UNIVERSIDAD NACIONAL AUTÓNOMA DE MÉXICO
PROGRAMA DE MAESTRÍA Y DOCTORADO EN INGENIERÍA
ENERGÍA - SOLAR FOTOTÉRMICA

MEZCLADO EN CONVECCIÓN NATURAL

T E S I S

QUE PARA OPTAR POR EL GRADO DE:
MAESTRO EN INGENIERÍA

PRESENTA:
PABLO SEBASTIÁN CONTRERAS OSORIO

TUTOR PRINCIPAL:
DR. EDUARDO RAMOS MORA
INSTITUTO DE ENERGÍAS RENOVABLES, UNAM

MÉXICO, D. F. NOVIEMBRE 2014

JURADO ASIGNADO:

Presidente: Dr. Mariano López de Haro

Secretario: Dr. Eduardo Ramos Mora

Vocal: Dr. Luis Miguel de la Cruz

$1^{er.}$ Suplente: Dr. Sergio Cuevas García

$2^{do.}$ Suplente: Dr. Raúl Mauricio Rechtman Schrenzel

Lugar donde se realizó la tesis:

Instituto de Energías Renovables, UNAM
Temixco, Morelos

TUTOR DE TESIS

DR. EDUARDO RAMOS MORA

FIRMA

Contents

Resumen **9**

Abstract **11**

Introduction **13**

1 Background **19**

1.1 Mixing . . . 19

1.1.1 Flows and maps . . . 20

1.1.2 Characterization of mixing . . . 21

1.1.3 Thermal Mixing . . . 23

1.2 Governing equations for natural convection . . . 23

1.2.1 Boussinesq approximation . . . 25

1.2.2 Non-dimensional equations . . . 26

1.2.3 General scalar transport equation . . . 26

2 Topological analysis of mixing **29**

2.1 Flow topology . . . 29

2.1.1 Periodic points . . . 29

2.1.2 Periodic lines . . . 30

2.1.3 Symmetries . . . 33

2.1.4 Invariant surfaces . . . 35

2.2 Noninertial case in the lid-driven cylinder flow . . . 36

2.2.1 Area-preserving maps . . . 38

3 Convective mixing in three dimensions **45**

3.1 Problem statement . . . 46

3.2 Piece-wise steady and linear flow . . . 46

4 Numerical method for calculating the velocity field and particle tracking 53
4.1 Finite Volume Method . . . 53
4.1.1 Discretization . . . 54
4.1.2 Pressure correction methods . . . 57
4.1.3 Linear systems solution . . . 58
4.2 Coherent structures . . . 59
4.2.1 Particle tracking . . . 59
4.2.2 Invariant surfaces . . . 59
4.2.3 Periodic points . . . 60

5 Results 63
5.1 Flow topology . . . 63
5.1.1 Symmetries . . . 63
5.1.2 Invariant surfaces and intra-surface dynamics . . . 65
5.1.3 Period-1 lines . . . 92
5.1.4 Classification of periodic points . . . 98

6 Summary 107

A Dynamical systems 109
A.1 Hamiltonian systems . . . 111

B Incompressibility constraint 113

List of Figures

1 Poincaré map for the asteroid. 15

2 Stable and Unstable axes. 16

2.1 Poincaré surface of section for the standard map, the coordinates p and θ are periodic. (a) $k = 0$, (b) $k = 0.1$, (c) $k = 0.4$, (d) $k = 0.8$, (e) $k = 1$, (f) $k = 1.2$. 43

2.2 Continuation of the previous sequence. Poincaré surface of section for the standard map, the coordinates p and θ are periodic. (a) $k = 1.5$, (b) $k = 2.2$, (c) $k = 3$, (d) $k = 6$. 44

3.1 Boundary layer at a heated vertical flat plate. We show distributions of velocity and temperature. 45

3.2 Time-periodic wall temperature protocol. In the first half of the cycle, two opposite vertical walls are sequentially kept at a higher and lower temperatures, respectively. In the second half, the temperature of the other two vertical, opposite walls is assumed to take the same time-dependent values. (This figure was made by L. M. de la Cruz). 47

3.3 (a) Coordinate system for the unitary cube. Heating protocol will be carried out in the vertical walls. (b) Piece-wise steady and linear flow configuration for a plane $z = const.$, with boundary conditions for one quarter of the total cycle. 48

4.1 Discretized domain using control volumes. In the FVM the discretized space is formed by a set of small cells, one cell being associated to one mesh point. 54

4.2 Control volume surrounding P. The neighbor nodes are represented by capital letters and small letters denote points on the faces of control volumes. In this way we denote variables evaluated at the center and at the boundaries of volumes respectively. 55

5.1 Velocity fields for the first half of the forcing protocol. Two streamlines and the temperature distribution for the middle z plane are also shown. The origin of the frame of reference is located at the lower left corner at the back of the cube, the z direction is pointing to the front of the cube. (a) First quarter of the forcing protocol and (b) second quarter of the forcing protocol for Ra $= 7 \times 10^4$ and a mesh of 96^3 from a diagonal view. (c) First quarter of the forcing protocol and (d) second quarter of the forcing protocol for Ra $= 9 \times 10^4$ and a mesh of 128^3 from a frontal view. 64

5.2 (a) Qualitative flow produced by the application of first half of the protocol $\mathbf{F}_1$ (this is a sketch of the general behavior and not an exact representation). (b) Analogy of the heating protocol with movement of walls. 65

5.3 (a) Typical Lagrangian orbit of a tracer for 20 cycles. (b) Poincaré map built from (a) for 200 cycles. Ra $= 1 \times 10^5$ and radius $= 0.307$. 66

5.4 Poincaré maps on invariant surfaces for Ra $= 3 \times 10^4$. (a) Typical invariant surface exhibiting two elliptic points symmetrically arranged, radius $=$ 0.239. (b) Settlement of nested invariant surfaces, red surface corresponds to the one in (a) and the radius of the blue one is 0.117. 67

5.5 Ra $= 3 \times 10^4$. Appearance of elliptic and hyperbolic points near the central region of surfaces. (a) Radius $= 0.307$. From (a)-(b) we decrease the radius of the invariant surface. 67

5.6 Ra $= 3 \times 10^4$. Position of invariant surfaces and planes of analysis. (a) Invariant surface of fig. 5.4 (a) and $x = 1 - z$ plane (central line from this view point). (b) Invariant surface of fig. 5.5 (b) and the considered planes from a top view. 68

5.7 Ra $= 3 \times 10^4$. Typical behavior near a 5-bifurcation point, i.e., presence of an elliptic and hyperbolic periodic-5 orbit surrounding one of the elliptic points. This is another view of fig. 5.5 (b) emphasizing the behavior near one of the elliptic points. From (a)-(b) we decrease the radius of the invariant surface. 68

5.8 Ra $= 3 \times 10^4$. Different view of the five-tupling bifurcation. In (a)-(g) the radius of the invariant surfaces decreases. The radius in (a) is 0.3131 and the radius in (g) is 0.2764. 69

5.9 Ra $= 5 \times 10^4$. In (a)-(f) we are decreasing the radius of the invariant surfaces. 70

5.10 Continuation of previous sequence. Ra $= 5 \times 10^4$. In (a)-(d) we are decreasing the radius of the invariant surfaces. 71

5.11 Ra $= 5 \times 10^4$. In (a)-(f) we are decreasing the radius of the invariant surfaces. We can see how points corresponding to the opposite elliptic points unite and separate. 72

5.12 Position of elliptic points for different radii of invariant surfaces (this is expressed as different colors). (a) Ra $= 3 \times 10^4$, (b) Ra $= 5 \times 10^4$. $(c) - (d)$ are yz projection of $(a) - (b)$. 73

5.13 Ra $= 7 \times 10^4$. In (a)-(c) we are decreasing the radius of the invariant surfaces, we can see how the two set of points unite. (d)-(f) top view with a cut in y of (a)-(c). 74

5.14 Ra $= 7 \times 10^4$. In (a)-(c) we are decreasing the radius of the invariant surfaces. $(d) - (f)$ Is a slightly different perspective of $(a) - (c)$. 75

5.15 Ra $= 7 \times 10^4$. In (a)-(f) The Poincaré sections of orbits on invariant surfaces are shown for different radii. We can see for certain radii the appearance of island chains at the center of the invariant surfaces between the two elliptic points (only one is shown for clarity), see (b) and (d). . . . 76

5.16 Comparison of invariant surfaces for Ra $= 5 \times 10^4$ (blue) and Ra $= 7 \times 10^4$ (red). In $(a) - (d)$ we are decreasing the radius. Topologies are similar but for 5×10^4 the different structures are exhibited at smaller radius compared with 7×10^4. 77

5.17 Ra $= 9 \times 10^4$. In (a)-(f) we are decreasing the radius of the invariant surfaces. 78

5.18 Continuation of previous sequence. Ra $= 9 \times 10^4$. In (a)-(d) we are decreasing the radius of the invariant surfaces. From (a) to (b) we have skipped one invariant surface because it shows a similar behavior. 79

5.19 Another view of the previous sequence. Ra $= 9 \times 10^4$. In (a)-(d) the radius of the invariant surfaces decreases. From (a) to (b) we have skipped one invariant surface because it shows a similar behavior. 80

5.20 Position of elliptic points for different radii of invariant surfaces. (a) Ra $= 5 \times 10^4$, (b) Ra $= 7 \times 10^4$ and (c) Ra $= 9 \times 10^4$. 80

5.21 Wandering of elliptic points augmenting Ra for fixed radius, from this perspective the plane $x = 1 - z$ is represented by the vertical line. (a) Ra $= 3 \times 10^4$, (b) Ra $= 5 \times 10^4$, (c) Ra $= 7 \times 10^4$, and (d) Ra $= 9 \times 10^4$. . 81

5.22 Ra $= 1 \times 10^5$. We focus in one of the elliptic points (right bottom). In (a)-(f) we are decreasing the radius of the invariant surfaces. 82

5.23 Continuation of previous sequence. Ra $= 1 \times 10^5$. In (a)-(f) we are decreasing the radius of the invariant surfaces. 83

5.24 Ra $= 1 \times 10^5$. (a) Invariant surfaces of fig. 5.22 (c) and (d). (b) Invariant surfaces of fig. 5.22 (c) and (e). 84

5.25 (a) Position of elliptic points for different radii of invariant surfaces for Ra $= 5 \times 10^4$. (c) View of (a) in the zy plane. (b) Same as (a) for Ra $= 1 \times 10^5$. (d) View of (b) in the zy plane. 84

5.26 Ra $= 5 \times 10^5$. In (a)-(d) we are decreasing the radius of the invariant surfaces. 86

5.27 Ra $= 5\times10^5$. In (a)-(d) we are decreasing the radius of the invariant surfaces. 86

5.28 Continuation of the previous sequence for the point on the left. Ra $= 5 \times 10^5$. In (a)-(f) we are decreasing the radius of the invariant surfaces. . 87

5.29 Ra $= 5 \times 10^5$. In (a)-(f) we are decreasing the radius of the invariant surfaces. 88

5.30 Ra $= 5 \times 10^5$. In $(a) - (c)$ we are decreasing the radius of the invariant surface. 89

5.31 Ra $= 5 \times 10^5$. In $(a) - (c)$ we are decreasing the radius of the invariant surface. 89

5.32 Ra $= 5\times10^5$. In (a)-(d) we are decreasing the radius of the invariant surfaces. 90

5.33 Periodic lines found on the plane $x = 1 - z$ (green) for different Ra. Black (Ra $= 1 \times 10^5$), purple (Ra $= 9 \times 10^4$), blue (Ra $= 7 \times 10^4$), red (Ra $= 5 \times 10^4$) and orange (Ra $= 3 \times 10^4$). Green dots represent the intersection of an invariant surface and the plane. 92

5.34 Periodic lines found on the plane $x = 1 - z$ (blue) for different Ra. (a) Black (Ra $= 1 \times 10^5$) and red (Ra $= 5 \times 10^5$). Blue dots represent the intersection of an invariant surface and the plane. 93

5.35 Projection of figures 5.33 and 5.34 on the xy plane, colors represent the same Ra numbers as in the previous figures. In (a) lines have been added to highlight the trends. 94

5.36 Settlement of periodic lines found for (a) Ra $= 9\times10^4$, and (b) Ra $= 5\times10^5$. Color black represents points on $x = z$ plane and blue and red points on $x = 1 - z$ plane. We added dots as an aid to the eye for the closed lines. . 95

5.37 Settlement of periodic lines found for Ra $= 5 \times 10^5$ on $x = 1 - z$ plane. . . 96

5.38 Settlement of periodic points found for Ra $= 5 \times 10^5$ on planes (a) $x = z$, (b), $x = 1 - z$. 97

5.39 Closed periodic lines and one invariant surface where there is merging of points for the 4-bifurcation. Ra $= 1 \times 10^5$. Blue points represent the line on $x = z$ plane and black points the line on $x = 1 - z$ plane. In (a) we show a top view of the intersection. $(b) - (c)$ show a cut of this arrangement. 97

5.40 Period-1 lines on $x = 1 - z$ plane. (a) Ra $= 3 \times 10^4$ and (b) Ra $= 5 \times 10^4$. Blue and green points represent elliptic periodic points and blue and red represent hyperbolic periodic points. 99

5.41 Period-1 lines on $x = 1 - z$ plane. (a) Ra $= 7 \times 10^4$ and (b) Ra $= 9 \times 10^4$. Blue and green points represent elliptic periodic points and blue and red represent hyperbolic periodic points. 100

5.42 Period-1 lines on $x = 1 - z$ plane. (a) Ra $= 1 \times 10^5$ and (b) Ra $= 5 \times 10^5$. Blue and green points represent elliptic periodic points and blue and red represent hyperbolic periodic points. 101

5.43 Classification of points for the closed period-1 line found on symmetry planes. (a) Ra $= 9 \times 10^4$. (b) Ra $= 1 \times 10^5$. Blue and green points represent elliptic periodic points and blue and red represent hyperbolic periodic points. We present a slightly different perspective in the two cases seeking the clarity of the figures. 102

5.44 Classification of points for the closed period-1 line found on symmetry planes for Ra $= 5 \times 10^5$. Blue and green points represent elliptic periodic points and blue and red represent hyperbolic periodic points. (a) Points on $x = z$ plane. (b) Arrangement of periodic points for four closed periodic lines. 103

5.45 Ra $= 5 \times 10^5$. Tracking of initial circles surrounding two periodic points, crosses, on the $x = 1 - z$ plane. (a) The black points represent a segment of the periodic line and the red points are located at circles surrounding the hyperbolic point (top of the image) and the elliptic point. (b) Deformation of circles (red) for 1 (blue), 2 (green), 3 (pink), 4 (yellow) and 5 (purple) cycles. 105

Resumen

El presente trabajo es un estudio de las propiedades topológicas del mezclado en un flujo generado por convección natural en un contenedor cúbico donde la temperatura de las paredes verticales es dependiente del tiempo. El fluido es Newtoniano pero no se consideran los términos no lineales, esto es, se considera el problema lineal en estado permanente a pedazos.

Seguimos la metodología propuesta para un flujo producido por el desplazamiento de paredes en una cavidad cilíndrica donde no se toman en cuenta los términos inerciales en una primera instancia. Las propiedades a considerar en este contexto son líneas periódicas, planos de simetría y superficies invariantes.

Para el flujo convectivo considerado en este estudio se identifican superficies invariantes que son topológicamente equivalentes a esferas y se encuentran líneas periódicas situadas en planos de simetría. Hacemos un estudio paramétrico en función del número de Rayleigh en el que se estudian seis valores del parámetro. Es interesante notar que encontramos una segmentación de las líneas periódicas con puntos elípticos e hiperbólicos. La dinámica en las superficies invariantes muestra los comportamientos distintivos de los mapeos que conservan área. Agrupamos las diferentes características observadas en términos del número de Rayleigh.

El flujo estudiado comparte ciertas propiedades con otros sistemas y a lo largo del trabajo hacemos notar las similitudes para tener un panorama amplio del mezclado de fluidos.

Abstract

In this work we use topological tools to describe the motion of a natural convective flow generated by stepwise, alternating heating and cooling protocol of opposite vertical walls of a cubic container. The working fluid considered is Newtonian but the nonlinear terms are neglected, i.e., we study the piece-wise steady and linear problem.

We follow the methodology presented for the lid-driven cylinder flow for the noninertial case. The organizing properties for the analysis are periodic lines, specific symmetries and invariant surfaces.

For this convective mixing flow we identify invariant surfaces formed by the orbits of massless tracers that are topologically equivalent to spheroids and periodic lines that are located on symmetry planes. We describe the previous features as functions of the Rayleigh number, a parametric study is made in which six values of the Rayleigh number are considered. It is particularly interesting that elliptic and hyperbolic segments of the periodic lines are found. We show that the dynamics on the invariant surfaces exhibit the complexity of area-preserving maps. We are able to group the different properties observed in terms of the Rayleigh number.

The flow under consideration exhibit properties that are present in other systems and in this work we point out specific similarities in order to have a wider context about fluid mixing.

Introduction

The simplest mixing problem corresponds to the mixing of a fluid with itself. Although this may seem a problem without much interest, in this case rests the foundation of the subject[1] [1].

Mixing is present in a variety of physical systems on a large range of time and length scales in nature and industry [3]; from the very small (microfluidic applications as microelectronics cooling, micro-reactors, 'labs-on-a-chip' for molecular analysis, etc.[2]), to the very large (mixing in the Earth's oceans and atmosphere). The ratio of the contributions of inertial forces (dominant at large scales) to viscous forces (dominant at small scales) spans more than twenty orders of magnitude [5]. In particular, mixing under laminar[3] flow conditions is key to a wide variety of fluid systems extending from micrometers to meters [6].

Over the years, efforts have been devoted to find methods to quantify and accelerate mixing; for example, using mechanical interactions to mix fluids with propellers or through periodic displacement of container's wall as in the flow between rotating cylinders. There are also non intrusive methods, for example, systems that rely on the use of electromagnetic forces to produce stirring in electrically conducting fluids [7].

The concept of laminar flow mixing with *blinking vortices* was introduced by Hassan Aref [8]. In Aref's system the flow was generated by point vortices fixed in space that are switched alternatively on and off; here he demonstrated that such a system can produce effective mixing. Experimental mixing with periodic motion for laminar flows was demonstrated by the group of Ottino, see for example [9]. In two dimensions, fluid mixing can be considered to be a visual representation of the behavior of a Hamiltonian system.

Here it is interesting to note the comment in the introduction of [4]: three decades have passed since Aref introduced the term *chaotic advection*, and twenty-five years since a textbook of the field appeared [10]. Clearly during this period of time a lot of research has been done but there are still open problems and our insight into laminar mixing remains incomplete to date.

[1] The term mixing has a precise meaning in ergodic theory, see for example [1]; in this work the term will be used in a fluid mechanical sense: physical processes in which fluids are combined in such a way that each individual fluid is continuously distributed among the other fluids [2].

[2] See the latest review of Aref et al. [4].

[3] They are characterized by low Reynolds numbers (Reynolds number, Re, represents the ratio of inertial to viscous forces in a fluid).

Poincaré maps and chaos

In this part of the introduction we follow the exposition made by Galison [11] and our purpose is present certain concepts used in the text. Poincaré was very interested in the three-body problem[4], which was described by Whittaker as '*the most celebrated of all dynamical problems* and which fulfilled the necessary criteria for a good mathematical problem as defined by Hilbert [12]. Poincaré took a new visual-geometrical approach to celestial mechanics through diagrams[5], he focused on qualitative features of differential equations.

It has been stated that the work of Henri Poincaré on the three body problem published in the journal *Acta Mathematica*, is renowned for containing the first mathematical description of chaotic behavior[6] [12]. He was aiming to set bounds on the motions caused by the mutual attractions of planets and to reaffirm the stability of the solar system.

Poincaré asked the following question: 'in the configuration of an asteroid hurtling around the orbiting system of Jupiter-Sun, what could the orbit of the asteroid do?' His idea was not to concentrate on the trajectory itself. If we think about simple periodic motion, the asteroid returning every time to the same spot with the same velocity, his idea was to examine the situation each time the asteroid came around as in a stroboscopic picture. This is the idea behind *Poincaré maps*.

In this particular case we can think the map as a plane that intersects the asteroid's wandering, Poincaré's idea was to study the patterns punctured in the plane, see fig. 1. For the simple periodic orbit the asteroid would punch the plane in the same point over and over again, that is we have a *fixed point*, F. Two interesting situations are when the intersections occur near but not in F; one possibility is a succession of points that approach to F (labeled by $S_1, S_2, ...$ in fig. 2) orbit by orbit. The curve through the points is named *stable axis*, S; an asteroid starting anywhere on the line gradually tends toward an orbit that circulates through F. A curve through F is called *unstable*, U, if an asteroid punching F gradually moves away from F; in this case, successive punctures run away from F in the plane, see fig. 2.[7]

In mid-1885 an announcement of a mathematical competition honoring the birthday of the King of Sweden Oscar II, was given. The problem: the three-body problem. Poincaré thought that if asteroid's intersections fled from a fixed point they would eventually settle

[4]It can be simply stated: three particles move in space under their mutual gravitational attraction; given their initial conditions, determine their subsequent motion [12].

[5]June [12] remarks that Poincaré instructs his readers in the introduction to his original memoir that: *'These theorems have been given in a geometric form which has to my eyes the advantage of making clearer the origin of my ideas ...'*.

[6]Here we can have an idea of the importance of Poincaré's work from the 1925 comment of George Birkhoff: '*Le Problème de* [sic] *trois corps* ... contained the first great attack upon the non-integrable problems of dynamics ... *Acta Mathematica* has had many remarkable articles, but perhaps none of larger scientific importance than this one.' [12].

[7]See chapter 2 and Appendix A and for more details on fixed points, stable and unstable manifolds, etc.

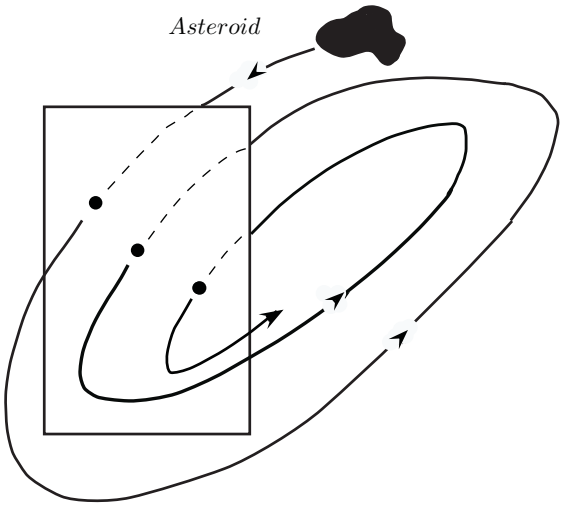

Figure 1: Poincaré map for the asteroid.

down toward another fixed point. However, some problems in the prize proof of Poincaré[8] were found and he discovered something that he had neither sought nor desired, a crack in the stability of the problem, *chaos*[9].

The idea of Poincaré was to suppose that a line of stability and a line of instability crossed at the fixed point F. If the asteroid begins near but not on the stable axis (labeled by C_0 on fig. 2), it will move toward F getting quite near to it and at some point it will fall under the influence of the unstable axis and begin to wander away from F, see the right panel of fig. 2. The interesting point comes if we suppose that the stable and unstable axes cross somewhere else, at H for example, a *homoclinic point*[10]. If an asteroid flies through H, since it must remain on S, it moves toward F but H is also on U and then the following points must also be on U, the result of both situation is a complex behavior. As pointed out by Poincaré: 'The intersections form a kind of lattice, web or network with infinitely tight loops; neither of the two curves must ever intersect itself but it must bend in such a complex fashion that it intersects all the loops of the network infinitely many times. One is struck by the complexity of this figure which I am not even attempting to draw' [14].

[8] 1890 Poincaré's applauded paper is very different from the version which actually won the prize [12].

[9] Holmes [13] pointed out that the memoir published in 1890 by Poincaré (the same work referred by Birkhoff) describing the prize problem is the first textbook in the qualitative theory of dynamical systems.

[10] As we have noted, Poincaré's discovery of a significant error in the original prize paper made him extend the material contained in the work, it was as a result of its correction that Poincaré made his important discovery of *homoclinic points* [12].

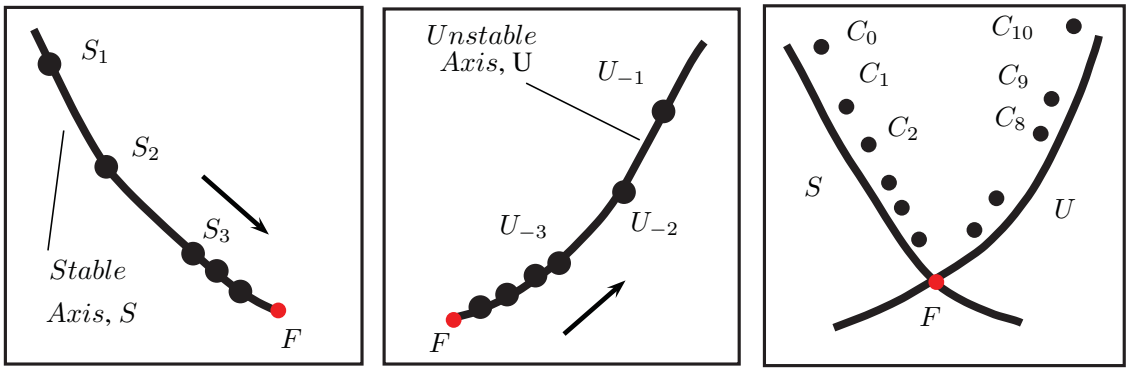

Figure 2: Stable and Unstable axes.

Stretching and folding

Ottino et al. [15] make a historical review of the connection between mixing, stretching and folding and chaos. Behind the chaotic behavior found by Poincaré are homoclinic intersections, the mechanism being exactly equivalent to stretching and folding in phase space. This idea is precisely the one advocated by Reynolds to explain fluid mixing. On the other hand, stretching and folding as the fingerprint of chaos formally appeared in the literature in the late 1960s through the *horseshoe map* of Smale, see [1] for more details about this map. Connections between fluid mixing, stretching and folding and horseshoes were made in the 80s, see [15] and references therein. The authors of the previously cited work show that Reynolds's stretching and folding idea of fluid mixing was replaced by the statistical viewpoint that was taken in the 1950s and 1960s[11] with the starting point being the averaged Navier-Stokes equations proposed by Reynolds himself. In this way the authors refer the history of mixing as one of failed connections[12]; it is now standard to visualize internal motion of fluids by deformation of 'colored bands' and to apply geometrical thinking to rationalize internal motion of fluids, ideas that were linked to the stretching and folding picture of fluid mixing.

Fluid mixing is an instance in which chaos is beneficial [16]. For laminar flow applications, biological, industrial, etc., chaotic advection is typically the only way to efficiently increase transport rates for mixing, reaction, and heat and mass transfer. In this context, we are interested in chaotic motion [17]. This is a particular interesting point of the area, usually, chaos is associated with something 'bad': undesirable vibrations, difficulty in control problems, yet another type of noise, etc. [4].

[11] The picture of turbulence during those decades was one of a structureless viewpoint where no pattern could exist. Similar comments were applied to mixing [15].

[12] Reynolds presented the stretching and folding mechanism for mixing in a 1894 lecture and the idea of averaged Navier-Stokes equations was published in 1895 [15].

Mixing of fluids

We can think a mixing problem as knowing where fluid particles are advected by a prescribed velocity field. For a two dimensional flow of an incompressible fluid the equations of motion of an individual passive particle can always be written in Hamiltonian form and methods of Hamiltonian mechanics can be applied [18], as opposed, the study of three dimensional mixing flows encounters considerable difficulties.

Unlike turbulent flows, where chaotic tracer motion is intrinsic to the stochastic velocity field, in the viscous limit chaotic tracer paths typically coexist with regular flow patterns. This reflects the essential difference between laminar and turbulent mixing [2].

In a Lagrangian representation, tracer motion of mixing flows is described by a dynamical system[13]. Much of the work due to the incorporation of dynamical systems theory to mixing is for two dimensional flows and the extension to the three dimensional case has seen less progress [19]. To study two and three dimensional periodic flows the concept of Poincaré maps is traditionally applied, this approach allows to transfer the problem from a continuos dynamical system to a discrete mapping and reduce the number of dimensions. An important characteristic for both classes of flows is the location of periodic points. In particular, the presence or absence of periodic points allows a judgement on the quality of mixing process [20].

In a series of papers, Clercx and collaborators have described a methodology to analyze the topological properties of mixing in a time-dependent driven flow inside a cylinder (lid-driven cylinder flow). For a brief review of their work see [21] or [4, section V]. The analysis made by the group of Clercx starts by considering symmetry planes, periodic lines and invariant surfaces of the Lagrangian orbits in a Stokes flow, i.e., in the non-inertial limit, $\mathrm{Re} = 0$.

To identify periodic invariant curves the authors use the symmetries of the flow, then they determine the stability of these curves and, in general, find that a particular curve may be normally hyperbolic along certain length but change to normally elliptic along the rest of the length. The point where the curve changes stability is normally parabolic [19].

For some protocols the authors find that the flow structure is such that it is filled out by concentric invariant spheres. The particle motion on the invariant spheres can take a variety of forms, depending on the radius of the sphere, as well as the forcing. Invariant spheres can exhibit particle motions that appear integrable (regular), a mixture of regular and chaotic, and completely chaotic. The dynamics of particle motion on the sphere is governed by two dimensional time-periodic Hamiltonian dynamics [19]. In chapter 2 we will review the topological analysis made by these authors more widely.

From the previous cited methodology we briefly comment on three works. Malyuga et al. [18] consider the Stokes problem for the lid-driven cylinder flow with discontinuous movements of top and bottom walls, a classification of periodic points is presented and the

[13] Dynamical-systems theory deals primarily with the behavior of differential equations and their relatives, iterated mappings, we refer to [13] for a brief history of the mathematical foundations of the subject.

flow near these points is explored using Poincaré maps. Here the authors find periodic lines and isolated periodic points for the different studied protocols. Speetjens et al. [2] study three dimensional advection of passive tracers in non-inertial lid-driven cylinder flows by means of numerical simulations and laboratory experiments. Tracer orbits exhibit quasi-two dimensional motion within thin shells, effectively two dimensional dynamics or truly three dimensional dynamics covering the entire flow domain depending on the time-periodic forcing protocol [2, 21, 4]. The configuration considered by Pouransari et al. [6] is the lid-driven cylinder flow where the fluid is set in motion through periodic forcing resulting from in-plane motion of the lower endwall. Once the topological properties of the linear flow have been found, the analysis proceeds by looking at the modifications of the topological properties brought about by the inclusion of the nonlinear terms in the momentum conservation equations, here, the authors show new types of dynamical systems structures [19].

Chaotic mixing can be achieved inside a two dimensional cavity with time dependent wall temperature in presence of a body force as showed by de la Cruz & Ramos [22]. Under these conditions a vortex of variable strength is generated and the center of the vortex moves around the container. In this configuration no moving walls are required to mix the fluid inside the cavity.

In the present investigation, we study a natural convective flow inside a cubic box with a time-dependent temperature in the vertical walls. Our system shares some features with the lid-driven cylinder flow; motion is generated by time-dependent boundary conditions, although the main difference is that the displacement of a wall is a surface force while natural convection is a body force. The dynamical consequences of these two effects are similar insofar the motion in the natural convective flow is mostly concentrated in the dynamic boundary layer that forms very close to the vertical wall.

Chapter 1 is an introduction to the study of mixing and a summary of the equations of natural convection. Chapter 2 presents a review of the topological analysis of mixing, as we have commented, we mainly follow the papers of the group of Clercx, but also add some results of the 'blinking rolls' flow and the 'blinking tumbler' from granular flows because these configurations share some features with our system and it is particularly interesting that an analytic treatment can be made. In chapter 3 the problem statement is set for the piece-wise steady and linear flow. Chapter 4 considers the numerical tools of solution for the topological analysis and in chapter 5 the results are presented. Finally we give the conclusions and an outlook of future work in chapter 6.

Chapter 1

Background

In this chapter we will briefly introduce previous ideas in the study of mixing and the concept of chaotic advection. We also enunciate the context in which are located three dimensional unsteady incompressible laminar flows from the point of view of volume preserving maps. We shortly comment about some examples of thermal mixing in the literature and in the second part we present a summary of the governing equations for natural convection.

1.1 Mixing

Over the years, different strategies have been adopted in the study of mixing. Ottino [10] shows examples of papers published in the 40's and 50's related to the subject; in some of them, the approach is statistical and others emphasize geometric aspects of the problem. Subsequently, statistical theory took over and geometrical aspects of the problem were somewhat lost as was briefly commented in the Introduction.

Danckwerts in 1953 focused primarily on the characterization of the mixed state, he devised parameters to indicate how well a mixed system is[1]. A large number of mixing measures exist, e.g., interfacial area between fluids per unit volume, fractal dimension, various types of correlation and distribution functions, average cluster size and cluster size distribution, etc., however, the characterization of the structures depend strongly on the specific application[2]. The importance and relevance of measures of mixing is not clear; they might be impossible to relate to the mixing process itself or they might be unmeasurable from an experimental viewpoint [3].

In mechanical mixing, an initially designated material region of fluid stretches and folds throughout the space. Without the action of molecular diffusion, mechanical mixing produces a lamellar structure and a measure of the state of mechanical mixing is given by the thicknesses of layers.

Wiggins & Ottino [1] give the mathematical definition of a mixing transformation in the context of the hierarchy of characterization of mixing. Intuitively the basic idea of the definition is as follows: within the domain R, denote a region B of fluid (differentiated by

[1] Ottino [3] remarks that the earliest ideas about quantification of mixing come from Danckwerts.

[2] The measure should be selected according to the specific application and it is futile to devise a single measure to cover all contingencies [10].

color, for example) and any other region W. After n applications of the mixing process if we take any region of W we have the same fraction of the fluid B as that for the entire domain[3].

Ottino et al. [15] present two other similar mathematical definitions of mixing, *measure-theoretic mixing* and *strongly topologically mixing*. A summary of the quality of the mixed state and some measures of mixing can be found in [4, section VI]. Briefly, the idea in most definitions is that mixing can be quantified using statistical quantities like the *coarse-grained density* and *entropy*[4]. The authors consider three criteria of the mixed state: the *average square density*, proposed by Welander in 1955; the *entropy*, following ideas of Gibbs proposed in 1902, and the *intensity of segregation* and *scale of segregation* proposed by Danckwerts in 1952.

The fundamental concept behind these measures is to estimate the time necessary for the mixed state to become uniform within some specified range, for a given volume element size ('the grain') [4]. In this work we will not use these concepts but we observe that their study might be of great interest in the context of the natural convective flow studied here.

1.1.1 Flows and maps

We present the main idea of the hierarchy in the dynamics of incompressible laminar fluid flows following Cartwright et al. [23]. Dynamics of one dimensional incompressible laminar flow (whether steady or unsteady), as Poiseuille or Couette flow, is well understood: one dimensionality plus incompressibility means that the fluid velocity must be uniform at any time in the direction of the flow.

As we mentioned in the introduction, two dimensional steady incompressible flows are integrable, like one degree of freedom time independent Hamiltonian systems. Two dimensional unsteady incompressible flows, on the other hand, display the dynamics of one degree of freedom time dependent Hamiltonians[5], which are generically nonintegrable. If we have time-periodic systems, the resulting maps are *area-preserving* on the plane, and show the chaotic motion typical of these maps, with chaotic trajectories bounded by the invariant KAM tori [23].

The steady three dimensional incompressible flow problem is similar to the unsteady case in two-dimensions: the Poincaré map to any section transverse to the flow is an area-preserving map on the plane. These flows can be reduced to a one-degree of freedom time-dependent Hamiltonian system, except at points where the flow has *fixed points*.

[3] Again the comment made by the authors is that from the viewpoint of applications we find a problem since in this definition is implicit the limit $n \to \infty$ and in practice we desire the number of cycles to be as small as possible.

[4] These quantities may be employed if at any moment in time the distribution of the marked fluid to be mixed in the ambient fluid domain in exactly known [4].

[5] In the literature it is also found that if the Hamiltonian is an explicit function of time the system has an additional degree of freedom. In the case of time-periodic Hamiltonians, time is regarded as an additional $\frac{1}{2}$ degree of freedom [10].

Arnold first addressed chaos in three dimensional steady incompressible inviscid fluid flow [24, 23, 4, 25].

Three dimensional unsteady incompressible laminar flow has an entirely different dynamics. Periodic systems in this category produce stroboscopic maps in three dimensions that preserve volume. These maps are named *Liouvillian maps*, do not correspond to Hamiltonian systems, which have phase spaces of even dimensionality: Hamiltonians with two or three degrees of freedom produce volume preserving maps of two or four dimensions respectively [23]. An important feature of Liouvillian maps is that they can exhibit types of behavior analogous to both two and three degree-of-freedom Hamiltonian systems [24, 23]. We want to stress that to study volume-preserving systems it is mandatory the use of algorithms that provide accurate solutions to the incompressibility constraint, i.e., $\nabla \cdot \mathbf{u} = 0$.

A similar feature between the system studied in this work and the one analyzed by Clercx and collaborators is the presence of spheroidal invariant surfaces[6] that topologically differ from the classical invariant tori. The context of these flows is the study of generic volume-preserving systems. Tumbled granular flows also display features as time periodicity, invariant surfaces and periodic lines of elliptic and hyperbolic type [6]. Another system that shares some topological characteristics is the 3D time-periodic laminar flow driven by a rotating sphere [26].

Even if great progress has been made since mid-1980s, the development of a Hamiltonian-like framework for 3D Lagrangian transport is far from complete, for example, response scenarios to perturbations and routes to chaos and particularly scenarios for coherent structures of different topology as invariant spheroids remain outstanding [21, 4]. Topological equivalence of invariant surfaces to spheres is a key feature; the Hamiltonian response to perturbation of *one-action maps*[7] depends explicitly on the assumption that both intrasurface coordinates are periodic, this condition is fulfilled for tori but violated for spheres [27]. In this context, bifurcations on invariant surfaces are likely to play a pivotal role [21].

1.1.2 Characterization of mixing

As we pointed out in the introduction, mixing of a continuous medium in motion is intimately related to stretching and folding of material surfaces or lines in two dimensions, an exact description of mixing should be given in terms of the location of interfaces as functions of space and time. However, this level of description is rare because the velocity fields usually found in mixing processes are complex and furthermore the mixing problem starts rather than ends with the specification of the velocity field [3].

Mixing is also strongly related to flow visualization, but frequently, the typical ways of visualizing a flow (streamlines, pathlines, and to a lesser degree, streaklines) are insufficient to understand the process [10].

[6] See chapter 2 for details on invariant surfaces.

[7] They confine tracers to invariant surfaces, see section 2.2 for more about maps.

In the work of the Clercx group, tracer dynamics is investigated in terms of Poincaré sections of tracers released at strategic locations in the domain that enable visualization of the flow topology. We will study some properties of the results obtained with this technique in chapter 2.

When a particle moves with the fluid, we speak of advection, sometimes *passive* advection[8] to emphasize that the particle is light and inert [28]. The motion of passive tracers in the flow is governed by the kinematic equation, called by Aref as *advection equations*

$$\frac{d\mathbf{x}}{dt} = \mathbf{u}(\mathbf{x}, t), \quad \mathbf{x}(0) = \mathbf{x}_0, \tag{1.1}$$

which describe the evolution of the positions $\mathbf{x}(t)$ of tracers released at $\mathbf{x}_0$. These equations belong to the Lagrangian description of fluid motion, where individual particles are tracked. The general solution of eq. (1.1) reads $\mathbf{x}(t) = \mathbf{\Phi}_t(\mathbf{x}_0)$ and uniquely determines the current position $\mathbf{x}$ for a given initial tracer position $\mathbf{x}_0$.

The orbit defined by $X_t(\mathbf{x}_0) = \mathbf{\Phi}_{t'}(\mathbf{x}_0)$, where $t' = [0, t]$, coincides with the Lagrangian trajectory followed by the tracer while propagating from $\mathbf{x}_0$ to $\mathbf{x}$. For steady systems $\mathbf{u} = \mathbf{u}(\mathbf{x})$ and the tracer paths coincide with streamlines [2].

Time-periodic systems are characterized by $\mathbf{u}(\mathbf{x}, t) = \mathbf{u}(\mathbf{x}, t + T)$, with T the global period, and the corresponding discrete mapping by $\mathbf{x}_{k+1} = \mathbf{\Phi}_T(\mathbf{x}_k)$, where $\mathbf{x}_k$ is the tracer position after k periods of the time-periodic protocol. The sequence $[\mathbf{x}_0, \mathbf{x}_1, \mathbf{x}_2, ...]$ contains the subsequent tracer positions at times $[0, T, 2T, ...]$ and forms the temporal *Poincaré section* of the tracer trajectory[9].

The system of ordinary differential equations (1.1) can generate nonintegrable or chaotic dynamics. As we stated in the previous subsection 1.1.1, steady, two dimensional advection is integrable[10], in two dimensions we need time-dependent flow to produce chaotic particle motion but three dimensional flows need not be time-dependent in order to have chaos.

Chaotic advection is a way to generate small-scale structures in the spatial distribution of advected fields by using the stretching and folding property of chaotic flows [4]. In chaotic advection particles moving passively with the flow field follow chaotic particle trajectories.

Mixing by chaotic advection has the advantage over turbulence that it does not require the large input of energy to maintain the Kolmogorov cascade to create small-scale structures.

[8] The formal statement of passive advection in terms of velocity can be expressed as $\mathbf{v}_{\text{particle}} = \mathbf{v}_{\text{fluid}}$.

[9] As pointed out by Cartwright et al. [23], the term *Poincaré section* is used for the sectioning of the flow in time or space to produce a map. The terminology is not completely fixed; generally, Poincaré section to mean any such section, and Poincaré map to be the dynamics on the section. See appendix A for more details about eq. (1.1) and mappings.

[10] Two dimensional kinematics of advection by an incompressible flow is equivalent to the Hamiltonian dynamics of a one-degree-of-freedom system (the stream function plays the role of the Hamiltonian).

1.1.3 Thermal Mixing

Heat transfer and mixing plays an important role in fields as earth and life sciences, chemical engineering and material science [29]. Since 1990s there have been many studies concerned the use of chaotic advection flows to promote heat transfer.

In this context, two main classes of flow geometries are encountered in the production of chaotic mixing: those that use rotating elements or translating elements and those that use multiple curved ducts, see [30] for examples in both cases. For both types of geometry, the heat is communicated to the fluid through the walls, a situation that is very common in industrial applications.

We want to introduce a mixer composed of two circular rods inside a cylindrical tank (two-rod mixer[11]) that has been studied by Le Guer & El Omari [4, 30]. The tank and the rods can be heated or cooled and can rotate around their respective axes. This mixer is suitable for obtaining global chaotic flow without large KAM regions. The authors consider a highly viscous fluid ($\mathrm{Re} \approx 1$) with a high Prandtl number ($\mathrm{Pr} = 10^4$), so it is difficult to mix.

The authors have shown for Newtonian and non-Newtonian fluids and for a constant wall-temperature boundary condition (Dirichlet condition) that the efficiency of thermal exchange is strongly dependent on the choice of the stirring protocol imposed on the walls. The authors have also considered a constant heat flux imposed at the wall (Neumann condition) [30].

For constant temperature wall condition El Omari & Le Guer [29] show that the use of discontinuous wall rotations is necessary to promote heat transfer by chaotic mixing and to avoid hot spots in the vicinity of the walls, that is, maximizing heat transfer from the wall boundaries requires that the walls (tank or rods) move alternately.

We won't expand on the work of the two-rod mixer because we have followed the topological analysis presented for the lid-driven cylinder flow. However, it may be of interest to return and compare the results obtained for this kind of configuration, particularly, the evolution of the fluid temperature, its homogenization and mixing indicators. The authors focus mainly on different statistical tools.

1.2 Governing equations for natural convection

Natural convection flows arise when buoyancy forces due to density differences occur and these act as driving forces [31]. If the density is kept constant, a natural convection flow cannot form; the direct origin of the formation of natural convection flows is heat transfer via conduction through the fixed walls surrounding the fluid, heat supply by an internal dissipation mechanism, Joule or viscous dissipation, or heat injection by an external mechanism like electromagnetic radiation.

[11] This mixer geometry can be seen as an extension of the eccentric cylinder geometry (journal bearing flow).

The equations describing the natural convective motion of a Newtonian fluid can be found in many references [32, 33, 34] and we will only enunciate them briefly.

Consider a fluid in which the density ρ is a function of position x_j $(j = 1, 2, 3)$ and time t, and let u_j $(j = 1, 2, 3)$ denote the components of the velocity. The variables p and T are the pressure and the temperature of the fluid, respectively. We shall use the notation of Cartesian tensors with the usual summation convention. The conservation equations are presented below.

Mass conservation equation

$$\frac{\partial \rho}{\partial t} + \frac{\partial (\rho u_j)}{\partial x_j} = 0. \tag{1.2}$$

For an incompressible fluid, the equation of continuity (1.2) reduces to

$$\frac{\partial u_j}{\partial x_j} = 0; \tag{1.3}$$

the velocity field in this case is *solenoidal*.

Momentum conservation

$$\rho \frac{\partial u_j}{\partial t} + \rho u_k \frac{\partial u_j}{\partial x_k} = -\frac{\partial p}{\partial x_j} + \frac{\partial}{\partial x_j}(\lambda \frac{\partial u_k}{\partial x_k}) + \frac{\partial}{\partial x_i}[\mu(\frac{\partial u_i}{\partial x_j} + \frac{\partial u_j}{\partial x_i})] + \rho f_j, \tag{1.4}$$

where μ is the dynamic viscosity of the fluid[12], the parameter λ is referred as the second viscosity coefficient and f_j is the jth component of an external force acting on the fluid. Equations (1.4) are known as the *Navier-Stokes equations*. For an incompressible fluid in which μ is constant, equations (1.4) simplifies to

$$\rho \frac{\partial u_j}{\partial t} + \rho u_k \frac{\partial u_j}{\partial x_k} = -\frac{\partial p}{\partial x_j} + \mu \frac{\partial^2 u_j}{\partial x_k \partial x_k} + \rho f_j. \tag{1.5}$$

In the special case of negligible viscous effects, the Laplacian term is eliminated, equations (1.5) are known as *Euler equations* and the fluid is called *inviscid*.

Energy conservation

$$\rho \frac{\partial e}{\partial t} + \rho u_k \frac{\partial e}{\partial x_k} = -p \frac{\partial u_k}{\partial x_k} + \frac{\partial}{\partial x_j}(k \frac{\partial T}{\partial x_j}) + \lambda (\frac{\partial u_k}{\partial x_k})^2 + \mu (\frac{\partial u_i}{\partial x_j} + \frac{\partial u_j}{\partial x_i}) \frac{\partial u_j}{\partial x_i}. \tag{1.6}$$

Here e is the internal energy per unit mass and k is the thermal conductivity of the fluid appearing in Fourier's law.

[12] The kinematic viscosity is defined by $\nu = \mu/\rho$.

Equation of state

The set of mass, momentum and energy conservation equations do no constitute a closed system. Additional relationships between thermodynamic variables are required. The most convenient are

$$p = p(\rho, T), \tag{1.7}$$

and

$$e = e(\rho, T). \tag{1.8}$$

Equations (1.7) and (1.8) are general representations of the thermal and caloric equations of state, respectively.

1.2.1 Boussinesq approximation

Equations (1.2), (1.4) and (1.6) are the basic hydrodynamical equations and are of quite general validity. However, there are many situations where they can be simplified considerably; these situations occur when the variability of the density and of the various coefficients (μ, c_V, α, and k) due to variations in the temperature is only moderate. Under this condition, we may treat ρ as constant in all terms in the equation of motion except the one in the external force and all the physical attributes in the coefficients are considered constants, this is the Boussinesq approximation[13] [32].

Under this approximation, the conservation equations for Newtonian incompressible fluids take the following form

$$\frac{\partial u_j}{\partial x_j} = 0, \tag{1.9}$$

$$\rho_0[\frac{\partial u_i}{\partial t} + u_j \frac{\partial u_i}{\partial x_j}] = -\frac{\partial p}{\partial xi} + \mu \frac{\partial^2 u_i}{\partial x_j \partial x_j} + \rho b_i, \tag{1.10}$$

$$\frac{\partial T}{\partial t} + u_j \frac{\partial T}{\partial x_j} = \alpha \frac{\partial^2 T}{\partial x_j \partial x_j}, \tag{1.11}$$

$$\rho = \rho_0 \left[1 - \beta(T - T_0)\right], \quad \beta = -\frac{1}{\rho_0}\left(\frac{\partial \rho}{\partial T}\right)_{T=T_0}, \tag{1.12}$$

where T_0 is a reference temperature, ρ_0 is the density for $T = T_0$. The variable $\alpha = k/(\rho c_V)$, is the thermal diffusivity. In eq. (1.11) it is considered that the internal energy can be expressed as $e = c_V T$, with c_V the specific heat at constant volume. In eq. (1.12), the density function $\rho(T)$ is expanded in Taylor series with β the coefficient of volume expansion and breaking off after the linear term.

[13] The formal conditions under which the Boussinesq approximation is valid can be found in Gray & Georgini [35]. See also the work by Ramos & Vargas [36].

1.2.2 Non-dimensional equations

In order to simplify the generalization of the results, it is convenient to write the variables in the natural scale of the flow as follows

$$x_j = \frac{x'_j}{H}, \quad t = \frac{t'}{H^2/\alpha}, \quad u_j = \frac{u'_j}{\alpha/H}, \quad p = \frac{p'}{\alpha\nu\rho_0/H^2}, \quad \text{and} \quad T = \frac{T'-T_C}{\Delta T} - \frac{1}{2},$$

where H is the vertical characteristic length of the container and $\Delta T = T_H - T_C$, is the difference between hot, (T_H), and cold, (T_C), temperatures. The non-dimensional conservation equations are [37]:

$$\frac{\partial u_j}{\partial x_j} = 0, \tag{1.13}$$

$$\frac{\partial u_i}{\partial t} + u_j\frac{\partial u_i}{\partial x_j} = -\frac{\partial p}{\partial x_i} + \mathrm{Pr}\frac{\partial^2 u_i}{\partial x_j \partial x_j} + b_i, \qquad (b_i = (0, \mathrm{PrRa}T, 0)) \tag{1.14}$$

$$\frac{\partial T}{\partial t} + u_j\frac{\partial T}{\partial x_j} = \frac{\partial^2 T}{\partial x_j \partial x_j}, \tag{1.15}$$

where the non-dimensional parameters are the Prandtl and Rayleigh numbers defined by

$$\mathrm{Pr} = \frac{\nu}{\alpha} \quad \text{and} \quad \mathrm{Ra} = \frac{g\beta\Delta T H^3}{\alpha\nu}. \tag{1.16}$$

We are considering the gravity force in the negative direction of y-axis.

1.2.3 General scalar transport equation

The previous equations share some features which can be used to write a general transport equation. If we introduce a general variable ϕ, we can write the fluid flow equations in the following form [38]

$$\frac{\partial \phi}{\partial t} + \frac{\partial}{\partial x_j}(u_j\phi) = \frac{\partial}{\partial x_j}(\Gamma\frac{\partial \phi}{\partial x_j}) + S, \quad j = 1, 2, 3. \tag{1.17}$$

The second term on the left and the first term on the right hand side of this equation are the convective and diffusive terms respectively. Γ is a generalized diffusion coefficient and S is the source term. Equation (1.17) is the *transport equation* for property ϕ. Equations (1.13), (1.14) and (1.15) can be expressed in the form of (1.17) with the following identifications

Equation	ϕ	Γ	S_i
Mass	$\rho = \text{constant}$	0	0
Momentum	u_i	Pr	$-\frac{\partial p}{\partial x_i} + b_i$
Energy	T	1	0

Table 1.1: Correspondence of balance equations with the general transport equation. $i = 1, 2, 3$.

Eq. (1.17) is used as the starting point for computational procedures in the finite volume method and we will return to it in chapter 4.

Chapter 2

Topological analysis of mixing

In this chapter we present a recapitulation of the topological concepts applied to mixing processes that are available in the literature. The flow topology can be characterized by the collection of coherent structures embedded in the web of tracer orbits. Coherent structures geometrically determine the transport properties of the flow so they are essential to three dimensional mixing phenomena.

These concepts are important in the present context since they constitute the fundamental ideas of the modern analysis of three dimensional mixing as introduced Pouransari et. al [6]. Further, visualization and isolation of coherent structures in numerical and experimental data is a big challenge for three dimensional transport studies [4].

2.1 Flow topology

Flow topology imposes geometrical constraints on the tracer motion and thus dictates the advection properties of a flow. The coherent structures and organizing properties are periodic lines, specific symmetries and invariant surfaces associated with constants of motion.

2.1.1 Periodic points

Location of periodic points of two and three dimensional flows is closely related to the problem of determining regions of regular behavior, which are barriers for mixing. Period-1 structures are the most important for the flow topology, as they determine the global organization. Higher-order structures are embedded within lower-order ones and thus concern smaller features [4].

In three dimensions these points can form one-dimensional periodic lines, and, this situation is of interest because the flow near a periodic line is topologically similar to the flow near a periodic point in the two dimensional case [18].

The presence or absence of first-order periodic points in mixing protocols consisting of time-periodic boundary conditions can be explained using a qualitative argument. By definition, periodic points are points where tracers return to their original position after one or more periods of the flow, if a periodic point exists, the tracer orbit must be closed.

An orbit consists of segments stemming from the streamlines of each step of the protocol, and in order to have closed trajectories the crossing of streamlines is required, moreover, detecting the absence of first-order periodic points in a mixing flow gives an early, strong indication of poor mixing properties [20].

Periodic points in two dimensional maps can be classified as hyperbolic, elliptic, or parabolic, according to the nature of deformation of the fluid in the neighborhood of the periodic point. Elliptic points are surrounded by *islands*, or *regular regions*, where there is no chaos [39]. Hyperbolic points are accompanied by stable, W^s, and unstable, W^u, manifolds that either merge into closed orbits or display transversal intersection. The former phenomenon acts obstructing communication between flow regions, whereas the later implies stretching and folding of material elements. The stable manifold is defined as a set of points that tends to the periodic point, $\mathbf{P}$, at moments $t_n = nT$ with $n \to \infty$, while the unstable manifold, is defined as a set of points that tend to $\mathbf{P}$ at moments $t_n = -nT$ with $n \to \infty$ [18].

In three dimensional space, periodic points may either appear isolated or merge into periodic lines. If a periodic point is isolated, one of its manifolds is a surface, while the other is a line. If periodic points are arranged on a line, their stable and unstable manifolds are integrated into two surfaces [18]. In two dimensional flows the stable and unstable manifolds are two lines that can intersect at an infinite set of points called *homoclinic points*, or *heteroclinic points* for intersection of manifolds of two different fixed points. The behavior of the flow near homoclinic points is very complicated and their existence in the flow generally indicates chaotic behavior of the system; the complex dynamics of chaotic systems is intimately related to the emergence of periodic points in the flow, in particular lower-order periodic points [10]. Homoclinic intersection of stable an unstable manifolds in a flow is referred to as being 'signature of chaos'[1], the manifolds are folded infinitely many times and the layered form is associated with locally efficient mixing behavior. Such a behavior of the manifolds corresponds with the so called *horseshoe map*, which describes repeated stretching and folding of material by the flow.

Generally, the periodic points of three dimensional flows are characterized by a much richer variety compared with the points of two dimensional flows, a general classification of periodic points in three dimensional flows is presented by Malyuga et al. [18], see table 2.1.

2.1.2 Periodic lines

Key coherent structures for laminar flows are periodic lines, that is, material curves consisting of points that periodically return to their initial position. These structures have been found in numerical simulation and also in experiments, as is demonstrated for the lid-driven cylinder flow [40].

Periodic points of order p (period-p points) of a time-periodic map are material points that will return to their initial positions after p periods: $\mathbf{X} = \mathbf{\Phi}^p(\mathbf{X})$. The local behaviour

[1] See Appendix A for more details.

at such period-p points is determined by

$$d\mathbf{x}_{n+1} = \mathbf{F} \cdot d\mathbf{x}_n, \quad \mathbf{F} = \nabla \mathbf{\Phi}^p|_{\mathbf{X}} = \sum_{i=1}^{3} \lambda_i \mathbf{n}_i \mathbf{n}_i, \tag{2.1}$$

with $d\mathbf{x}$ being the local frame of reference, $\mathbf{F}$ being the deformation tensor (real Jacobian matrix) representing the locally linearized mapping $\mathbf{\Phi}$ and $\{\lambda_i, \mathbf{n}_i\}$ being its spectral decomposition [18]. Stable and unstable structures may emerge, depending on the properties of $\mathbf{F}$.

The eigenvalue spectrum $\Lambda = \{\lambda_1, \lambda_2, \lambda_3\}$ determines the local dynamics and thus the type of periodic point; the solenoidality of the flow field $\mathbf{u}$ implies $\lambda_1\lambda_2\lambda_3 = \det(\mathbf{F}) = 1$, where det is the determinant of $\mathbf{F}$. The eigenvalue spectrum of $\mathbf{F}$ is found with the characteristic polynomial

$$\lambda^3 - J_1\lambda^2 + J_2 - J_3 = 0, \tag{2.2}$$

with $J_1 = \mathrm{Tr}(\mathbf{F})$, $2J_2 = \mathrm{Tr}^2(\mathbf{F}) - \mathrm{Tr}(\mathbf{F}^2)$, $J_3 = \det(\mathbf{F})$, Tr and det represent the trace and determinant, respectively. Equation (2.2) always has one real positive eigenvalue, say, λ_1, and it can be rewritten as follows

$$(\lambda - \lambda_1)(\lambda^2 + (\lambda_1 - J_1)\lambda + \frac{1}{\lambda_1}) = 0. \tag{2.3}$$

The remaining eigenvalues are

$$\lambda_{2,3} = \frac{J_1 - \lambda_1}{2} \pm \sqrt{\mathscr{D}}, \qquad \mathscr{D} = \frac{(J_1 - \lambda_1)^2}{4} - \frac{1}{\lambda_1}, \tag{2.4}$$

where $\mathscr{D}$ is the discriminant. Introducing the parameters ($\mathscr{D}$, λ_1) allows the identification of nine principal regimes, as listed in table 2.1 [18].

	$\lambda_1 > 1$	$\lambda_1 = 1$	$\lambda_1 < 1$
$\mathscr{D} > 0$	I	II	III
$\mathscr{D} = 0$	IV	V	VI
$\mathscr{D} < 0$	VII	VIII	IX

Table 2.1: Parameter regimes of periodic points in three dimensional flows.

Regimes IV and VI accommodate two identical eigenvalues $\lambda_2 = \lambda_3 = \pm 1/\sqrt{\lambda_1}$ and in region V the system exhibits $\lambda_1 = \lambda_2 = \lambda_3 = 1$, constituting the two degenerate cases for which $\mathbf{F}$ is non-diagonalizable. Outside the two degenerate cases, $\mathbf{F}$ has three distinct eigenvalues, implying that it is fully diagonalizable.

For eigenvalue $\lambda_1 = 1$, i.e., regimes II and VIII indicates absence of stretching and compression in the corresponding direction $\mathbf{n}_1$, and designates via $\lambda_2\lambda_3 = 1$ the canonical plane spanned by $\mathbf{n}_{2,3}$ as *area preserving* and thus essentially two dimensional; this behavior is typical of periodic lines [18, 6].

Periodic lines are the three dimensional counterparts of periodic points in two dimensional systems in that they induce effectively two dimensional tracer dynamics in the local plane perpendicular to their tangent. This tangent coincides with the eigenvector $\mathbf{n}_1$, signifying absence of motion in $\mathbf{n}_1$-direction, and further, eigenvectors $\mathbf{n}_{2,3}$ are normal to $\mathbf{n}_1$ and span the before mentioned perpendicular plane; the associated eigenvalues dictate the dynamics within this plane [6].

In the tangent subspace the behavior is governed by the single parameter $J_1^{2D} = J_1 - \lambda_1 = \lambda_2 + \lambda_3$ through $\lambda_{2,3} = J_1^{2D}/2 \pm \sqrt{(J_1^{2D}/2)^2 - 1}$ and permits this subclass of periodic structures to adopt the classification proposed for two dimensional systems. One can distinguish elliptic (VIII), hyperbolic (II) and parabolic (V) periodic lines. Here, quasi-three dimensional effects exist by the spatial variations in J_1^{2D} subdividing a periodic line into elliptic and hyperbolic segments smoothly connected via parabolic points.

In steady systems, periodic points describe closed streamlines on which any constituent point is periodic; such closed streamlines form uniform-type periodic lines (fully elliptic, hyperbolic or parabolic) [2]. Time-periodic systems allow periodic lines with elliptic and hyperbolic segments [18].

In summary, the topological features of periodic lines are

(*i*) Elliptic type ($\mathscr{D} < 0$, $\mathbf{\Lambda} = \{1, e^{i\phi}, e^{-i\phi}\}$), elliptic points on periodic lines form the centres of elliptic islands within the local perpendicular plane that consist of concentric closed orbits along which tracers undergo periodwise rotation at an angle ϕ. In three-dimensions, these islands merge into elliptic tubes centred on elliptic (segments of) periodic lines; such tubes entrap and circulate tracers and thus form barriers to global tracer transport.

(*ii*) Hyperbolic type ($\mathscr{D} > 0$, $\mathbf{\Lambda} = \{1, \lambda, \frac{1}{\lambda}\}$), hyperbolic points on periodic lines are the time-periodic equivalent of saddle points in two dimensional systems; the stable and unstable manifolds delineate the principal transport directions within the local perpendicular plane. Material is elongated along the unstable manifold by a stretching rate $\lambda > 1$ and is compressed along the stable manifold by a compression rate $\frac{1}{\lambda} < 1$. In $3D$, the planar manifolds merge into two dimensional manifolds emanating from hyperbolic (segments of) periodic lines. Transverse manifold intersection leads to exponential stretching of material elements and chaotic tracer advection.

Elliptic and hyperbolic segments on periodic lines are connected by parabolic points ($\mathscr{D} = 0$, $\mathbf{\Lambda} = \{1, 1, 1\}$), these are degenerate points in that, contrary to elliptic and hyperbolic points, in the Poincaré section net fluid motion ceases in their proximity[2] [6].

For the sake of completeness we briefly comment on the other regimes. The eigenvalue spectrum, three distinct eigenvalues, of regimes I, III, VII and IX implies the emergence of an isolated periodic point and a three dimensional behavior, as opposed to the previous cases, where the map was locally area preserving and thus inherently two dimensional.

Isolated periodic points can be typified as node-like ($\mathscr{D} > 0$, $\mathbf{\Lambda} = \{\lambda_1, \lambda_2, (\lambda_1\lambda_2)^{-1}\}$) or focus-like ($\mathscr{D} < 0$, $\mathbf{\Lambda} = \{\lambda, e^{i\phi}/\sqrt{\lambda}, e^{-i\phi}/\sqrt{\lambda}\}$) [41]. See Malyuga et al. [18] for the

[2]This behavior near parabolic points is central for the flow topology in the works of the group of Clercx under weakly inertial conditions.

classification of these four regimes.

Blinking tumbler

Canonical examples of three dimensional chaotic dynamical systems are few, with the more realistic ones being analytically intractable [25]; the blinking spherical tumbler is a linked twist map, specifically, a composition of two *action-action-angle* maps, its mathematical structure is not precisely that of a perturbed integrable Hamiltonian system such as the ABC flows[3] first considered as prototypical 3D chaotic systems [25]. However, the analogy to nonintegrable Hamiltonian dynamics is helpful in understanding the bifurcations of period-one structures on the invariant surfaces of the flow.

Christov et al. [25] studied three dimensional chaotic dynamics in a 'blinking' tumbler granular flow. The authors find analytical expressions for the location of period-one curves. In general, period-one points are significant because they tend to give rise to the largest islands, i.e., regions of material that do not mix with their surroundings. For this system the period-one points lie on curves and their stability is determined by symmetry arguments. The authors refer to these curves as *normally* elliptic and hyperbolic because the elliptic and hyperbolic behavior occurs in planes normal to the period-one curves. Important for our work is the case where both curves intersect.

In a blinking tumbler, the trajectories are restricted to nested invariant surfaces with shape of a portion of a hemispherical "shell" that can be parametrized by the radius. The dynamics on these surfaces are essentially those of a volume preserving map and are similar to those of a one-and-a-half-degree-of-freedom dynamical system. The authors consider important the understanding of the structure of these curves for 3D generalization of elliptic islands and barriers to mixing. The study of stable and unstable manifolds associated with the normally hyperbolic invariant curves made in this system is also interesting for our work.

2.1.3 Symmetries

Symmetries are one of the most powerful tools in the understanding of mixing. They organize the flow topology, as they affect the tracer dynamics (symmetries in the flow field manifest themselves as symmetries in the tracer trajectories [2]), and facilitate identification of coherent structures. Symmetries reflect a degree of order in flows and play an essential role in the topological makeup, they are intimately related to the existence of constants of motion [41].

To determine symmetries when the analytical expressions for maps are not available we can take advantage of geometrical properties [42]. Symmetries exist whenever there are simple geometric constraints on the fluid motion, e.g., system geometry, flow conditions, etc. [43].

[3] These are the spatially periodic Arnold-Beltrami-Childress flows, for more details see [24].

There exist various definitions of symmetry of a map. In general, we say that a map[4] $\mathbf{M}$ posses a symmetry, if there exists a mapping[5] S such that $(\mathbf{M}S)^2 = \mathbf{I}$, with $(S)^2 = \mathbf{I}$ [42]. Both $\mathbf{M}S$ and S are called *involutions* of the map $\mathbf{M}$. If the determinant of the Jacobian of S is equal to -1, the transformation is orientation reversing, and S is said to be a *reflectional symmetry*. On the other hand, if the determinant is equal to $+1$, the transformation is orientation preserving and S is said to be a *rotational symmetry* [42].

The *fixed line* of the symmetry S is defined as a set of points $\{\mathbf{x}\}$ that is invariant upon transformation, i.e., $S\{\mathbf{x}\} = \{\mathbf{x}\}$ [15].

Any orientation reversing transformation contains a set of points that remain invariant upon action of the transformation; these points may form a fixed line associated with the transformation as in the case of two dimensional time-periodic flows studied by Franjione & Ottino [42]. The most important symmetry line of a flow is the fixed line of S because the lowest periodic points will be located either on this line, or, exist in pairs on opposite sides of the line as in the case of the cavity flow.

Mathematically, two maps $\mathbf{A}$ and $\mathbf{B}$ are said to be symmetric to each other if there exists a transformation S such that: $\mathbf{B} = S\mathbf{A}S^{-1}$. If $\mathbf{B} = \mathbf{A}$, the symmetry is termed ordinary; if $\mathbf{B} = \mathbf{A}^{-1}$, the symmetry is termed time-reversal. In general, S can be rotational symmetry or reflectional symmetry. If a map posses symmetry, the periodic points are found in symmetric arrangements [16].

Pouransari et al. [6] discuss two types of symmetries: time reversal reflectional symmetries and ordinary non-reflectional symmetries. If $S = S^{-1}$, we have a reflectional symmetry. Periodic lines are related to time-reversal reflectional symmetries of the mapping $\mathbf{\Phi}$, they are of the form

$$\mathbf{\Phi} = S\mathbf{\Phi}^{-1}S, \quad (S = S^{-1}) \tag{2.5}$$

where S is a map that effectuates reflection about the symmetry plane I_S, defined as $I_S = S(I_S)$. Time-reversal reflectional symmetries as (2.5) imply periodic lines in I_S[6] [6]. The procedure is to release a material surface on the symmetry plane I_s and track it for one period. The intersection of the original and tracked surfaces corresponds with a period-1 line.

Time reversal reflectional symmetries in mappings of the form $\mathbf{\Phi} = \mathbf{\Phi}_n\mathbf{\Phi}_{n-1}...\mathbf{\Phi}_1$, derive from symmetries of the individual steps[7]. Pouransari et al. [6] consider time-reversal and ordinary reflectional symmetries within and between steps.

The following four kinds of reflectional symmetry relations for the forcing steps can be identified

$$\mathbf{\Phi}_i = S\mathbf{\Phi}_i S, \quad \mathbf{\Phi}_i = S\mathbf{\Phi}_i^{-1}S, \quad \mathbf{\Phi}_i = S\mathbf{\Phi}_j S, \quad \mathbf{\Phi}_i = S\mathbf{\Phi}_j^{-1}S, \tag{2.6}$$

[4] We are thinking in time periodic systems where the motion can be written in the form of a mapping, $\mathbf{x}_{n+1} = \mathbf{M}\mathbf{x}_n$. See Appendix A for more information about mappings.

[5] Mappings can be composed, $\mathbf{MM} = \mathbf{M}^2$, $\mathbf{I}$ is the identity map, $\mathbf{M}^{-1}\mathbf{M} = \mathbf{I}$, for more information see [42, 43] and references therein.

[6] In principle, further periodic lines may exist outside the symmetry plane.

[7] Usually, the symmetries of the 'sub-mappings' are more easily determined, and this information can be used to deduce symmetries of the overall map [42].

with i and j indicating different steps.

The second type of symmetries relevant in the present context are ordinary symmetries

$$\mathbf{\Phi} = S\mathbf{\Phi}S^{-1}, \tag{2.7}$$

this symmetries affect the flow topology and tracer dynamics in very specific ways.

2.1.4 Invariant surfaces

Invariant surfaces are surfaces within which tracers remain trapped indefinitely; these surfaces may emanate from either particular symmetries or constants of motion. Pouransari et al. [6] consider only constants of motion without explicit time-dependence ($G = G(\mathbf{x})$) in the context of piecewise steady flows[8].

Constants of motion are quantities G that are preserved by fluid elements during their excursion in the flow domain. They are defined by

$$\frac{dG}{dt} = \mathbf{u} \cdot \nabla G = 0, \quad G(\mathbf{x}) = G(\mathbf{x}_0), \tag{2.8}$$

where $\mathbf{u}\cdot\nabla$ is the derivative in the $\mathbf{u}$ direction at position $\mathbf{x}$. The main idea is that a tracer released at $\mathbf{x}_0$ remains trapped within the surface defined by the surface $G(\mathbf{x}_0)$. In three dimensional flows, constants of motions parameterize families of iso-surface G =constant, within which tracers perform an effectively two dimensional motion [6].

Periodic lines and invariant spheroids are strongly linked in that the latter imply the former [40]. According to [26, Appendix A], Brouwer's fixed-point theorem states that any continuous mapping with convex invariant surfaces must accommodate at least one period-1 point. These period-1 points merge into period-1 lines under a certain condition which follows from the implicit-function theorem.

Bifurcations on intra-surface dynamics

The result of the existence of a constant of motion or a continuous symmetry in a flow field may lead to the existence of invariant surfaces[9], within which effectively 2D flow occurs; for incompressible flows, the intra-surface equations of motion define a Hamiltonian system [26].

In general, islands centered upon elliptic segments of period-1 line consist of closed orbits that coincide with a given surface of the invariant, in consequence, in the local intra-surface frame of reference (ϕ, φ), the map $\mathbf{\Phi}$ is *area-preserving*, meaning that closed orbits identify with level curves of a local Hamiltonian $H(\phi, \varphi)$ and thus tracers are locally governed by

[8] Absence of explicit time-dependence in G implies that these invariant surfaces remain fixed in space at any time.

[9] If a volume preserving map has a continuous symmetry, such as a rotational symmetry, then it has an invariant and the orbits are confined to surfaces [44].

two constant of motion [41, 27]. The situation expressed above will become important when we try to relate bifurcations in our system with those found in Hamiltonian systems.

Hamiltonian systems can undergo an enormous variety of bifurcations, however, the *generic* (not destroyed by small changes in the Hamiltonian) are more restricted [45]. For a Hamiltonian system with one-degree-of-freedom and no symmetry, the generic bifurcation when eigenvalues pass through zero is the 'fish' picture, or saddle-node, see Appendix A.1.

Mullowney et al. [46] study a nonautonomous, three dimensional, incompressible flow corresponding to sequentially active two dimensional rolls with distinct axes. In their model an analytical map is obtained; when the roll axes are orthogonal, motion is confined to two dimensional topological spheres and the dynamics on surfaces ranges from nearly regular to largely chaotic. The idea in this paper is to generalize the Aref's blinking vortex model for a system with three dimensional mixing. These researchers concentrate on two-roll maps, and they remark that from numerical investigations for orthogonal roll arrays three dimensional mixing does not occur and that observation led them to show that an invariant exists. As a result of this fact they visualize orbits of tracers using the angles of spherical coordinates to obtain a two dimensional projection of the dynamics. They also study dynamics near the origin and on the boundary of the cube in terms of normal forms[10]. In this work the authors limit their research for periodic points born at *q-tupling bifurcations*[11] of fixed points. An orbit of the map generically undergoes q-tupling bifurcations when an eigenvalue of the Jacobian matrix passes through the value $e^{2\pi i\omega}$ with $\omega = \frac{p}{q}$ rational. These bifurcations correspond to the creation of new periodic orbits, see [47, 48]. In the first example studied in this work, the authors find the presence of a pair of fixed points on each invariant surface, so they can focus only in one of these points (by symmetry the other point has the same behavior). They find several q-tupling bifurcations, in particuar, *doubling*, *tripling* and *quadrupling* bifurcations are shown [46].

In the case of the blinking tumbler studied in [25], Poincaré sections on different invariant surfaces are shown near a parabolic point; here the dynamics are similar to a perturbed (nonintegrable) Hamiltonian system, a double saddle-node bifurcation is presented (two elliptic period-one points coalesce with two hyperbolic period-one points in a symmetric manner).

2.2 Noninertial case in the lid-driven cylinder flow

In this section we summarize some properties found for the step-wise lid-driven cylinder flow in the non-inertial limit. We present some important features observed in this configuration since other systems, including the present investigation, share them [21, 4].

[10] Normal forms were introduced by Birkhoff for the area-preserving case. The idea of normal forms is to study the asymptotic behavior of a map near a fixed point [46].

[11] These bifurcations are also referred as *k-bifurcations* in the literature, see Appendix A.1. In this work we will use both terms.

The motion within each forcing step is described by the non-dimensional steady Stokes equations

$$\nabla p = \nabla^2 \mathbf{u}, \qquad \nabla \cdot \mathbf{u} = 0. \tag{2.9}$$

The analysis is made in terms of the topological properties of volume-preserving maps [41]. Time-periodic flows admit reduction to volume-preserving maps classified by the number of constants of motion ('actions') they may possess. Three kinds of maps can be distinguished: zero-, one-, and two-action maps[12], see [23, 24] for more about this classification. One-action and two-action maps confine tracers to dense sets of invariant surfaces and curves, respectively. Zero-action maps are devoid of geometrical constraints and admit unrestricted advection. The idea behind this analysis is the identification and possible destruction of the transport barriers of the one and two action maps transforming them into zero-action maps through perturbations[13].

As we have noted, in the lid-driven cylinder flow for the non-inertial limit, with forcing protocols of the lower endwall, the invariant surfaces are topologically equivalent to spheres [6, 41, 27]. They can see $\mathbf{\Phi}_T$ as a one-action map with invariant surfaces other than tori (which is a subclass of volume-preserving maps largely unexplored [41]). Perturbation of one-action maps hitherto appear examined only for invariant surfaces topologically equivalent to tori and gives the 'classical' Hamiltonian scenario: KAM-like survival of non-resonant tori; Poincaré-Birkhoff-type break-up of resonant tori. However, despite their practical relevance, response scenarios of one-action maps with invariant surfaces other than tori received little attention thus far [27].

For the two-step forcing protocol [41, 27], the authors find a period-1 line on one of the symmetry planes ($y = -x$[14]) and two period-2 lines, one within and one symmetric about this plane. The period-1 and period-2 lines intersect at a stagnation point and the two inner parabolic points on the period-1 line. Invariant surfaces are centered around the stagnation point.

Within invariant surfaces, motion is determined by the corresponding intrasurface topologies, which are shaped essentially by the periodic points defined by the intersection of the invariant surfaces with periodic lines[15]. The influence of the period-2 lines is highly localized and they left out of consideration.

As we pointed out in the previous section, periodic points belonging to periodic lines implies the map $\mathbf{\Phi}_T$ is locally area-preserving in their proximity. This has the important implication that the periodic points, and consequently, the associated islands and manifolds, have properties that are essentially the same as found in *area-preserving maps*. This, means that, thought the map is typically non-area-preserving away from the periodic points, the intrasurface dynamics are essentially similar to that of a Hamiltonian

[12] In three-action maps, tracer motion in fully restricted, implying rigid-body fluid motion rather than actual fluid flow [41].

[13] Which for this particular case can be done through the inclusion of inertial terms in the model.

[14] The frame of reference used by the authors has the z direction pointing in the vertical direction.

[15] As the authors point out, spatial variations in properties of periodic lines (elliptic and hyperbolic segments) suggests multiple kinds of intrasurface topologies.

system. Hence the intrasurface dynamics comprise *KAM* tori, island chains, and chaotic regions.

For the lid-driven cylinder flow r_s is defined as the horizontal distance between invariant surfaces and the parabolic stagnation point, this parameter acts as control parameter for the state of the intrasurface topology[16]. The behavior found by increasing r_s is phenomenologically similar to the progressive departure of a generic two dimensional Hamiltonian system from its integrable state by increasing the governing control parameter [41].

For the forcing protocols studied in Pouransari et al. [6], the authors find that the intrasurface motion is essentially equivalent to that of two dimensional time-periodic Hamiltonian systems, they consider three different protocols. Two parameters affect the intrasurface dynamics: the bottom-wall displacement, D, and the distance, r_s, as previously defined. Again the authors see that variations in these parameters result in changes in dynamics (linked with the segmentation of periodic lines) similar to those found upon perturbation of two dimensional Hamiltonian systems.

The evolution with D (for a given invariant surface) is similar to progressive departure from the integrable state of a $2D$ Hamiltonian system; it generally depends nonlinearly on the perturbation parameter in that stronger perturbation must not necessarily result in more chaotic dynamics (existing islands, after diminution, may again grow in size or new islands may form). The authors show here a similar behavior as the period-doubling bifurcation.

For a fixed D, the evolution as a function of r_s has the same Hamiltonian characteristics found with variations of D, that is, nonlinear progression of the flow topology with monotonic variation of the perturbation parameter. An essential difference, however, is that here the progression takes place between two (protocol-independent) integrable states: $r_s = 0$ (stagnation point) and r_s de radius of the cylinder (no-slip boundary).

The authors comment that qualitatively the evolution for all their protocols are similar but differences manifest in the composition of the flow topologies. In general, more elaborate forcing protocols tend to result in more complex topologies. For open protocols chaotic seas grows substantially larger with increasing r_s, typically they cover the entire invariant surfaces. Dynamics become more regular upon approaching the no-slip boundary sets in for higher r_s than for closed protocols. Another highlighted feature is that closed forcing protocols tend to be dynamically more constrained than their open counterparts in the sense that global chaos is less likely to occur and, instead, arrangements of islands remain present.

2.2.1 Area-preserving maps

The notion of an area-preserving map is a valuable tool for studying Hamiltonian systems. These maps can display all the generic properties of nonintegrable Hamiltonian systems

[16] It is not a perturbation parameter in the strict sense though, since it cannot be controlled externally [6].

[49]; for example, typical features of a Henon-Heiles-like surface of section are smooth curves, islands chains, and chaotic trajectories [50, 14].

Following the reasoning of the end of the previous section, we want to present some ideas of chaos in Hamiltonian systems and the Taylor-Chirikov or standard map[17].

Hamiltonian systems form a special case of volume preserving dynamical systems; they conserve volume in phase space and in Poincaré sections (it corresponds to an *area-preserving* map[18]). Systems with one-degree of freedom are *integrable*[19] and cannot be chaotic[20].

The existence of n integrals for integrable systems means that the phase-space trajectories will be confined to a manifold that has the topology of an *n-dimensional torus* [14]. Trajectories on a torus are N *frequency quasiperiodic* (in this case the orbits fill up the torus) if there is no vector of integers $\mathbf{m} = (m_1, ..., m_N)$ such that

$$\mathbf{m} \cdot \omega = 0, \tag{2.10}$$

except when $\mathbf{m}$ is the zero vector, ω is part of the solution of Hamilton's equations in action-angle coordinates, it can be interpreted as an angular velocity vector. For integrable systems, we can view the phase space as being completely occupied by N-tori almost all of which are in turn filled by N frequency quasiperiodic orbits [52]. In contrast with the case of N frequency quasiperiodicity is the case of *periodic motion*, where orbits on the N-torus close on themselves. It can be shown that arbitrarily near any torus on which there is N frequency quasiperiodicity there are tori on which the orbits are periodic[21]. A *rotation number* can be defined so that if it is irrational the trajectories wrap densely around the torus, never intersecting themselves. If this number is rational the trajectory returns exactly to its initial position.

A very fundamental question concerning Hamiltonian systems is how prevalent is integrability? The resolution came with the mathematical work in KAM theorem and with computer studies of chaos and integrability. In terms of the development of the subject of nonlinear dynamics, it is interesting to note that the first Poincaré section computations for nonintegrable Hamiltonians started to appear in the literature at about the same time as the KAM theorem [14].

For perturbed systems the Poincaré-Birkhoff (PB) and the Kolmogorov-Arnold-Moser (KAM) are two very important theorems. A full description of these results is beyond the scope of the present study, here we just present some general ideas. The former describes

[17] The name steaming from its presence in a variety of theoretical and practical problems [14]. The standard map can be derived from the *kicked rotator* system [51].

[18] More precisely, *symplectic* mapping, because the preservation corresponds to a sum of projected areas [14].

[19] A time-independent Hamiltonian H, with N degrees of freedom, is called integrable (also completely integrable) if there exist N independent functions, to be determined, $\{F_i\}$, $i = 1; ..., N$, such that $[F_i, H] = 0$, ($[,]$ is the Poisson bracket; F_i are integrals of motion, one of these is the Hamiltonian itself), and which are in *involution* ($[F_i, F_j] = 0$ for $i, j = 1, .., N$).

[20] Non-integrability is a necessary but not sufficient condition for chaos [10].

[21] For integrable systems the set of tori that have periodic orbits is *dense in the phase space* [52].

the fate of rational tori upon perturbation [14, 52], and the latter studies the local picture of what happens to the irrational orbits in the neighborhood of an elliptic point [10].

In 1954 Kolmogorov outlined a theorem that was subsequently proved by Arnold and Moser since the early 1960s. The central idea in this theorem is to ask what happens to an integrable system under a perturbation (are the tori preserved, destroyed, etc.?), this is of great importance because integrable Hamiltonian systems are exceptional, generic Hamiltonian dynamical systems are not integrable. In this context, we are interested in determining whether the perturbed Hamiltonian has N-dimensional tori to which its orbits are restricted.

A useful paraphrase of the KAM theorem is that 'for sufficiently small perturbation, almost all tori are preserved' [14]. KAM states that under very general conditions, 'most' of the tori of the unperturbed integrable Hamiltonian survive[22] [52].The theorem excludes tori with rationally related frequencies (*resonant tori*), these tori are 'destroyed' under perturbation and provide the 'seeds' of chaotic behavior observed in nonintegrable systems. PB tells us what happens to the rational orbits that disappear (the rational orbits break into a collection of equal number of hyperbolic and elliptic points). Successive applications procedures described by the KAM and Poincaré-Birkhoff fixed point theorems lead to a self-similar structure.

Now, since the resonant tori are 'dense', it is expected that, arbitrarily near surviving tori of the perturbed system, there are regions of phase space where the orbits are not on surviving tori. These regions are occupied by chaotic orbits as well as new tori and elliptic and hyperbolic orbits all created by the perturbation [52].

To complete the the overall picture we have to consider what happens in the neighborhood of the hyperbolic fixed points. As we commented in subsection 2.1.1, hyperbolic points are accompanied by stable and unstable manifolds. These manifolds are not allowed to intersect themselves but, instead, intersect each other. If the intersection point(s) involve the manifolds from the same fixed point, they are called homoclinic points. If the intersecting manifolds emanate from different fixed points, they are called heteroclinic points. The smooth joining of manifolds is the exceptional (i.e., nongeneric) situation that can only arise in integrable systems. Under perturbation the stable and unstable manifolds of an integrable Hamiltonian system intersect transversally and a complex picture appears near the hyperbolic points [10].

To fix ideas we describe the simplest case of a Hamiltonian system, $H = H(p, q)$, namely a system of one-degree of freedom. The essence of any integrable system can be seen in the phase space of the simple pendulum[23] containing two hyperbolic points connected

[22]Here the term 'most' has to be taken in the sense of the *Lebesgue measure*, intuitively, it give us the phase space volume. We say that a torus of the unperturbed system with frequency vector ω_0 'survives' perturbation if there exists a torus of the perturbed system which has a frequency vector $k\omega_0$ (k depends on the perturbation) and such that the perturbed toroidal surface goes continuously to the unperturbed torus as the perturbation goes to zero [52].

[23]All integrable systems with N-degrees of freedom can be transformed into N-uncoupled one-degree of freedom systems, therefore, the main features of an integrable system with N-degrees of freedom is embodied in a system of N non-interacting pendula [10].

smoothly by their stable and unstable manifolds encircling one stable elliptic point.

Under perturbations the stable and unstable manifolds intersect transversally and a complex picture appears near the hyperbolic points (the phase space change showing transverse heteroclinic points). On the other hand, near elliptic points, some orbits disappear, the 'most rational' tori first, each giving rise to a string of elliptic and hyperbolic points with their own stable and unstable manifolds. This picture can be taken as characteristic of all near-integrable chaotic Hamiltonian systems, for more details see [52, 10, 14].

We end this part of the discussion by saying that the standard KAM theorem does not apply to odd dimensional dynamical system, but generalizations of the KAM theorem have been developed and under certain condition may be used to study three dimensional time-periodic flows [19]. For volume preserving-maps there exist the 3D counterparts of KAM and Poincaré-Birkhoff theorems that respectively describe the fate of non-resonant invariant tori and resonant trajectories. Also the formation of invariant manifolds of various topologies due to constants of motion and local and global breakdown of invariant manifolds by resonances are important results in this context [4].

But as we commented in section 1.1.1, the development of a comprehensive Hamiltonian-like theoretical framework for 3D Lagrangian transport, in particular response scenarios to perturbations and routes to chaos, is nonetheless in its infancy [21].

Standard map

The standard map serves as an approximation for several physical systems, most notably the kicked rotor. The standard map can be written as [14]

$$\theta_{i+1} = \theta_i + p_{i+1}, \qquad p_{i+1} = p_i + \frac{k}{2\pi} sin(2\pi\theta_i), \qquad \text{mod} \quad 1. \tag{2.11}$$

The variables p and θ are dimensionless phase space variables (action-angle variables). Both coordinates are periodic with period unity, the map is confined to the unit torus. k is a dimensionless parameter that controls the nonlinearity of the system. In figs. 2.1 and 2.2 we present Poincaré surfaces of section for the standard map for different values of k. The surface of section is produced by choosing several initial points in phase space and then plotting the sequence of points that result from repeatedly applying the map to each initial point.

For $k = 0$ the system is integrable. The intersections of the tori in the (θ, p) surface of section are just lines of constant p (the surface of section consists of trajectories crossing horizontally from $\theta = 0$ to $\theta = 1$ at constant p), see fig. 2.1 (a); on each line the orbit is given by $\theta_n = (\theta_0 + np_0)$ modulo 1. The trajectories correspond to quasiperiodic behavior (a single orbit densely fills the line $p = p_0$) if p_0 is an irrotational number[24], and periodic behavior (the orbits on the line return themselves after a finite number of iterates, and we have a resonant torus) if p_0 is a rational number [52].

[24]Computers deal with rational numbers and only with finite precision, we must take this into account in analyzing surfaces of section [51].

Increasing k from zero introduces a small nonintegrable perturbation. For small k most of the orbits remain slightly distorted versions of the $k = 0$ orbits, there are KAM tori running from $\theta = 0$ to $\theta = 1$; these tori are those that originate from the nonresonant tori of the unperturbed system (p_0 irrational) and have survived the perturbation. Also we can see tori created by the perturbations nested around elliptic periodic orbits originating from resonant tori. In particular, the period one elliptic orbits, $(\theta, p) = (0.5, 0)$ and $(\theta, p) = (0.5, 1)$, and the period two elliptic orbits, (0, 0.5), (0.5,0.5), are visible, see figs. 2.1 $(e) - (f)$. We call the structure surrounding a period p elliptic periodic orbit a *period p island chain*. If the initial condition yields a chaotic orbit (seen as a disorganized scatter of points), then it will wander throughout an area densely filling that area. An important property of two dimensional area preserving maps is that the area bounded by two invariant KAM curves is itself invariant. Thus, while there may be chaotic orbits 'sandwiched' between KAM curves (as, for example, in the island structures surrounding elliptic orbits), these chaotic orbits are necessarily restricted to lie between the bounding KAM curves [52].

As k is increased further, we see that the islands grow, eventually these *resonances* overlap and the KAM tori between them are broken. The overlap of nonlinear resonances leads to chaotic motion [51], this chaotic motion begins in the vicinity of the *separatrix* (the boundary between a nonlinear resonance and the KAM tori that lie just outside).

As k is increased, more of the deformed survivors originating from the unperturbed tori are destroyed. At some point we see that there are none left (there are no tori running as continuous curves from $\theta = 0$ to $\theta = 1$). In their place we see chaotic regions distributed with island chains. As k is increased further many of the KAM surfaces associated with the island chains disappear, and the chaotic region enlarges. At $k = 3$ (fig. 2.2 (c)), for example, we see that the only discernible islands are those associated with the period one orbits.

Increasing even further k, Chirikov numerically found values of k for which there are no discernible tori, and the entire square is (to within the available numerical resolution), covered by a single orbit. Thus, if any island chains are present, they are very small, see fig. 2.2 (d). Some of the invariant tori extending across the phase plane are apparently permeated with small 'holes', this is not a numerical artifact but is, a manifestation of the fact that the invariant curves are not really tori but are the so-called *cantori* (the term has been invoked to suggest the connection with a Cantor-set-like structure) [14].

The absence of a period q island chain at some value $k = k'$, implies that the period q elliptic periodic orbit has become unstable as k increases from 0 to k'. As k increases, the eigenvalues of the qth iterate of the linearized map evaluated on the period q orbit eventually change. The periodic orbit of period q changes from elliptic to hyperbolic with reflection as k passes through some value, k_q[25]. The migration of the eigenvalues leads to a *period doubling bifurcation* and is typically followed by an infinite period doubling cascade. In such a cascade, the period q elliptic orbit destabilizes (becomes hyperbolic)

[25]When a periodic orbit becomes hyperbolic with reflection its eigenvalues in the elliptic range, $e^{\pm i\theta}$, both approach -1 by having θ approach π as k approaches k_q [52].

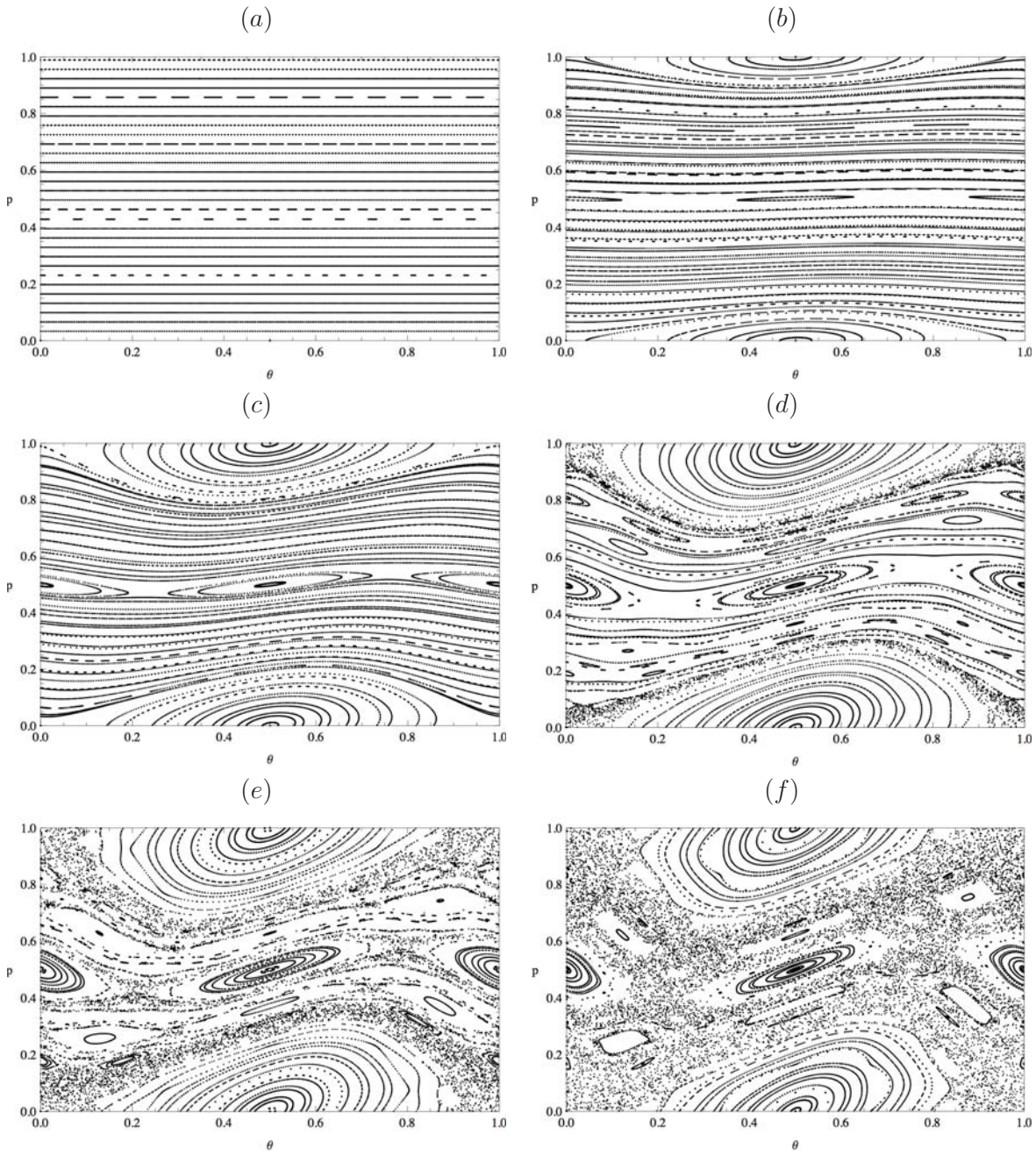

Figure 2.1: Poincaré surface of section for the standard map, the coordinates p and θ are periodic. (a) $k = 0$, (b) $k = 0.1$, (c) $k = 0.4$, (d) $k = 0.8$, (e) $k = 1$, (f) $k = 1.2$.

simultaneously with the appearance of a period $2q$ elliptic orbit, which then period doubles to produce a period 2^2q elliptic orbit, and so on [52].

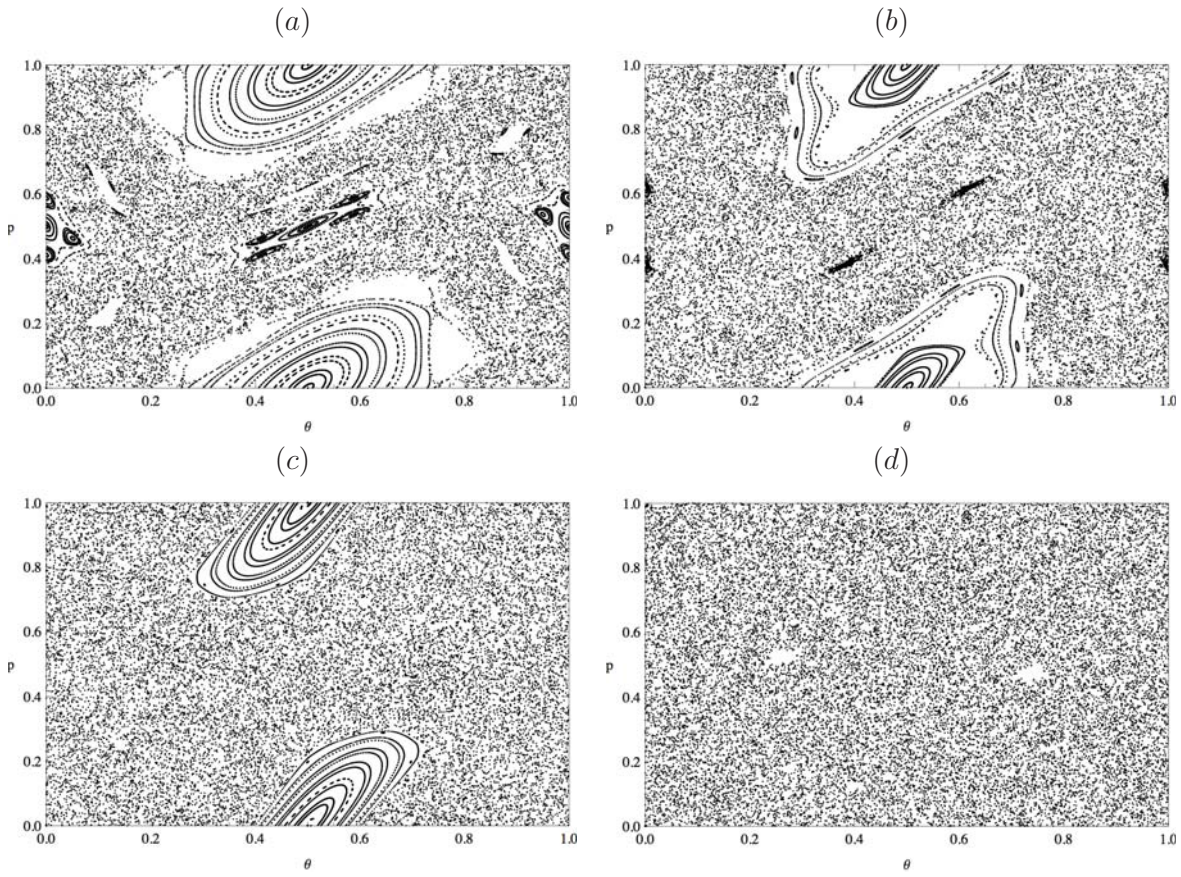

Figure 2.2: Continuation of the previous sequence. Poincaré surface of section for the standard map, the coordinates p and θ are periodic. (a) $k = 1.5$, (b) $k = 2.2$, (c) $k = 3$, (d) $k = 6$.

In summary, when $k = 0$ the standard map is integrable. As k is increased, chaotic regions occupy increasingly large areas, and the original KAM tori of the integrable system are successively destroyed.

A cause of the onset of chaotic motion in area-preserving maps is often attributed to the period-multiplying bifurcation phenomena. When the nonintegrable parameters varies, period-multiplying bifurcations occur by emitting stable and unstable periodic orbits nearby the original orbit. These bifurcations are as important as period-doubling bifurcations for the understanding of the onset of chaotic motion [49]. As we will see in chapter 5, we find bifurcations in this natural convective flow similar to higher order bifurcations studied in area-preserving maps, see [47].

Chapter 3

Convective mixing in three dimensions

In order to give a convenient background to the problem under analysis, let us start this chapter by introducing the problem of a heated vertical flat plate (fig. 3.1). We consider a vertical plate whose temperature T_W is greater than the surrounding fluid temperature T_∞. The heat transferred from the plate to the fluid leads to an increase of the temperature of the fluid close to the wall and to a change in the density because it is temperature dependent. If the density decreases with increasing temperature, buoyancy forces arise close to the wall, and warmer fluid moves up along the plate. The effect of

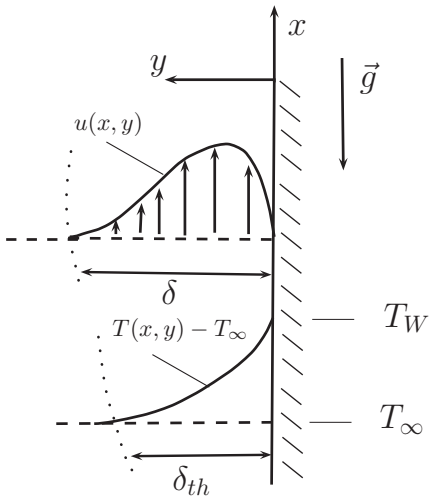

Figure 3.1: Boundary layer at a heated vertical flat plate. We show distributions of velocity and temperature.

the plate is restricted to a thin layer close to the wall (the flow has a boundary-layer character); the thickness, δ_{th}, of the *thermal layer* (the region with $T > T_\infty$) is taken to be the distance from the wall at which the temperature has dropped to within a certain percentage of the outer temperature T_∞ [31].

3.1 Problem statement

We study the mixing properties of a natural convective flow inside a cubic container with time-dependent wall temperatures. The working fluid is Newtonian and the system is in presence of the acceleration of gravity, we can see the frame of reference for the system in fig. 3.3 (a).

The temperature of the vertical walls is time dependent by instantaneously setting one vertical wall, right say, at a hot temperature and keeping it at this condition for a small time interval, the opposite wall temperature, left, is kept at $T = 0$. Then, the left wall is set at a cold temperature and maintained at this temperature for the same time interval while the temperature of the right wall is kept at $T = 0$. Subsequently, this protocol is repeated but with the temperature of the other two vertical walls. For this actual calculation, we determined the time interval by looking at the formation of the invariant surfaces for the trajectories of tracers for the case $\mathrm{Ra} = 1 \times 10^5$, then this time interval was used for all other studied values of the Ra parameter. The forcing protocol is illustrated in fig. 3.2.

The walls that do not participate on the forcing protocol are thermally insulated. In all walls the no-slip condition, $\mathbf{u} = \mathbf{0}$, is imposed. The number of cycles, i.e., repetitions of the protocol, used for each case with constant Rayleigh number was chosen in order to visualize the dynamics on invariant surfaces. In general, the number of cycles required for the analysis, increases for smaller values of Rayleigh number, see chapter 4.

As we have mentioned, in the lid-driven cylinder flow the motion is promoted by the displacement of a wall, i.e., a surface force, in contrast, in natural convection the fluid is set in motion by a convective force which is a volumetric or body force. The dynamical consequences of these two effects are similar insofar the motion in the natural convective flow is mostly concentrated in the boundary layer that forms very close to the vertical wall as in the heated vertical plate.

3.2 Piece-wise steady and linear flow

We consider the piece-wise steady and linear problem, i.e., the conservation equations without the convective terms corresponding to the unsteady, non linear natural convective flow in a cubic box. From equations of subsection 1.2.2 we have that the non-dimensional conservation equations in this case are

$$\frac{\partial u_j}{\partial x_j} = 0, \tag{3.1}$$

$$\frac{\partial p}{\partial x_i} = \mathrm{Pr}\frac{\partial^2 u_i}{\partial x_j \partial x_j} + b_i, \qquad (b_i = (0, \mathrm{PrRa}T, 0)) \tag{3.2}$$

$$\frac{\partial^2 T}{\partial x_j \partial x_j} = 0. \tag{3.3}$$

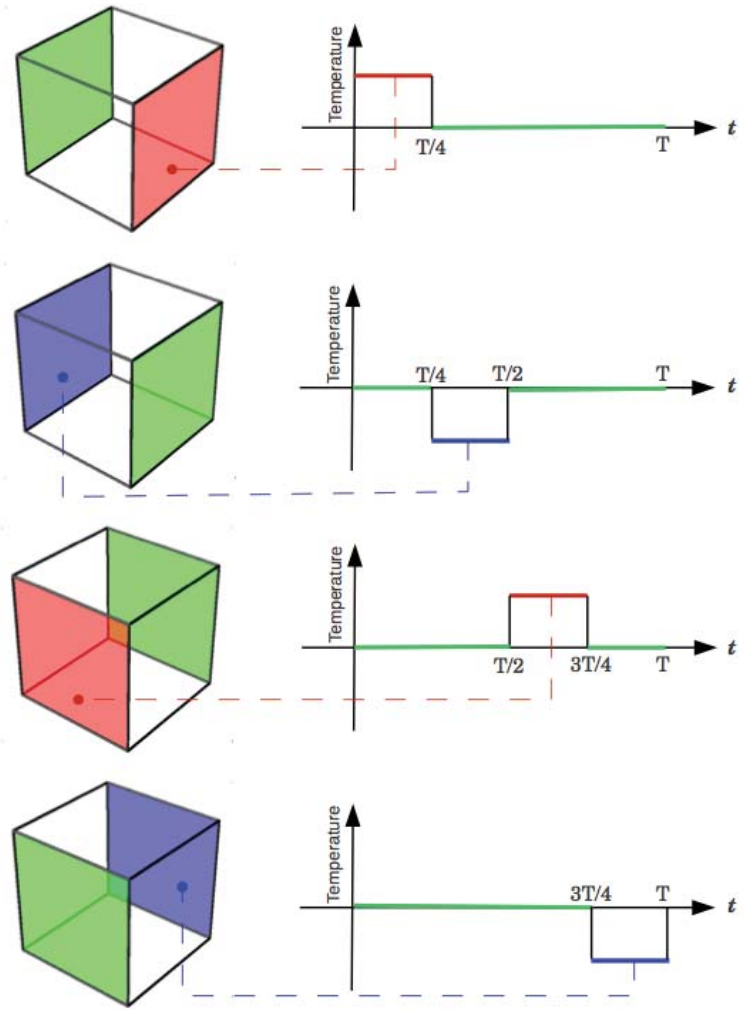

Figure 3.2: Time-periodic wall temperature protocol. In the first half of the cycle, two opposite vertical walls are sequentially kept at a higher and lower temperatures, respectively. In the second half, the temperature of the other two vertical, opposite walls is assumed to take the same time-dependent values. (This figure was made by L. M. de la Cruz).

Recall that we consider a constant Prandtl number, in this work the studied value is $\mathrm{Pr} = 5$, following the work by de la Cruz & Ramos [22]. We will focus on the topological analysis of the flow presented in chapter 2, that is, once the velocity field is calculated we study the advection equation (1.1) in terms of the flow topology. Before that we present some properties of eqs. (3.1)-(3.3). Let us focus in only one quarter of the total cycle, heating one of the vertical walls (the cooling part is very similar). We start by describing the problem in the configuration of fig. 3.3 (b) where z is constant. Boundary condition

for three of the walls are[1]

$$T = A, \quad x = 1; \quad T_y = 0, \quad y = 0, 1. \tag{3.4}$$

Below we consider two possible cases for the boundary condition of the other vertical wall:

1. Adiabatic
$$\frac{\partial T}{\partial x} = 0, \quad x = 0. \tag{3.5}$$

2. Constant temperature
$$T = 0, \quad x = 0. \tag{3.6}$$

As we noted in fig, 3.2 we will use case 2 for the numerical simulations and the topological analysis but we briefly comment the other one because it helps us to understand the fundamental statement of the problem.

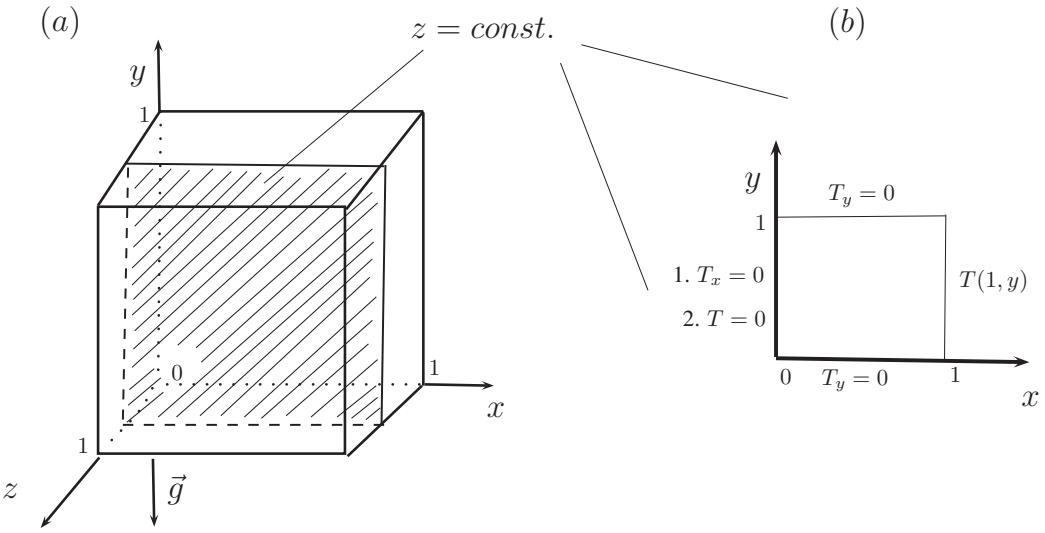

Figure 3.3: (a) Coordinate system for the unitary cube. Heating protocol will be carried out in the vertical walls. (b) Piece-wise steady and linear flow configuration for a plane $z = const.$, with boundary conditions for one quarter of the total cycle.

With this configuration eq. (3.3) is

$$T_{xx} + T_{yy} = 0. \tag{3.7}$$

We look for a solution of the form $T(x, y) = X(x)Y(y)$ as the standard separation of variables method. Note that this is neither an entirely Dirichlet nor a Neumann problem,

[1] In this work we use $A = 0.5$.

but a mixed thermal boundary problem in which T is prescribed on part of the boundary and its normal derivative on the rest. The second derivatives are

$$T_{xx} = X''Y, \qquad T_{yy} = XY'',$$

substituting them in (3.7) and dividing by $T(x, y)$ we get

$$\frac{X''}{X} + \frac{Y''}{Y} = 0, \quad \text{or} \quad \frac{Y''}{Y} = -\frac{X''}{X}.$$

In the last expression the term in one side is only a function of y and the other of x so each term must be equal to a constant[2], $-\lambda$. We get two differential equations with the next boundary conditions

$$Y'' + \lambda Y = 0, \qquad Y'(0) = 0, \quad Y'(1) = 0. \tag{3.8}$$

$$X'' - \lambda X = 0, \qquad \begin{cases} \text{Case 1} & X'(0) = 0, \\ \text{Case 2} & X(0) = 0. \end{cases} \tag{3.9}$$

We will need also $T(1, y) = X(1)Y(y) = A$ from the first condition in eq. (3.4). At this point λ is arbitrary but the boundary value problem (3.8) has non trivial solution $Y(y)$ only if $\lambda = \lambda_n = n^2\pi^2$, $n = 0, 1, 2, ...$, and in that case

$$Y(y) = Y_n(y) = \cos(n\pi y).$$

For the first case in (3.9) we have the differential equation $X'' - n^2\pi^2 X = 0$, with general solution $X(x) = \alpha\cosh(n\pi x) + \beta\sinh(n\pi x)$, and using $X'(0) = 0$, we get $\beta = 0$. Therefore

$$T_n(x, y) = \cosh(n\pi x)\cos(n\pi y), \qquad n = 0, 1, 2, ...,$$

and the function

$$T(x, y) = \frac{c_0}{2} + \sum_{n=1}^{\infty} c_n \cosh(n\pi x)\cos(n\pi y) \tag{3.10}$$

is a solution of (3.7). We must now set the condition $T(1, y) = A$ for obtaining the constants c_n. The series of cosines of a constant is the constant so we have $c_0 = 2A$ as the only non zero constant giving the solution for the first case

$$T_1(x, y) = A. \tag{3.11}$$

Now for the second case in (3.9) $X(x) = \delta\sinh(n\pi x)$, with δ a constant of integration. The difference with previous case is that for $\lambda = 0$ we have the particular solution $T_0(x, y) = k_0 x$, so we get

$$T(x, y) = \frac{c_0' x}{2} + \sum_{n=1}^{\infty} c_n' \sinh(n\pi x)\cos(n\pi y) \tag{3.12}$$

[2]This is a standard result, see for example Boyce & DiPrima [53].

and using the boundary condition we get

$$T_2(x, y) = Ax. \tag{3.13}$$

Equations (3.2) are

$$y\text{-component} \qquad \frac{\partial p}{\partial y} = \mathrm{Pr}\left(\frac{\partial^2 v}{\partial y^2} + \frac{\partial^2 v}{\partial x^2}\right) + \mathrm{PrRa}T \tag{3.14}$$

and

$$x\text{-component} \qquad \frac{\partial p}{\partial x} = \mathrm{Pr}\left(\frac{\partial^2 u}{\partial y^2} + \frac{\partial^2 u}{\partial x^2}\right). \tag{3.15}$$

Now since

$$\frac{\partial}{\partial x}\left(\frac{\partial p}{\partial y}\right) - \frac{\partial}{\partial y}\left(\frac{\partial p}{\partial x}\right) = 0,$$

and using (3.14) and (3.15) in the first case (T is constant)

$$\frac{\partial}{\partial x}\left(\frac{\partial p}{\partial y}\right) = \mathrm{Pr}\left(\frac{\partial}{\partial x}\left(\frac{\partial^2 v}{\partial y^2}\right) + \frac{\partial^3 v}{\partial x^3}\right)$$
$$\frac{\partial}{\partial y}\left(\frac{\partial p}{\partial x}\right) = \mathrm{Pr}\left(\frac{\partial^3 u}{\partial y^3} + \frac{\partial}{\partial y}\left(\frac{\partial^2 u}{\partial x^2}\right)\right),$$

we have

$$\mathrm{Pr}\left(\frac{\partial}{\partial x}\left(\frac{\partial^2 v}{\partial y^2}\right) - \frac{\partial}{\partial y}\left(\frac{\partial^2 u}{\partial x^2}\right) + \frac{\partial^3 v}{\partial x^3} - \frac{\partial^3 u}{\partial y^3}\right) = 0. \tag{3.16}$$

For this two dimensional flow we can use the stream function, ψ and vorticity, ω

$$\omega_z = \frac{\partial v}{\partial x} - \frac{\partial u}{\partial y} = \frac{\partial}{\partial x}\left(-\frac{\partial \psi}{\partial x}\right) - \frac{\partial}{\partial y}\left(\frac{\partial \psi}{\partial y}\right) = -\left(\frac{\partial^2 \psi}{\partial x^2} + \frac{\partial^2 \psi}{\partial y^2}\right).$$

That is, $-\nabla^2\psi = \omega_z = \omega$. We also have

$$\nabla^2\omega = \frac{\partial^2}{\partial x^2}\left(\frac{\partial v}{\partial x}\right) - \frac{\partial^2}{\partial x^2}\left(\frac{\partial u}{\partial y}\right) + \frac{\partial^2}{\partial y^2}\left(\frac{\partial v}{\partial x}\right) - \frac{\partial^2}{\partial y^2}\left(\frac{\partial u}{\partial y}\right) = \tag{3.17}$$

$$= \frac{\partial^3 v}{\partial x^3} - \frac{\partial^3 u}{\partial y^3} + \frac{\partial^2}{\partial y^2}\left(\frac{\partial v}{\partial x}\right) - \frac{\partial^2}{\partial x^2}\left(\frac{\partial u}{\partial y}\right), \tag{3.18}$$

and if we exchange the order of the partial derivatives in (3.16) and comparing the result with the last expression we get

$$\nabla^2\omega = 0. \tag{3.19}$$

Finally, using $-\nabla^2\psi = \omega$ in the last equation, we get

$$\nabla^4\psi = 0. \tag{3.20}$$

Essentially, the same process can be repeated for the second case but we will have an extra term $\partial(A\mathrm{PrRa}x)/\partial x = A\mathrm{PrRa}$, coming from eq. (3.14), to give the expression

$$\frac{1}{A}\nabla^4\psi = \mathrm{Ra}. \tag{3.21}$$

The previous derivation applies for the second quarter of the cycle with $T = -A$, and the second half of the total cycle is equivalent to the first one with a $\pi/2$ rotation. The no-slip condition in the walls results in $\partial\psi/\partial y = -\partial\psi/\partial x = 0$.

Solution to eq. (3.20) is the classical biharmonic problem, which consists in finding a continuous function $\psi(x, y)$, with continuos partial derivatives up to the fourth order and that has prescribed values for it and its normal derivative on the boundary of the domain. Eq. (3.21) is the inhomogeneous biharmonic equation and appears in other problems like for instance, the bending of an elastic rectangular clamped plate. According to the boundary conditions we can define different biharmonic problems, for example, in the theory of elasticity is studied the biharmonic equation for the stress function and the boundary conditions are given for the shear and normal stresses (second order derivatives of the stress function).

Interest in solutions of the biharmonic equation and their mathematical properties goes back over more than 130 years and yet, the biharmonic problem is still challenging in hydrodynamics, linear theory of elasticity, mathematics and engineering [54, 55]. There are various representations of the general solution of the biharmonic equation in terms of harmonic functions (any harmonic function automatically satisfies the biharmonic equation) and in terms of analytic functions of the complex variable.

The way in which the solutions of the biharmonic problems can be obtained is, in principle, similar [56][3]. There are many methods for the solution of such problems and we refer to [54, 56, 57] for more information[4]. As pointed out by Bloor & Wilson [55], an approximate solution is straightforward to obtain but fails to allow the arbitrary level of refinement for the analysis of the physical mechanism.

Superposition method has been widely used for the resolution of biharmonic problems for Stokes flows in a cavity[5]. The idea is to construct the solution in the form of the sum of Fourier series with sufficient functional arbitrariness for fulfilling the boundary conditions. Because of the interdependency, the expressions for a coefficient of a term in one series will depend on all the coefficients of the other series an vice versa, therefore, the final solution involves an infinite system of linear algebraic equations [54].

With the previous comments it may be noted that the solution of equation (3.21) is far from trivial. In our case the difficulties come from the boundary conditions, our goal would be to have a semi analytical solution but at this point a deeper numerical study would be required. We will not follow the path of solving it, however, it may be a very interesting study in the future. A semi analytical solution would provide us with great tools for the study of the flow topology. In the next chapter we present the method for solving equations (3.1)-(3.3) with the finite volume method that is used in this dissertation.

[3]The inhomogeneous biharmonic equation can be reduced to the homogeneous problem by choosing a particular solution, see [57].

[4]A solution of the biharmonic equation (even in a two-dimensional domain) traditionally represents a challenging problem for various analytical and numerical methods. The difficulties come from the boundary conditions imposed on the function and its normal derivatives (first, second or third) [57].

[5]The advantage of the superposition method is the high accuracy that can be obtained with relatively little calculations [56].

Chapter 4

Numerical method for calculating the velocity field and particle tracking

The topological characterization of a mixing flow starts by determining a time-dependent velocity flow. In this chapter we describe the numerical method to solve the equations that describe the flow under analysis.

In this work we use the software *TUNAM*[1] for solving the governing equations of fluid mechanics of natural convection with the finite volume method (FVM). TUNAM was originally developed to simulate natural convection in rectangular domains; it is intended to solve the transport equation (1.17) where ϕ represents a scalar field, temperature, density or a component of the velocity. We solve the natural convection equations in the piece-wise steady and linear case numerically with the FVM using central differences scheme for diffusive terms, and SIMPLER algorithm to decouple the equations. In TUNAM the tools for the unsteady and nonlinear case are also available, QUICK scheme for the advective terms and the SIMPLEC algorithm. Below these tools are briefly described, we mainly follow the exposition made in [37, 58]. Figures 4.1 and 4.2 were made by L.M. de la Cruz.

4.1 Finite Volume Method

The Finite Volume Method (FVM) is the name given to the technique by which the integral formulation of the conservation laws is discretized directly in the physical space. The FVM is based on cell-averaged values, which distinguishes this method from the finite difference and finite element methods, where the main numerical quantities are the local function values at the mesh points [59].

A mesh of the domain is required in the FVM. Once a grid has been generated, the FVM consists in associating a local finite volume, also called control volume, to each mesh point, see fig. 4.1, and applying the integral conservation law to this local volume. The key step in this method is the integration of the general equation over a control volume,

[1] Stands for: Template Units for Numerical Applications and Modeling in computational fluid dynamics and is an open source project. Web page http://code.google.com/p/tunam/.

subsequently different numerical schemes are used for resulting terms. For more details about the method see [38, 60, 59].

Piecewise continuous functions are used for expressing the variations of ϕ between mesh points in the integration. The result of this process is a set of discrete equations for each control volume. Equations have the form of a linear system of algebraic equations that can be solved by iterative solvers [37, 58].

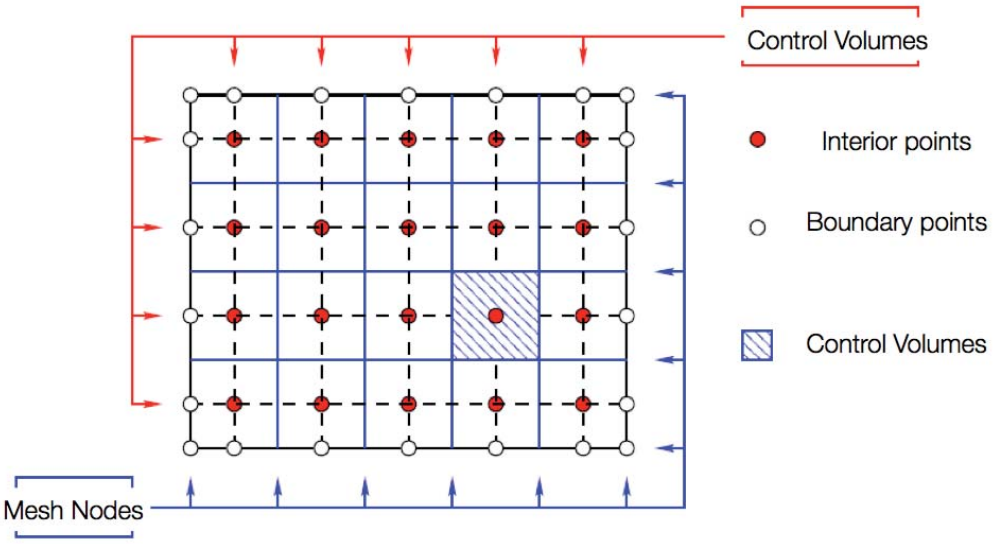

Figure 4.1: Discretized domain using control volumes. In the FVM the discretized space is formed by a set of small cells, one cell being associated to one mesh point.

4.1.1 Discretization

For describing the FVM consider a structured rectangular mesh[2] in three dimensions. Control volumes where eq. (1.17) is integrated are presented in fig. 4.2. The spatial and temporal integration (over the region ΔV and the interval Δt) of the transport equation results in

$$(\phi - \phi^0)\frac{\Delta V}{\Delta t} + \mathbf{C} = \mathbf{D} + \mathbf{S}, \tag{4.1}$$

where ϕ is the value of the variable at time $t + \Delta t$ and ϕ^0 represents the value at the same point at time t. $\mathbf{C}$, $\mathbf{D}$ and $\mathbf{S}$ are the convective, diffusive and source term and depend of the numerical scheme used for discretization. Using a *Backward Euler* scheme (which is a fully implicit scheme), the previous terms are functions of ϕ and have the following form [58]

$$\mathbf{C} = (c_e\phi_e - c_w\phi_w) + (c_n\phi_n - c_s\phi_s) + (c_f\phi_f - c_b\phi_b), \tag{4.2}$$

[2]In a structured mesh every point has the same number of neighbors, except the boundary points.

$$\mathbf{D} = \Gamma\left[\left(\frac{\partial\phi}{\partial x}\right)_e - \left(\frac{\partial\phi}{\partial x}\right)_w\right]\Delta y\Delta z + \Gamma\left[\left(\frac{\partial\phi}{\partial y}\right)_n - \left(\frac{\partial\phi}{\partial y}\right)_s\right]\Delta x\Delta z + \Gamma\left[\left(\frac{\partial\phi}{\partial z}\right)_f - \left(\frac{\partial\phi}{\partial}\right)_b\right]\Delta x\Delta y, \quad (4.3)$$

$$\mathbf{S} = S_P\Delta V. \quad (4.4)$$

The terms of eq. (4.2) are defined by

$$\begin{aligned} c_e &= u_e\Delta y\Delta z, & c_w &= u_w\Delta y\Delta z, \\ c_n &= v_n\Delta x\Delta z, & c_s &= v_s\Delta x\Delta z, \\ c_f &= w_f\Delta x\Delta y, & c_b &= w_b\Delta x\Delta y. \end{aligned} \quad (4.5)$$

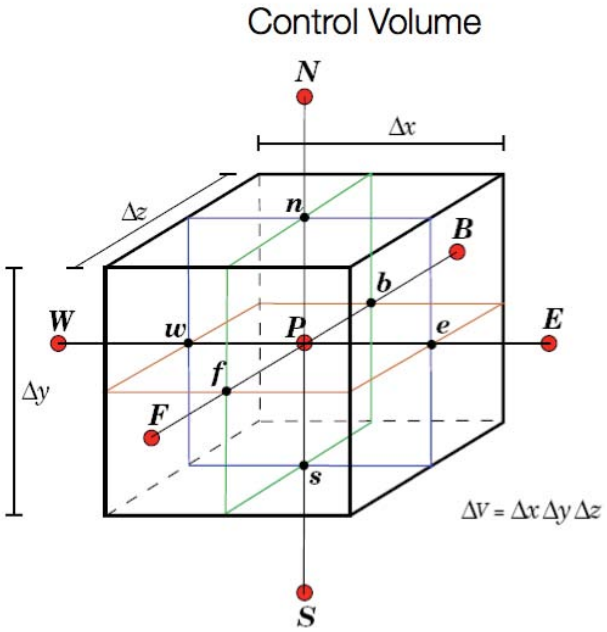

Figure 4.2: Control volume surrounding P. The neighbor nodes are represented by capital letters and small letters denote points on the faces of control volumes. In this way we denote variables evaluated at the center and at the boundaries of volumes respectively.

The convective and diffusive terms can be approximated using different schemes; independently of these approximations when we insert all the terms in (4.1) we get the linear system

$$a_P\phi_P = a_E\phi_E + a_W\phi_W + a_N\phi_N + a_S\phi_S + a_F\phi_F + a_B\phi_B + S_P. \quad (4.6)$$

Here $a_P = D_P + C_P + \frac{\Delta V}{\Delta t}$ and $a_\alpha = D_\alpha + C_\alpha$, being α the six neighbors.

Diffusive terms

Partial derivatives appearing in eq. (4.3) are evaluated in the faces of control volumes; these derivatives are approximated using a linear function between adjacent mesh points. In this way we would have $\left(\frac{\partial\phi}{\partial x}\right)_e \approx \frac{\phi_E - \phi_P}{\Delta x}$, and equivalent expressions for all faces. These expressions yield an approximation of order $\mathcal{O}(\Delta x^2)$ [38]. The diffusive part of (4.6) is given by

$$\begin{aligned} D_E &= \Gamma\frac{\Delta y\Delta z}{\Delta x}, & D_W &= \Gamma\frac{\Delta y\Delta z}{\Delta x}, \\ D_N &= \Gamma\frac{\Delta x\Delta z}{\Delta y}, & D_S &= \Gamma\frac{\Delta x\Delta z}{\Delta y}, \\ D_F &= \Gamma\frac{\Delta x\Delta y}{\Delta z}, & D_B &= \Gamma\frac{\Delta x\Delta y}{\Delta z}, \end{aligned} \tag{4.7}$$

. (4.8)

and D_P results from the sum of the previous terms.

Convective terms

The variable ϕ represents a scalar variable defined at the center of volumes but in eq. (4.2) it is evaluated at the cell faces. Different schemes exist in order to approximate the value of ϕ at these points such as upwind, central differences and QUICK (Quadratic Upstream Interpolation for Convective Kinematics). Convective terms need to be carefully calculated as they are the nonlinear part of momentum equations.

The upwind scheme takes into account the flow direction when determining the value at a cell face: the convected value of ϕ at a cell face is taken to be equal to the value at the upstream node [38]. This scheme gives an approximation of first order $\mathcal{O}(\Delta x)$. Central differences scheme consists in evaluating ϕ at the faces using a linear interpolation and is of second order $\mathcal{O}(\Delta x^2)$.

QUICK is an upwind scheme of third order, $\mathcal{O}(\Delta x^3)$, where three points of the mesh are chosen in order to build a second order polynomial. Points are selected according the direction of the velocity in the corresponding face of the control volume. The final expressions for the convective coefficients can be found in the references, see for example [38, 37].

Boundary conditions

In our heating protocol there exist two types of boundary conditions

- Dirichlet: the value of the scalar field is given at the boundary, that is, $\phi = \phi_b$.
- Neumann: the value of the normal derivative of scalar field is specified, $\frac{\partial\phi}{\partial n} = \phi'_b$.

Boundary condition are incorporated to the system of equations to be solved and different approximations can be used depending on the order of the numerical scheme used for the interior points [37].

4.1.2 Pressure correction methods

A central problem with the numerical integration of Navier-Stokes equations is that there is no equation for the pressure. A way to overcome this situation is to use SIMPLE (Semi-Implicit Method for Pressure Linked Equations) methods. In this context *staggered grids* are widely used. The idea is to evaluate scalar variables such as pressure and temperature in the centers of control volumes while velocities are taken at the faces of volumes.

SIMPLE

SIMPLE is a guess-and-correct procedure for the calculation of pressure on the staggered grid arrangement. To illustrate in a very general way the method, let us consider the FVM applied to the momentum conservation equation for u in the staggered grid. In this way we get [37]

$$a_P u_P = \sum_{nb} a_{nb} u_{nb} + b_u + A_u(p_W - p_P), \tag{4.9}$$

where nb represents the neighbors in the arrangement of the staggered mesh, A_u, is the face area of the control volume where the pressure force is acting and, b_u, is the source term. We can write similar equations for each velocity component. As the pressure field is unknown, we need a method for calculating it. The idea of the SIMPLE algorithms is to solve the velocity equations with an initial guessed pressure field p^* that will produce an approximate velocity u^* as follows

$$a_P u_P^* = \sum_{nb} a_{nb} u_{nb}^* + b_u + A_u(p_W^* - p_P^*). \tag{4.10}$$

In general, the solution u^*, does not satisfy the continuity equation. In a second step we correct the guessed pressure until the resulting velocity field satisfies the continuity equation. Let p' and u' be the pressure and velocity correction respectively, they are the difference between correct and guessed fields such that

$$p = p^* + p' \qquad u = u^* + u'. \tag{4.11}$$

We have a similar expressions for all the velocity components. From equations (4.9)-(4.10) we get an expression for p' and u'

$$a_P u_P' = \sum_{nb} a_{nb} u_{nb}' + A_u(p_W' - p_P'). \tag{4.12}$$

Different ways of handling the term $\sum_{nb} a_{nb} u_{nb}'$ (and the corresponding terms for other components of the velocity) define various methods of the SIMPLE family. For SIMPLE

the approximation is the omission of these terms for each velocity components. With this approximation we get expressions for the correct velocity field in terms of p'. By using the continuity equation with these expressions we can get the discretised continuity equation as an equation for the pressure correction p'. The source term of this equation will be the the continuity imbalance arising from the incorrect velocity field. By solving this equation the pressure correction field is known and we can get the correct pressure field by using eq. 4.11 and finally the correct velocity components through the correction formulae.

The pressure correction equation is susceptible to divergence unless some under-relaxation is used during the iterative process. The idea is to add a multiplicative factor to the pressure correction variable [38].

SIMPLER (SIMPLE Revised) is an improved version of SIMPLE. In this algorithm the discretised continuity equation is used to derive a discretised equation for pressure (instead of a pressure correction equation as in SIMPLE). The intermediate pressure field is obtained directly without the use of a correction. Velocities are, however, still obtained through the velocity corrections and p' equation must also be solved. For a detailed description of the algorithms SIMPLER and SIMPLEC see [38].

4.1.3 Linear systems solution

As we have seen in the previous sections, discretization of the governing equations results in a system of linear algebraic equations which need to be solved. The complexity and size of the set of equations depends on the dimensionality of the problem, the number of grid nodes, etc.

There are two families of solutions techniques for the resolution of linear algebraic systems: indirect or iterative and direct methods. Examples of direct methods are Gaussian elimination and Cramer's rule matrix inversion. Examples of iterative methods are Jacobi and Gauss-Seidel point-iterative methods [38].

The TDMA is a direct method based on a technique developed by Thomas for rapidly solving tridiagonal systems. TDMA is actually a method for one-dimensional situations, but it can be applied iteratively, in a line-by-line procedure, to solve multi-dimensional problems and is widely used in CFD simulations [38]. In TUNAM the TDMA method is available an we refer to the previous reference for more details.

In summary, using the finite volume method we obtain the velocity, pressure and temperature fields as functions of space and time. In Appendix B we present the incompressibility constraints for the velocity fields used in this work and show also the size of the meshes for each case. As we study the piece-wise steady and linear flow we do not take into account the transient states, the boundary conditions were given in chapter 3.

4.2 Coherent structures

The tools needed for particle tracking inside the natural convective flow and the construction of the invariant surfaces are available in TUNAM. Below we briefly discuss the general idea of these tools and also present the searching algorithm of periodic points and the method for their classification.

4.2.1 Particle tracking

The solution of balance equations constitutes only a first but important step in this work. With the discrete velocity field calculated on each point of the mesh it is possible to track massless particles inside the flow based on a numerical integration of the equation (1.1).

A general particle tracking must perform the following actions for every time step [61]:

1. Locate the particles inside de container.
2. Interpolate the velocity to the positions of the particles.
3. Integrate the equation (e.g., Fourth order Runge-Kutta scheme).

The last two steps are the most important because introduce accumulative numerical errors. A trilinear interpolation of the velocity is used, in such a way that the accuracy depends on the size of the mesh.

For reliable numerical integration of kinematic equation (1.1) higher-order algorithms are mandatory. In the framework of this dissertation a fourth-order Runge-Kutta scheme is used [62]

$$\mathbf{k}_1 = \mathbf{u}(\mathbf{x}_m, t_m), \qquad \mathbf{k}_2 = \mathbf{u}(\mathbf{x}_m + \mathbf{k}_1 \tfrac{\Delta t}{2}, t_m + \tfrac{\Delta t}{2})$$

$$\mathbf{k}_3 = \mathbf{u}(\mathbf{x}_m + \mathbf{k}_2 \tfrac{\Delta t}{2}, t_m + \tfrac{\Delta t}{2}), \qquad \mathbf{k}_4 = \mathbf{u}(\mathbf{x}_m + \mathbf{k}_3 \Delta t, t_m + \Delta t)$$

$$\mathbf{x}_{m+1} = \mathbf{x}_m + \frac{\Delta t}{6}(\mathbf{k}_1 + 2\mathbf{k}_2 + 2\mathbf{k}_3 + \mathbf{k}_4). \tag{4.13}$$

4.2.2 Invariant surfaces

The invariant surfaces are found by releasing many particles on different initial position and tracking them inside the flow. In this work we started by tracking initial tracers positioned in a diagonal from the center of the cube (the center of the cube is stagnation point) to near a corner of the container. Specifically, the line of initial points goes from the point with coordinates (0.501, 0.501, 0.501) to the point (0.85, 0.85, 0.85). We do not extend the analysis to the corner of the cube in order to avoid lack of precision at the boundary layer.

We start with 100 tracers to construct 100 surfaces. All of these surfaces are topologically equivalent to spheroids, they are slightly flattened near top and bottom walls. We do not have an analytical solution of the velocity field and we must calculate the surfaces numerically. The procedure to find these surfaces is as follows:

1. Define the initial position of a particle.
2. Follow the particle for a short number of cycles (20 is a typical number).
3. Take a representative number of points on this trajectory.
4. Build Poincaré maps for the previous number of points for a large number of cycles (typical values range from 200-700) in order to visualize the dynamics of invariant surfaces.

In step 1 we determine a particular invariant surface. In step 2 we only use few cycles in order to reduce the numerical errors in the construction of the surface.

4.2.3 Periodic points

The idea for a formulation of a generic search algorithm of periodic points is outlined below. We define a displacement function

$$d\mathbf{X}(\mathbf{x}) = \mathbf{x} - \mathbf{\Phi}_T^k(\mathbf{x}), \tag{4.14}$$

which represents the displacement vector between the material point $\mathbf{x}$ and the k-th forward mapping $\mathbf{\Phi}_T^k(\mathbf{x})$. The period-$k$ points, $\mathbf{x}_0^{(k)}$, coincide with the roots of eq. (4.14) ($d\mathbf{X}(\mathbf{x}_0^{(k)}) = \mathbf{0}$). One way of finding the roots rests on the fact that $d\mathbf{X}(\mathbf{x})$ and the euclidean norm ($dX(\mathbf{x}) = |d\mathbf{X}(\mathbf{x})|$) share the same roots [20]. The idea of the searching algorithm is to find points in which $d\mathbf{X}(\mathbf{x})$ reaches a minimum.

For this work a searching algorithm was developed, the searching procedure focused in points laying at the intersection of the invariant surfaces and symmetry planes.

Period-1 lines

For the identification of periodic lines of period 1, we calculate the intersection of invariant surfaces with symmetry planes and track the points of the intersection for one cycle looking for minimum values of $dX(\mathbf{x})$. A general procedure for isolation of periodic points can be found in [26, Appendix B].

We can verify the existence of periodic lines by the eigenvalues of the linearized deformation tensor, recall the discussion in 2.1.2.

Classification of periodic points

The classification of fixed points for time-periodic systems is based on the eigenvalues of the linearized deformation tensor ($\mathbf{F} = \frac{\partial \mathbf{\Phi}_T}{\partial \mathbf{x}}|_{\mathbf{x}_0}$). For the numerical evaluation of the tensor at arbitrary point $\mathbf{x}_0$ we define six surrounding material nodes [62]

$$\mathbf{x}_1^{(+,-)} = \mathbf{x}_0 + (\pm\delta, 0, 0), \quad \mathbf{x}_2^{(+,-)} = \mathbf{x}_0 + (0, \pm\delta, 0), \quad \mathbf{x}_3^{(+,-)} = \mathbf{x}_0 + (0, 0 \pm \delta), \tag{4.15}$$

through which the entries of $\mathbf{F}$ follow from the central difference scheme

$$F_{ij} = \frac{\partial f_i}{\partial x_j} = \frac{f_i(\mathbf{x}_j^{(+)}) - f_i(\mathbf{x}_j^{(-)})}{2\delta} \qquad i, j = 1, 2, 3. \tag{4.16}$$

We have defined $\mathbf{f}(\mathbf{x}) = \mathbf{\Phi}_T(\mathbf{x})$. This way of calculating numerically the elements of the matrix is equivalent to the approach taken by Krasnopolskaya et al. [63]. For solenoidal velocity fields, the requirement $\det(\mathbf{F}) = 1$ is an accuracy test.

In this work we use $\delta = 1 \times 10^{-3}$ for all Ra except for the case $\mathrm{Ra} = 5 \times 10^5$ where we reduced it to $\delta = 5 \times 10^{-4}$ for the periodic points located away from the center of the cube, see section 5.1.4.

Chapter 5

Results

In this chapter we present the the main topological properties found for the natural convective piece-wise steady and linear flow. We follow the presentation made in chapter 2. We start by considering qualitatively the symmetries of the flow taking into account the similarities with the forcing protocols of the lid-driven cylinder flow. We then present the main intra-surface dynamics found on invariant surfaces, the periodic lines found on symmetry planes and their classification for the studied values of Ra parameter.

5.1 Flow topology

5.1.1 Symmetries

Velocity field

The main feature of the velocity field for each quarter of the forcing protocol is the formation of a vortex in the center of the cube. The position of the vortex is apparently maintained when we pass from the first quarter of the protocol (heating) to the second quarter (cooling). This pattern is shown in fig. 5.1. The behavior for the second half of the cycle is equivalent for the other two opposite walls, with a $\pi/2$ rotation. This behavior is similar for all explored values of Ra. From the velocity field we see the generation of blinking vortices each half of the protocol. We can think that the first half of the protocol, $\mathbf{F}_1$, is the basis of our heating forcing since $\mathbf{F}_2 = S_{\frac{\pi}{2}}\mathbf{F}_1$, being $\mathbf{F}_2$, the second half of the protocol and $S_{\frac{\pi}{2}}$, the rotation of $\pi/2$. The effect of applying $\mathbf{F}_1$ produces the motion of the fluid about the center of the cube. Qualitatively, the effect is similar to the displacement of the bottom wall in the lid-driven cylinder flow. This is called the steady base flow since all the forcing steps can be reduced to it via rotations and reflections, where they find closed streamlines [2, 21].

The first half of the protocol $\mathbf{F}_1$ consists of a heating and a cooling part. The application of $\mathbf{F}_1$ produces the movement illustrated in fig. 5.2 (a). We can focus on the motion near the planes $y = 0$ (bottom wall) and $y = 1$ (top wall). The effect of $\mathbf{F}_1$ is similar to the displacement of the top wall in the $-x$ direction and the movement of the bottom wall in $+x$ direction. When we apply $\mathbf{F}_2$, we can make also the analogy with the displacement of walls, the top wall moves in the $-z$ direction and the bottom wall in $+z$ direction, see fig. 5.2 (b).

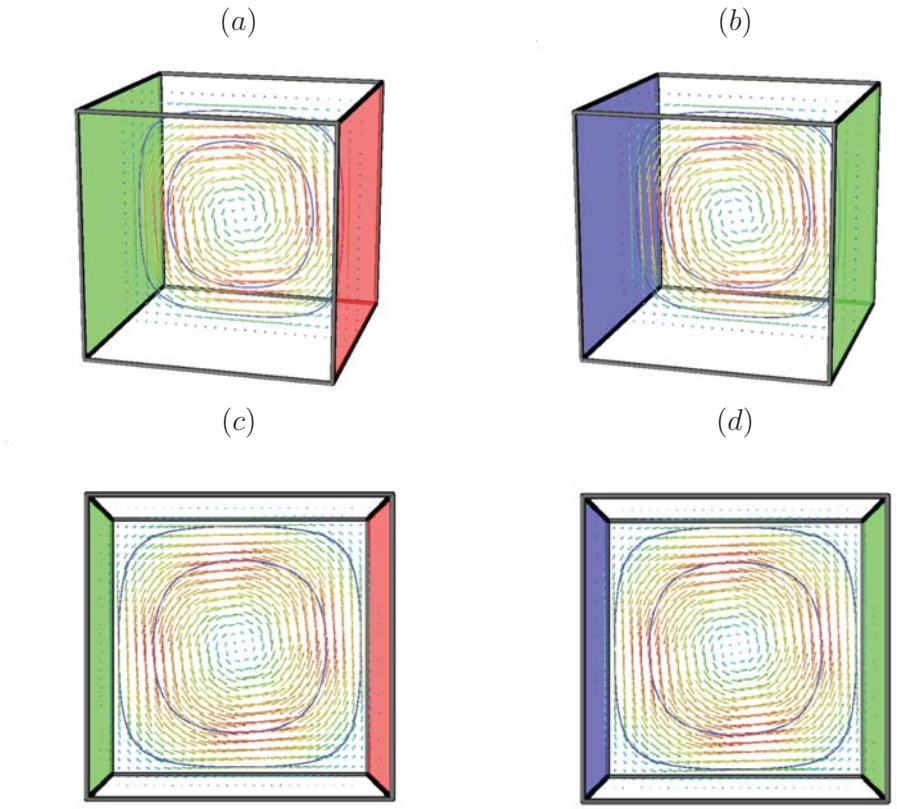

Figure 5.1: Velocity fields for the first half of the forcing protocol. Two streamlines and the temperature distribution for the middle z plane are also shown. The origin of the frame of reference is located at the lower left corner at the back of the cube, the z direction is pointing to the front of the cube. (a) First quarter of the forcing protocol and (b) second quarter of the forcing protocol for $\mathrm{Ra} = 7 \times 10^4$ and a mesh of 96^3 from a diagonal view. (c) First quarter of the forcing protocol and (d) second quarter of the forcing protocol for $\mathrm{Ra} = 9 \times 10^4$ and a mesh of 128^3 from a frontal view.

Making this analogy we can think in our heating protocol in the same way as lid-driven cavity flows. The deduction of symmetries for the square cavity with alternate movements of two opposite walls can be found in the work of Franjione et al. [42] and for the alternate movements of a wall in perpendicular directions in [2]. As we can see from fig. 5.2 (b), we have a sort of combination of the two cases.

For the alternate movement of a wall in perpendicular directions there exist a time-reversal reflectional symmetry that hosts a period-1 line [2, 6]. With the previous discussion we will focus on the searching of periodic points on the planes[1] $x = 1 - z$ and $x = z$, see

[1]The exploration of the plane $y = 0.5$ can also be of interest.

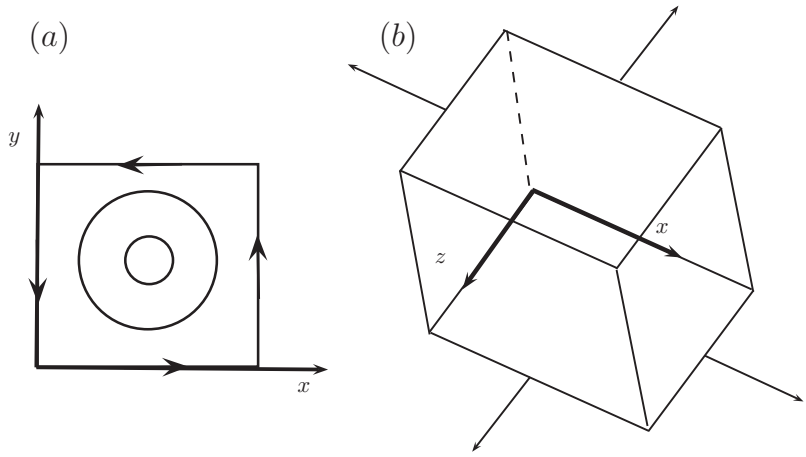

Figure 5.2: (a) Qualitative flow produced by the application of first half of the protocol $\mathbf{F}_1$ (this is a sketch of the general behavior and not an exact representation). (*b*) Analogy of the heating protocol with movement of walls.

subsection 5.1.3. In this work we don't present a rigorous and exhaustive study of the symmetries of this heating protocol and we have it in mind for the future.

5.1.2 Invariant surfaces and intra-surface dynamics

We studied invariant surfaces and their dynamics for Ra numbers of $3{\times}10^4$, $5{\times}10^4$, $7{\times}10^4$, $9{\times}10^4$, $1{\times}10^5$ and $5{\times}10^5$. For the piece-wise steady and linear flow we find axisymmetric invariant surfaces that are topologically equivalent to spheres, similar to those found for the lid-driven cylinder flow [41, 6], the three-dimensional sphere-driven flow [26] and the blinking rolls flow [46]. In fig. 5.3, we show a typical orbit of a tracer that lies on an invariant spheroid and the Poincaré map.

We make a parametric study of the dynamics; we discuss the most important structures found for each Ra and present them in the cases where their formation is more clearly visualized. We have two important parameters, Ra and the radius. We define the radius as the distance from the center of the cube to the point in the diagonal that was used to generate the invariant spheroid, recall the discussion in section 4.2. Different behaviors are present for several values of Ra at different radii. In particular, we emphasize the behavior near critical points when the radius of the invariant surfaces is slightly changed. Unless otherwise noted, we will always change the radius from a surface to the following one with an increment of $\Delta r \approx 0.006$, this increment is taken along the diagonal of the initial tracked points, see section 4.2. In each sequence of surfaces we maintain the scale of the figures. Similar bifurcations to those found for Hamiltonian systems with symmetry and area-preserving maps are presented. We are specifically thinking in the dynamics presented by Golubitsky & Stewart [45], see Appendix A.1.

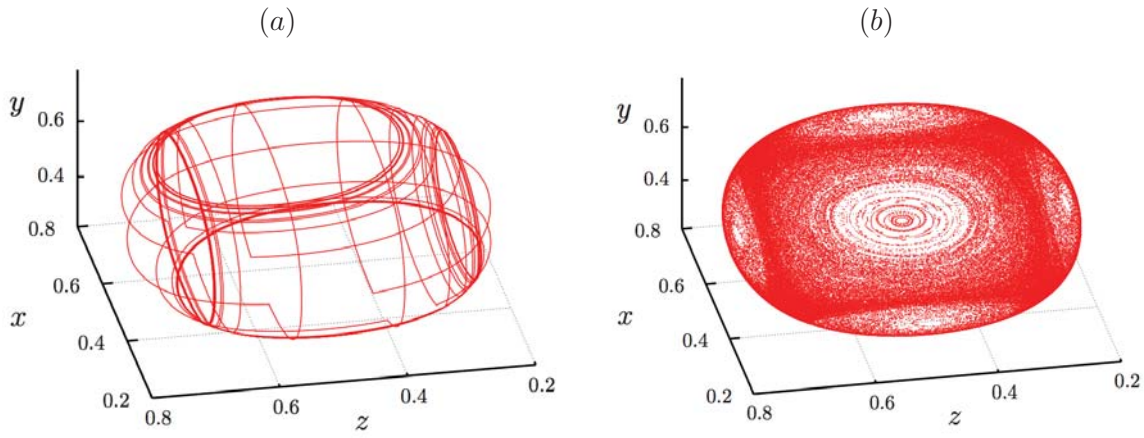

Figure 5.3: (a) Typical Lagrangian orbit of a tracer for 20 cycles. (b) Poincaré map built from (a) for 200 cycles. Ra $= 1 \times 10^5$ and radius $= 0.307$.

We present the dynamics in order of increasing Ra and show different views of invariant surfaces in order to be as descriptive as possible. At the end of all the cases we summarize the intra-surface dynamics in function of Ra and the radius.

Rayleigh number 3×10^4

In all cases except for Ra $= 5 \times 10^5$ we find on the invariant surfaces two elliptic points symmetrically arranged that are present all over the studied region of the container[2]. In fig. 5.4 (a) we show the Poincaré map on a typical invariant surface; we have colored the points in Poincaré section in order to highlight the fact that elliptic points are located at opposite sides of the surface. In fig. 5.4 (b) we show two axisymmetric surfaces where their common center is the center of the cube.

At specific radii we find that elliptic and hyperbolic points appear surrounding the two elliptic points previously mentioned, we will refer to this behavior as *k-bifurcations* or *q-tupling bifurcations* following [46, 25, 48]. This phenomenon generally starts at the central region of the surfaces. In fig. 5.5 (a) we show an invariant surface just before the appearance of points forming a *five-tupling* bifurcation (or 5-bifurcation). In fig. 5.5 (b) we decreased the radius from panel (a). In fig. 5.6 (b) we see another perspective of this surface from a top view where we have added the two planes considered in this work. For clarity, in fig. 5.6 (a), we show the position of the elliptic points about the plane $x = 1 - z$. Changing the radius of invariant surfaces produces a similar behavior to changing the perturbation parameter in k-bifurcation points. This is demonstrated in

[2]This behavior is similar to the arrangement of periodic points, and hence islands, in the flows with reflectional symmetry discussed by Franjione & Ottino [43]. The periodic points must exist along the line of symmetry, or in pairs on opposite sides of the line.

figs. 5.7 - 5.8. This structure is very similar to the bifurcations of Hamiltonian systems for the case $\mathbb{Z}_5$, see Appendix A.1. For this value of the parameter we find also 7 and 9-bifurcations at larger radius[3], see table 5.1.

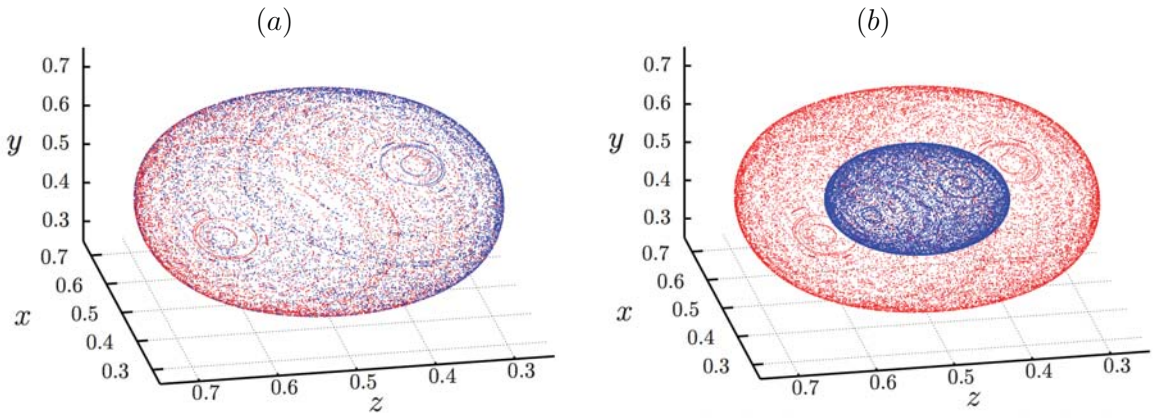

Figure 5.4: Poincaré maps on invariant surfaces for $\mathrm{Ra} = 3 \times 10^4$. (a) Typical invariant surface exhibiting two elliptic points symmetrically arranged, radius = 0.239. (b) Settlement of nested invariant surfaces, red surface corresponds to the one in (a) and the radius of the blue one is 0.117.

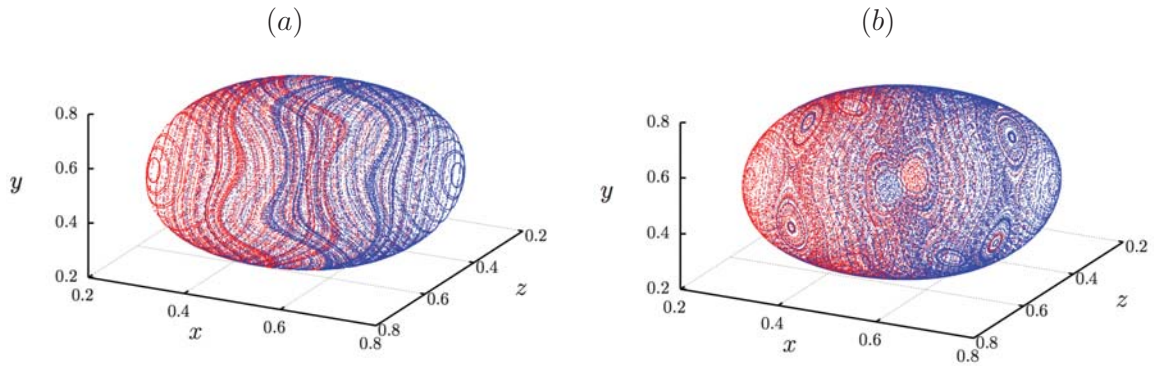

Figure 5.5: $\mathrm{Ra} = 3 \times 10^4$. Appearance of elliptic and hyperbolic points near the central region of surfaces. (a) Radius = 0.307. From (a)-(b) we decrease the radius of the invariant surface.

[3]As described in Appendix A.1 the behavior of bifurcations for $m \geq 5$ is similar.

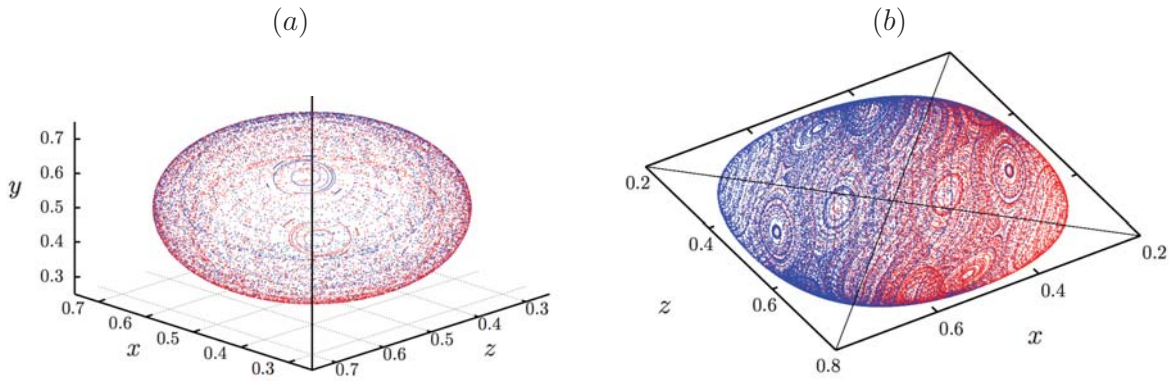

Figure 5.6: Ra $= 3 \times 10^4$. Position of invariant surfaces and planes of analysis. (a) Invariant surface of fig. 5.4 (a) and $x = 1 - z$ plane (central line from this view point). (b) Invariant surface of fig. 5.5 (b) and the considered planes from a top view.

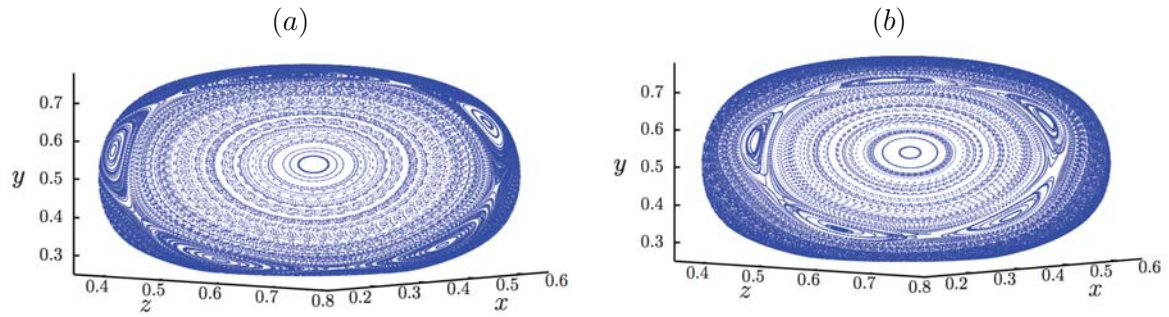

Figure 5.7: Ra $= 3 \times 10^4$. Typical behavior near a 5-bifurcation point, i.e., presence of an elliptic and hyperbolic periodic-5 orbit surrounding one of the elliptic points. This is another view of fig. 5.5 (b) emphasizing the behavior near one of the elliptic points. From (a)-(b) we decrease the radius of the invariant surface.

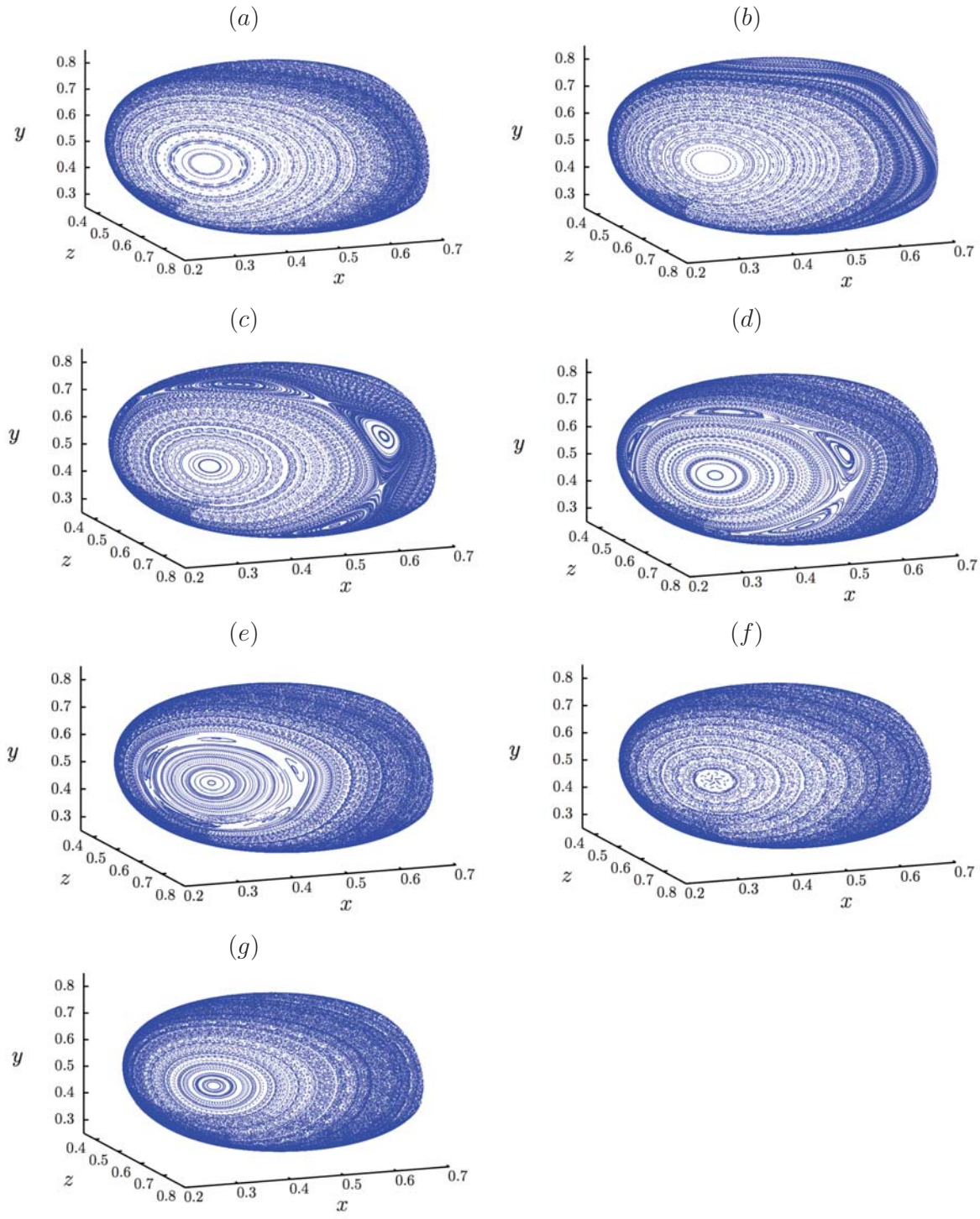

Figure 5.8: Ra $= 3 \times 10^4$. Different view of the five-tupling bifurcation. In (a)-(g) the radius of the invariant surfaces decreases. The radius in (a) is 0.3131 and the radius in (g) is 0.2764.

Rayleigh number 5×10^4

For this Rayleigh number we also find the 5-bifurcation described in the case of Ra $= 3 \times 10^4$ but for a larger radius. This tendency will be present for the whole range of Rayleigh numbers explored excepting Ra $= 5 \times 10^5$; we find similar intra-surface topologies but at larger radius for larger Ra.

In contrast to the case Ra $= 3 \times 10^4$, a different geometric feature found for Ra $= 5 \times 10^4$ is a 3-bifurcation, this is similar to the case of Hamiltonians with $\mathbb{Z}_3$ symmetry, see Appendix A.1. We can see a sequence of the formation of this structure near one of the elliptic points in figs. 5.9 - 5.10. Another perspective of the formation of hyperbolic/elliptic points is presented in fig. 5.11. Here in $(a) - (d)$ we can see a 'fish' type bifurcation for the three pairs of elliptic-hyperbolic points formed, see Appendix A.1.

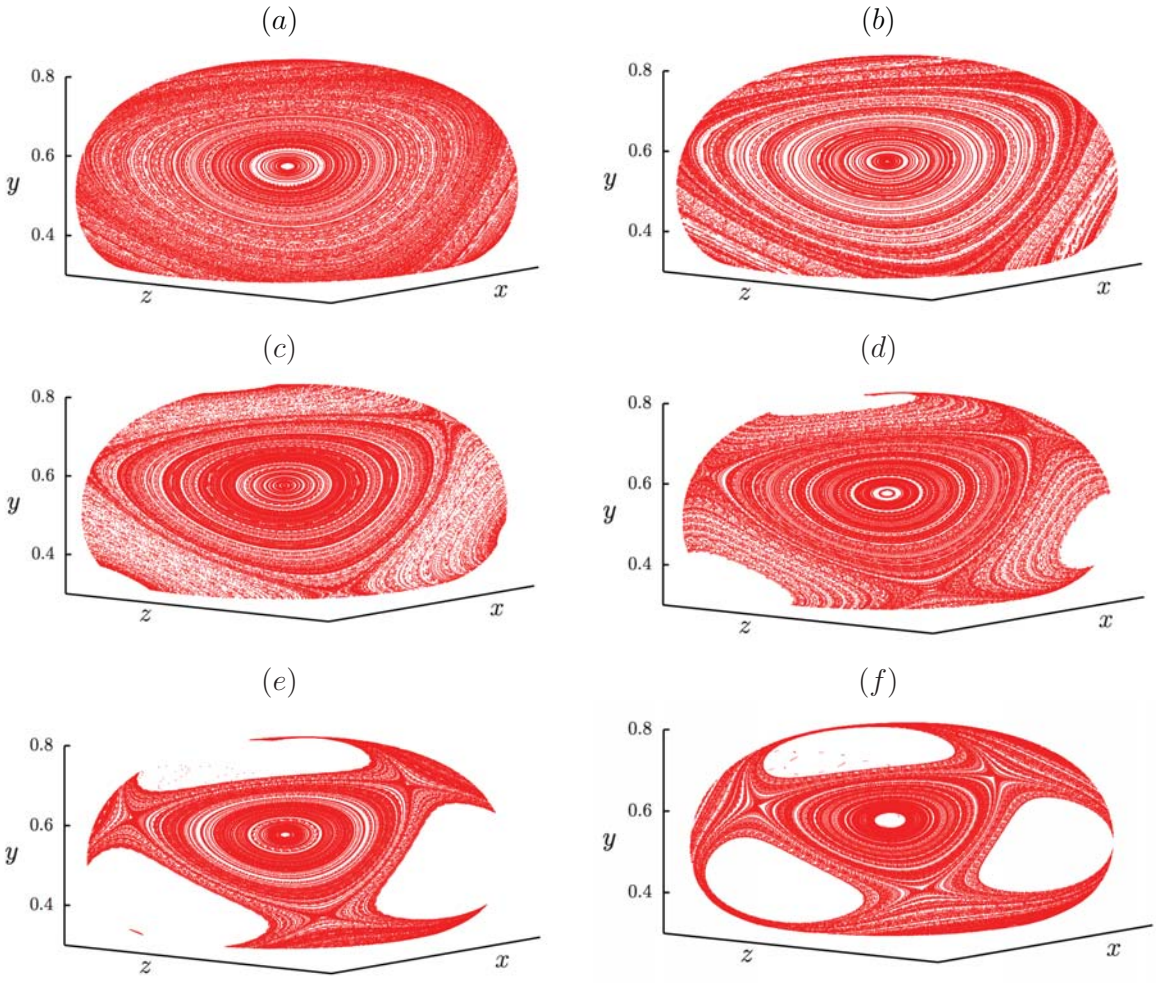

Figure 5.9: Ra $= 5 \times 10^4$. In (a)-(f) we are decreasing the radius of the invariant surfaces.

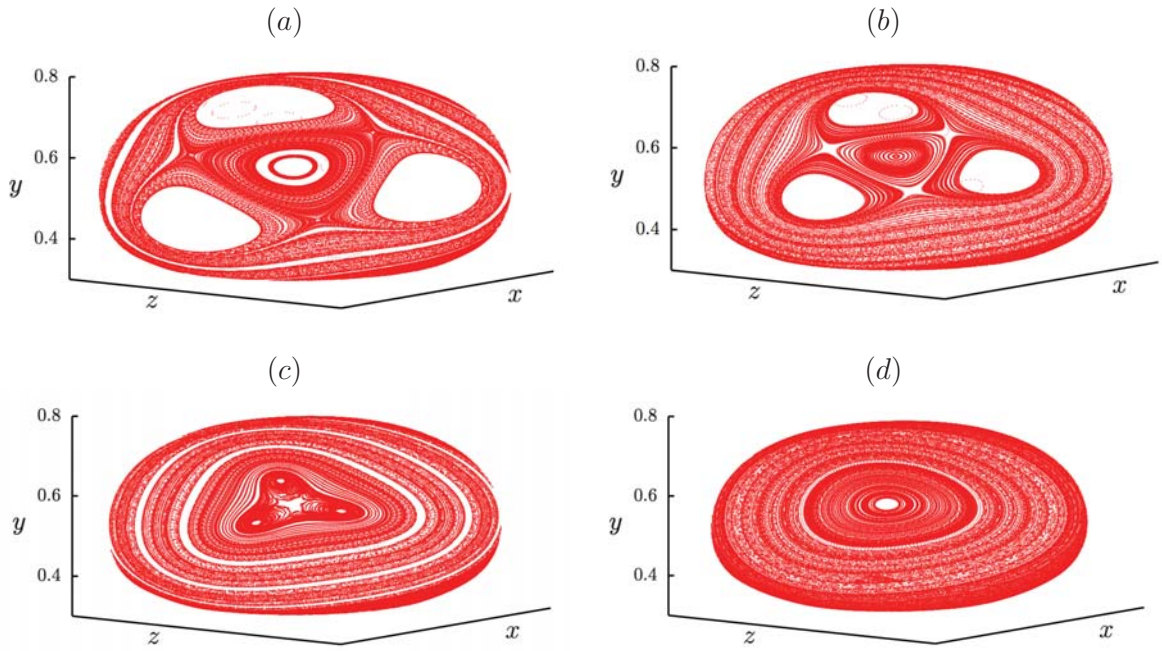

Figure 5.10: Continuation of previous sequence. Ra $= 5\times10^4$. In (a)-(d) we are decreasing the radius of the invariant surfaces.

It must be noticed that in the sequence of fig. 5.11 two of these pairs (hyperbolic/elliptic) correspond to one of the elliptic points and the other pair to the opposite elliptic point. What we are observing here is that the two opposite elliptic points 'merge' via the periodic orbits of the bifurcations. A similar behavior occurs in Poincaré maps for the partitioned pipe mixer when the mixing strength is augmented, see [10, 5].

A very similar behavior to figs. 5.10 $(c)-(d)$ is reported for the blinking rolls map [46]. In that case, investigators observe *stable* and *unstable* period-three orbits near a periodic point[4]. The collision of the fixed point and the unstable period three is named a *tripling* bifurcation point.

In fig. 5.12 we can see a phenomenon that occurs as Ra is increased. We observe four invariant surfaces with one of their elliptic points. From one value of the Ra to the other we see a wandering of points (a similar behavior is found increasing the displacement parameter for the lid-driven cylinder flow [6]). This effect is more dramatic for smaller radius of the invariant surfaces. Also we note that changing the radius for a given Ra results in the wandering of points and that the effect is more evident when we increase Ra.

[4]Two very interesting movies showing bifurcations for this system can be seen at the supplementary material web page.

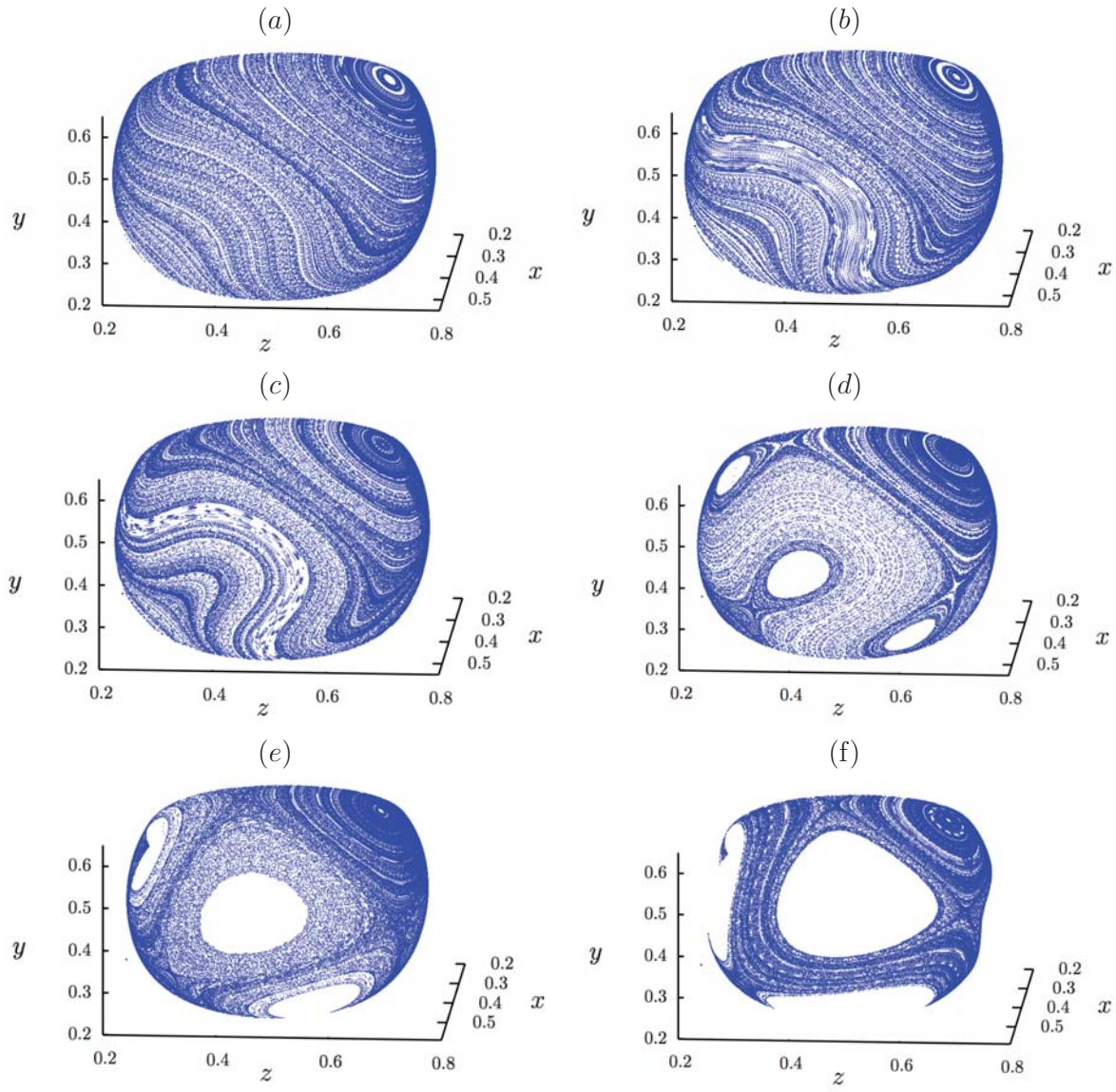

Figure 5.11: Ra $= 5 \times 10^4$. In (a)-(f) we are decreasing the radius of the invariant surfaces. We can see how points corresponding to the opposite elliptic points unite and separate.

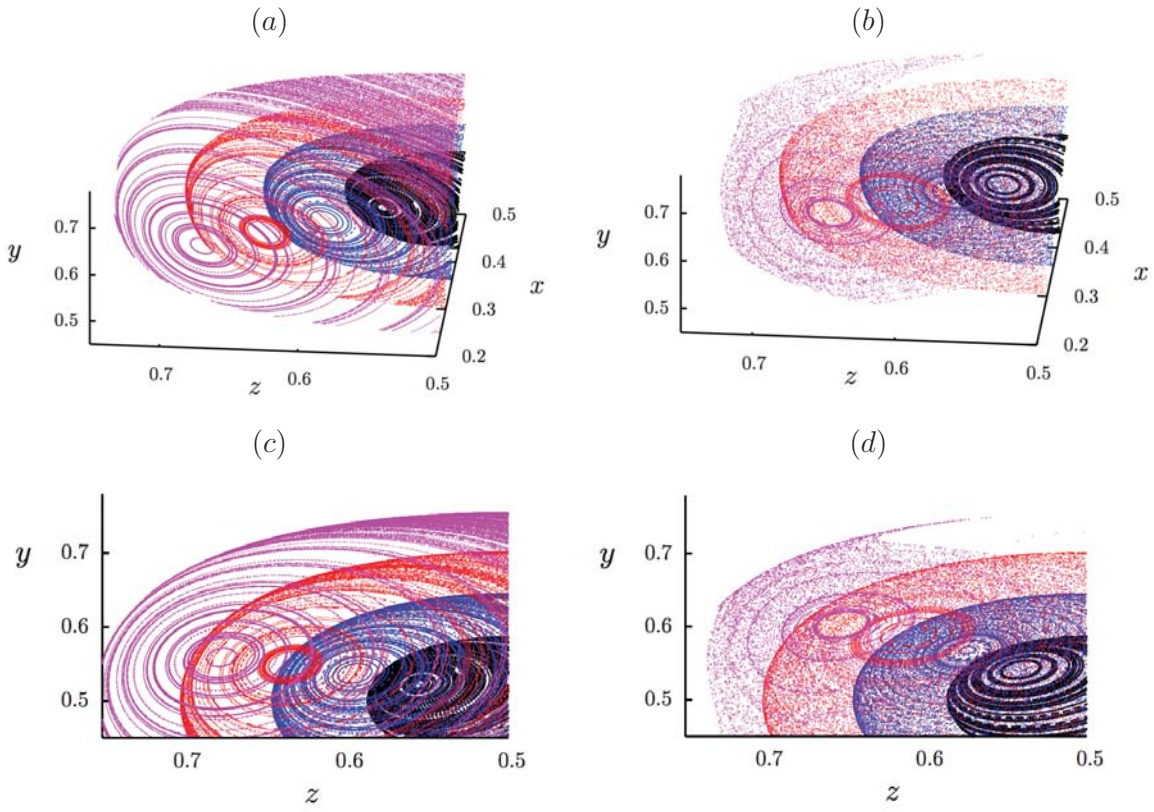

Figure 5.12: Position of elliptic points for different radii of invariant surfaces (this is expressed as different colors). (a) Ra $= 3 \times 10^4$, (b) Ra $= 5 \times 10^4$. $(c) - (d)$ are yz projection of $(a) - (b)$.

Rayleigh number 7×10^4

The dynamics for $\mathrm{Ra} = 5 \times 10^4$ and $\mathrm{Ra} = 7 \times 10^4$ are very similar. In fig 5.13 we show the tripling bifurcation previously described; the entire surfaces are shown for clarity. The difference between the dynamics of the two values of Rayleigh numbers is a difference of radii where they are present. Fig. 5.16 shows the tripling bifurcation for both Rayleigh numbers.

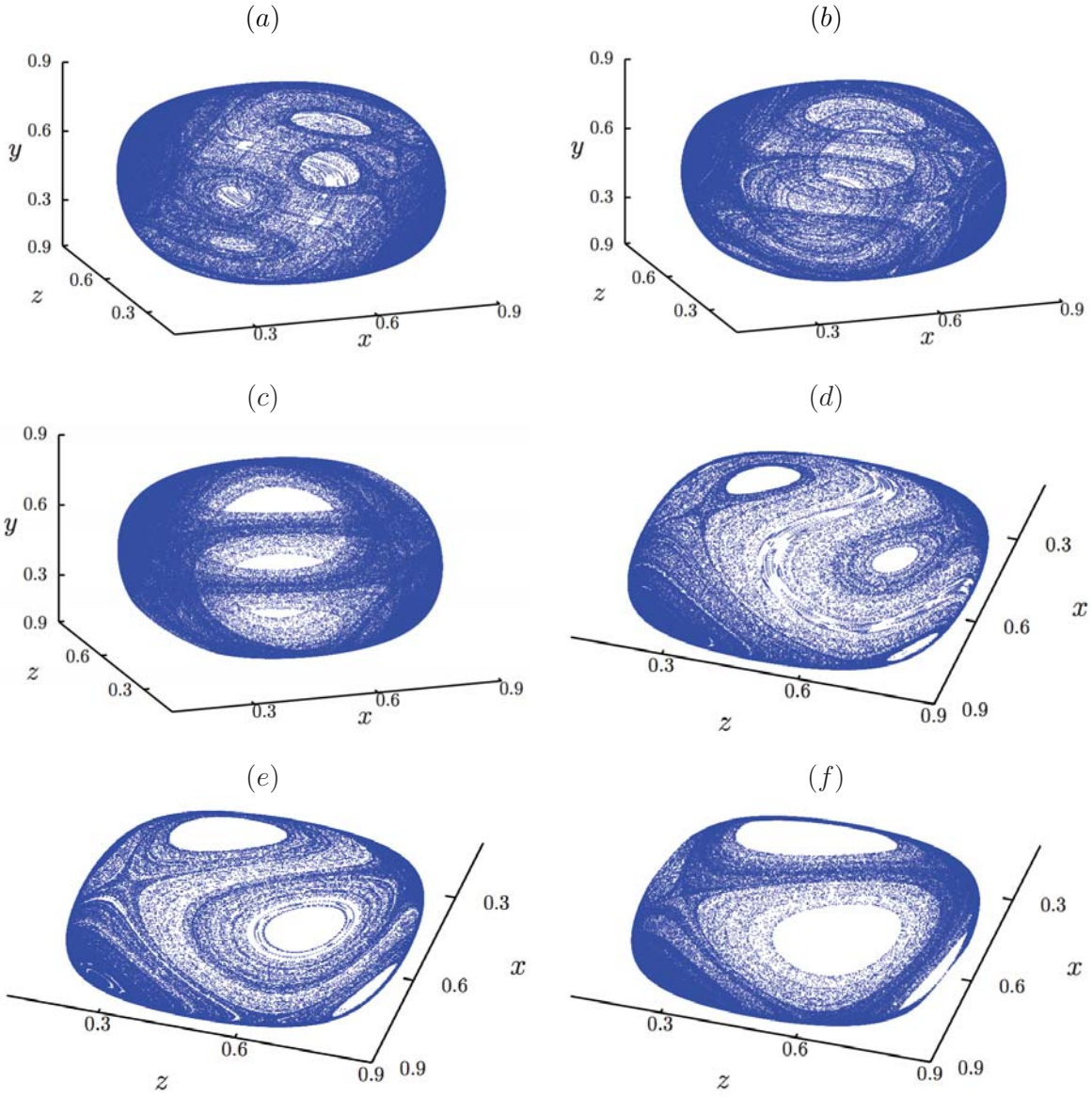

Figure 5.13: $\mathrm{Ra} = 7 \times 10^4$. In (a)-(c) we are decreasing the radius of the invariant surfaces, we can see how the two set of points unite. (d)-(f) top view with a cut in y of (a)-(c).

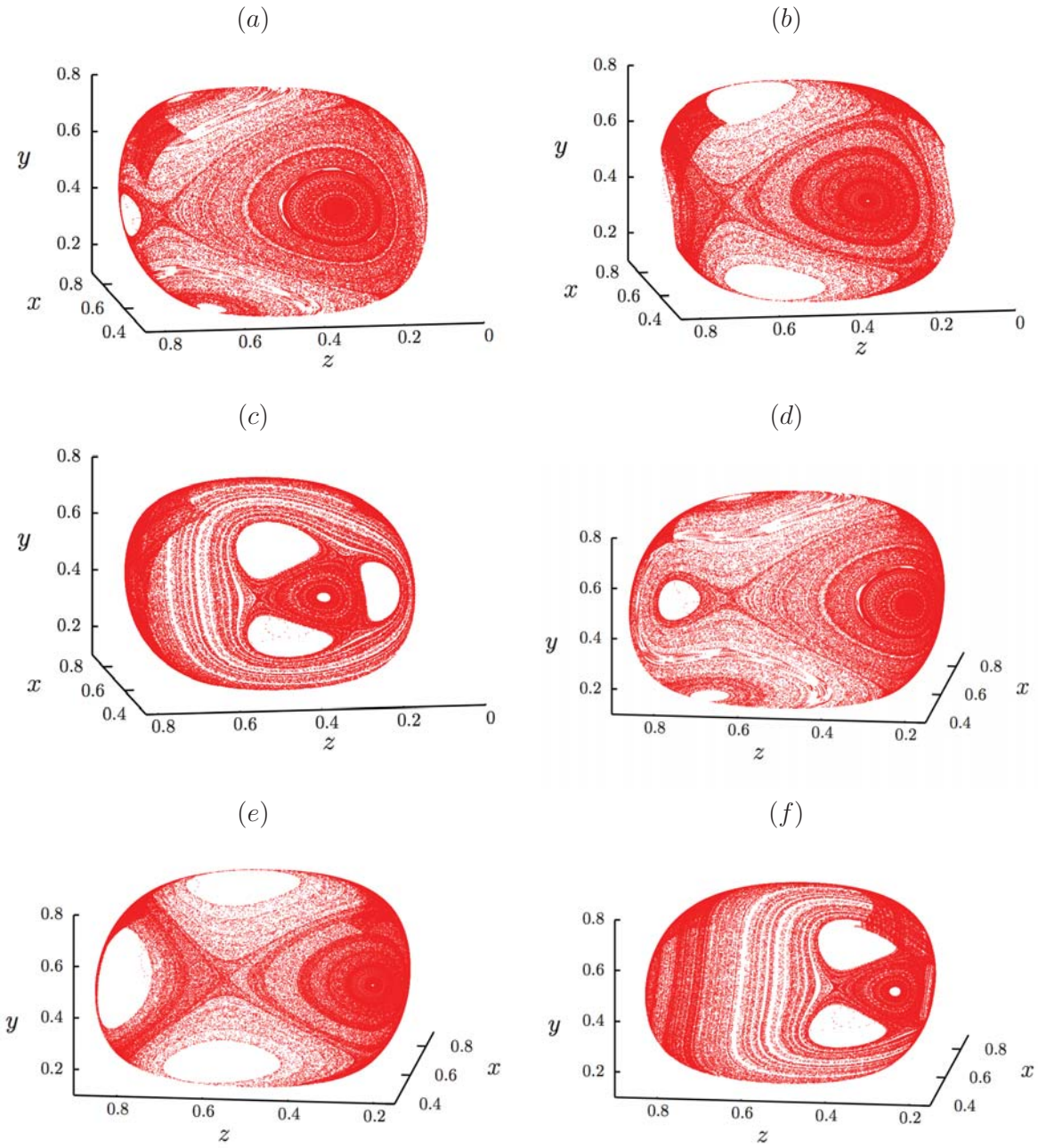

Figure 5.14: Ra $= 7\times10^4$. In (a)-(c) we are decreasing the radius of the invariant surfaces. $(d)-(f)$ Is a slightly different perspective of $(a)-(c)$.

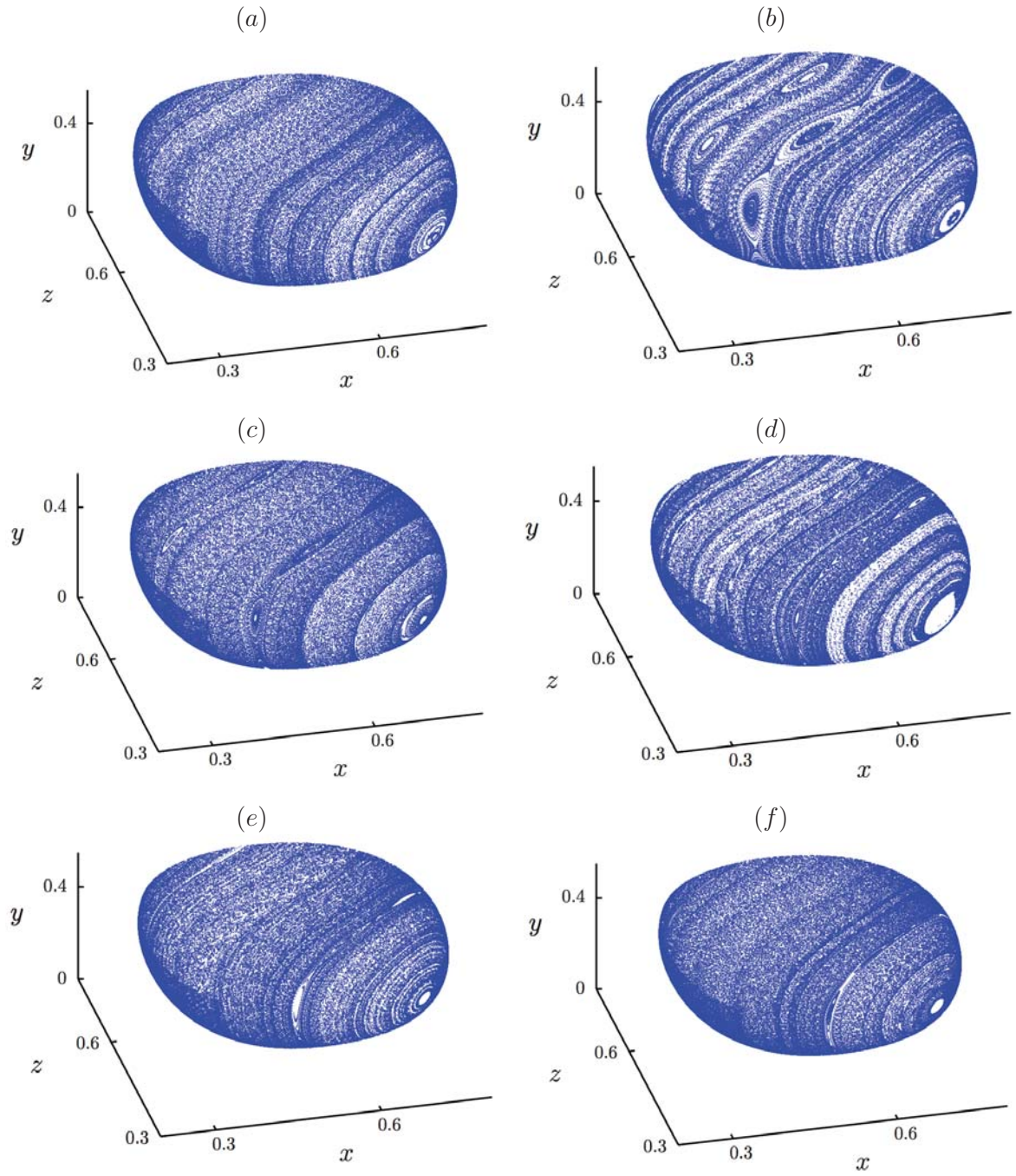

Figure 5.15: Ra $= 7 \times 10^4$. In (a)-(f) The Poincaré sections of orbits on invariant surfaces are shown for different radii. We can see for certain radii the appearance of island chains at the center of the invariant surfaces between the two elliptic points (only one is shown for clarity), see (b) and (d).

We want to highlight an interesting phenomenon that occurs after the merging of the set of points. In figs. 5.14 $(a)-(c)$ we show three invariant surfaces just before, during and after the merging of points. From (a) to (b) we changed the radius by a factor of two (i.e., we skipped one surface between them) and from (b) to (c) by a factor of five for clarity. A reconnection of hyperbolic points of the periodic 3 orbit is clearly seen by looking at the position of the elliptic points. Figs. 5.14 $(d)-(f)$ show a different view of the previous sequence.

A distinctive feature in this case is the appearance of chains of hyperbolic and elliptic points, see fig. 5.15. The difference of these chains with the described bifurcation in $\mathrm{Ra} = 3 \times 10^4$, is that we can not appreciate the points radius by radius until they 'collide' the main elliptic point, i.e., in the Poincaré sections the chains are lost at some radius and they are not clearly present onwards.

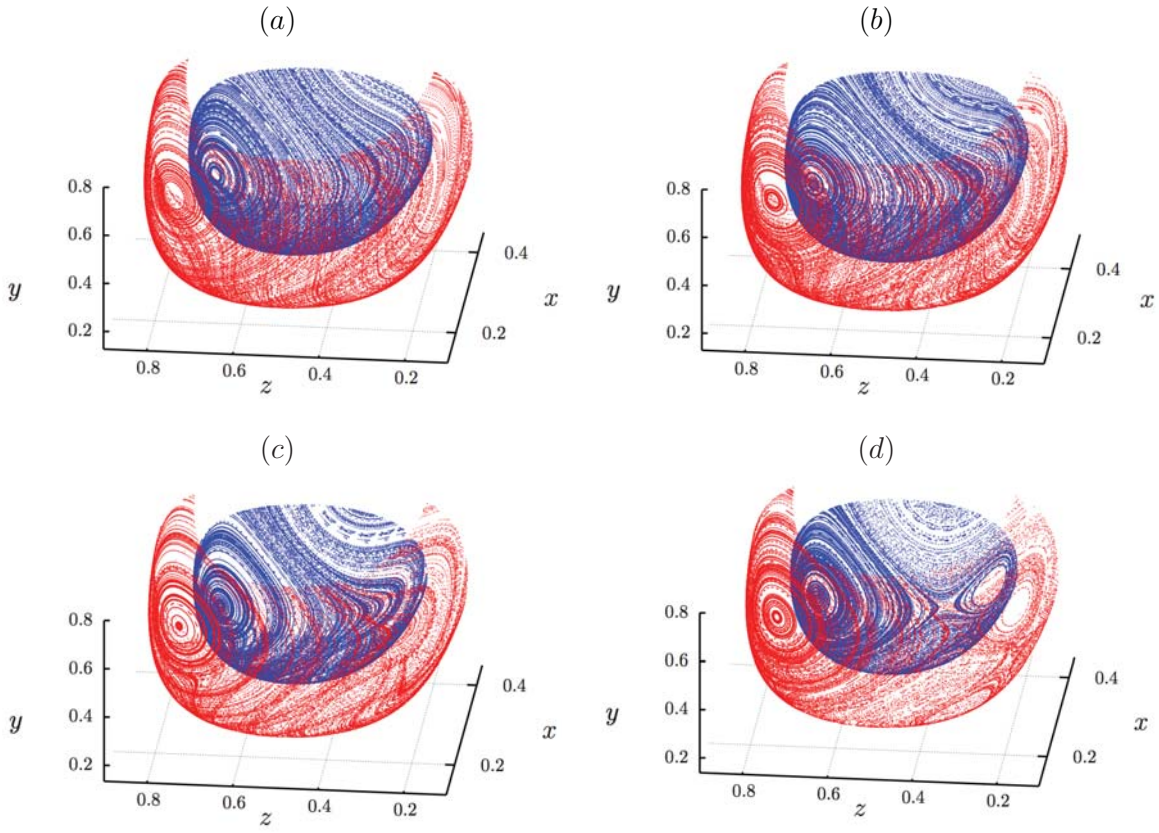

Figure 5.16: Comparison of invariant surfaces for $\mathrm{Ra} = 5 \times 10^4$ (blue) and $\mathrm{Ra} = 7 \times 10^4$ (red). In $(a)-(d)$ we are decreasing the radius. Topologies are similar but for 5×10^4 the different structures are exhibited at smaller radius compared with 7×10^4.

Rayleigh number 9×10^4

A change of the Poincaré section pattern occurs for $\mathrm{Ra} = 9 \times 10^4$ and $\mathrm{Ra} = 1 \times 10^5$. At the central region of surfaces we see the formation of four set of points, each consisting of a pair of hyperbolic and elliptic points, see figs. 5.17 $(a) - (d)$, this behavior is similar to a double-saddle-node bifurcation, a phenomenon also found for the blinking tumbler [25, 64, 65]. The four sets of points expand until they collide and a fragmentation of the entire surface takes place.

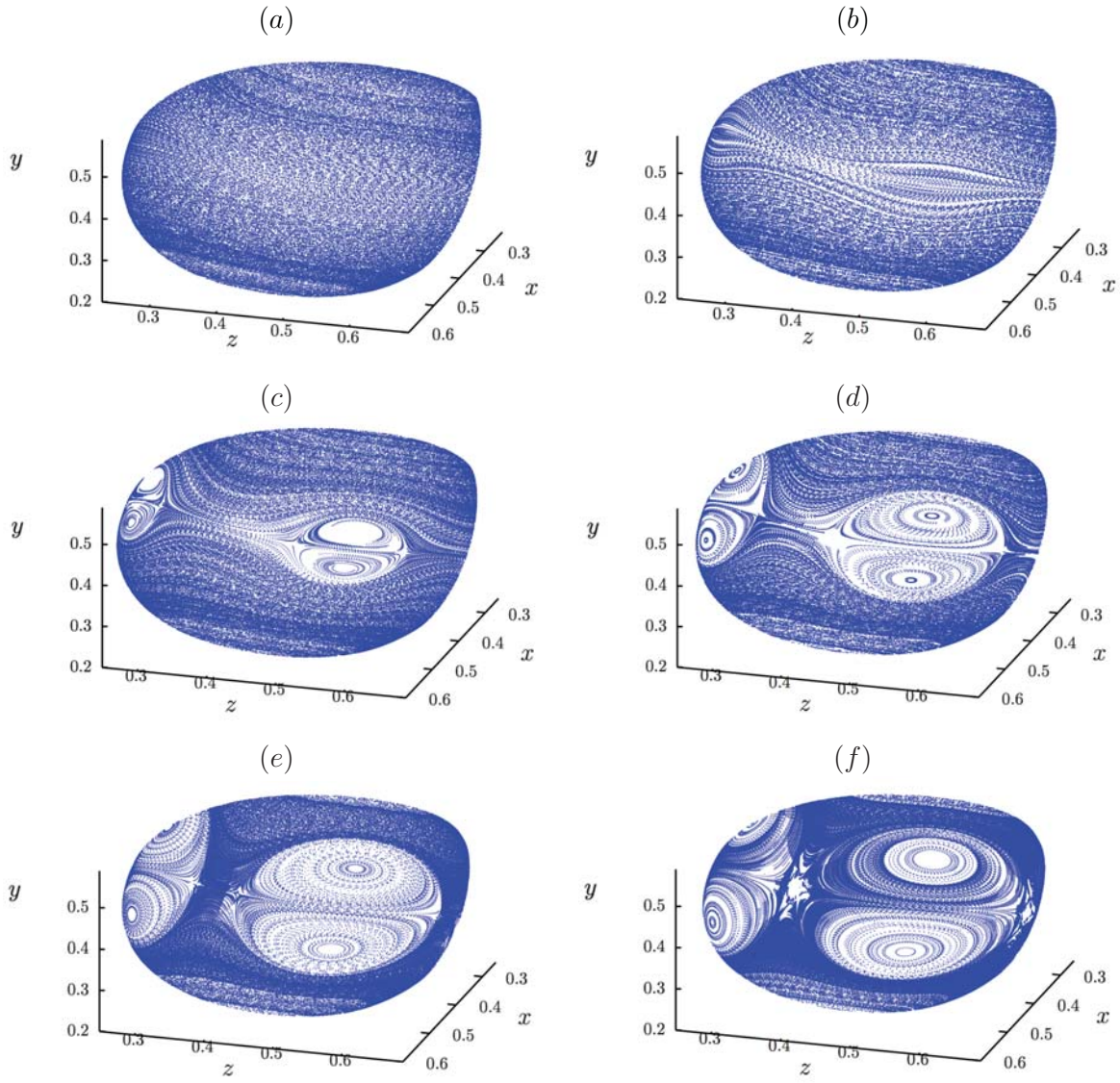

Figure 5.17: $\mathrm{Ra} = 9 \times 10^4$. In (a)-(f) we are decreasing the radius of the invariant surfaces.

By decreasing more the radius we see a separation of two set of points, each corresponding to the opposite elliptic points. This behavior resembles the bifurcation seen for level curves of Hamiltonians for the group $\mathbb{Z}_4$. The change of behavior of figs. 5.18 and 5.19 (b) to (c) looks like the two cases of level curves of 4-bifurcation points, see Appendix A.1. A complete sequence of a similar behavior is presented for $\mathrm{Ra} = 1 \times 10^5$ in the next subsection.

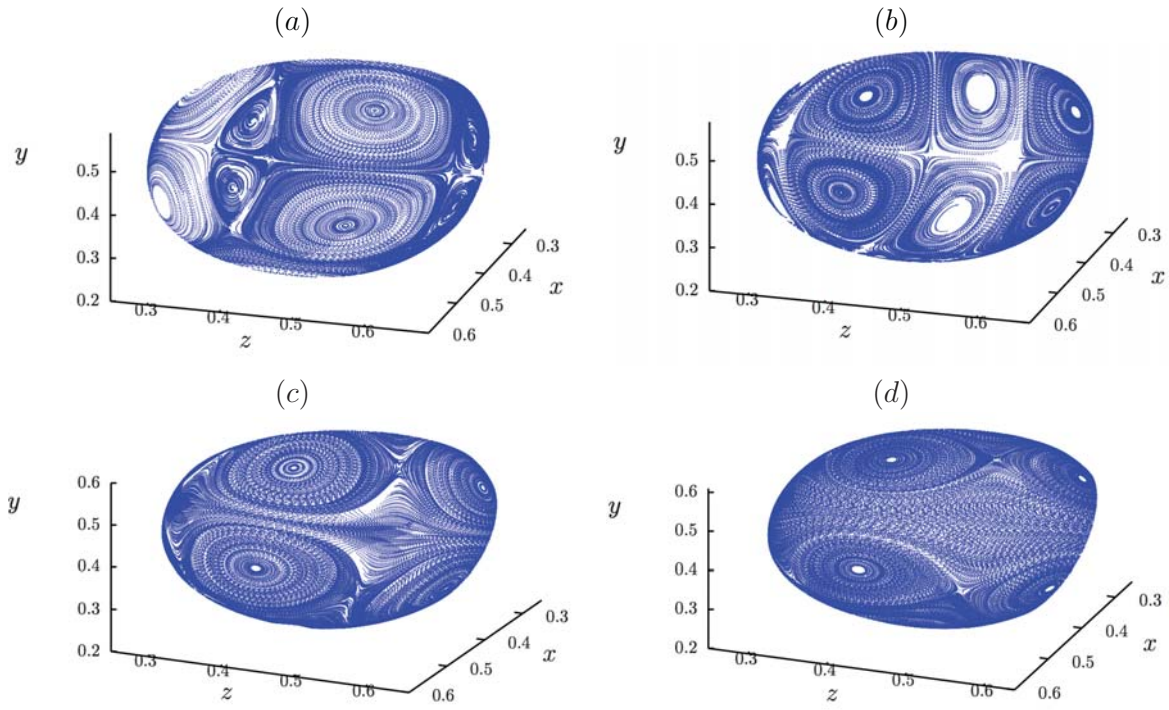

Figure 5.18: Continuation of previous sequence. $\mathrm{Ra} = 9 \times 10^4$. In ($a$)-($d$) we are decreasing the radius of the invariant surfaces. From (a) to (b) we have skipped one invariant surface because it shows a similar behavior.

In fig. 5.20 we observe the motion of elliptic points for $\mathrm{Ra} = 5 \times 10^4, 7 \times 10^4, 9 \times 10^4$ and different radii. The wandering of points is now more pronounced for the smaller surfaces. This behavior follows the behavior already described from 3×10^4 onwards. Fig. 5.21 shows the position of elliptic points about the plane $x = 1 - z$ (vertical line from this view point).

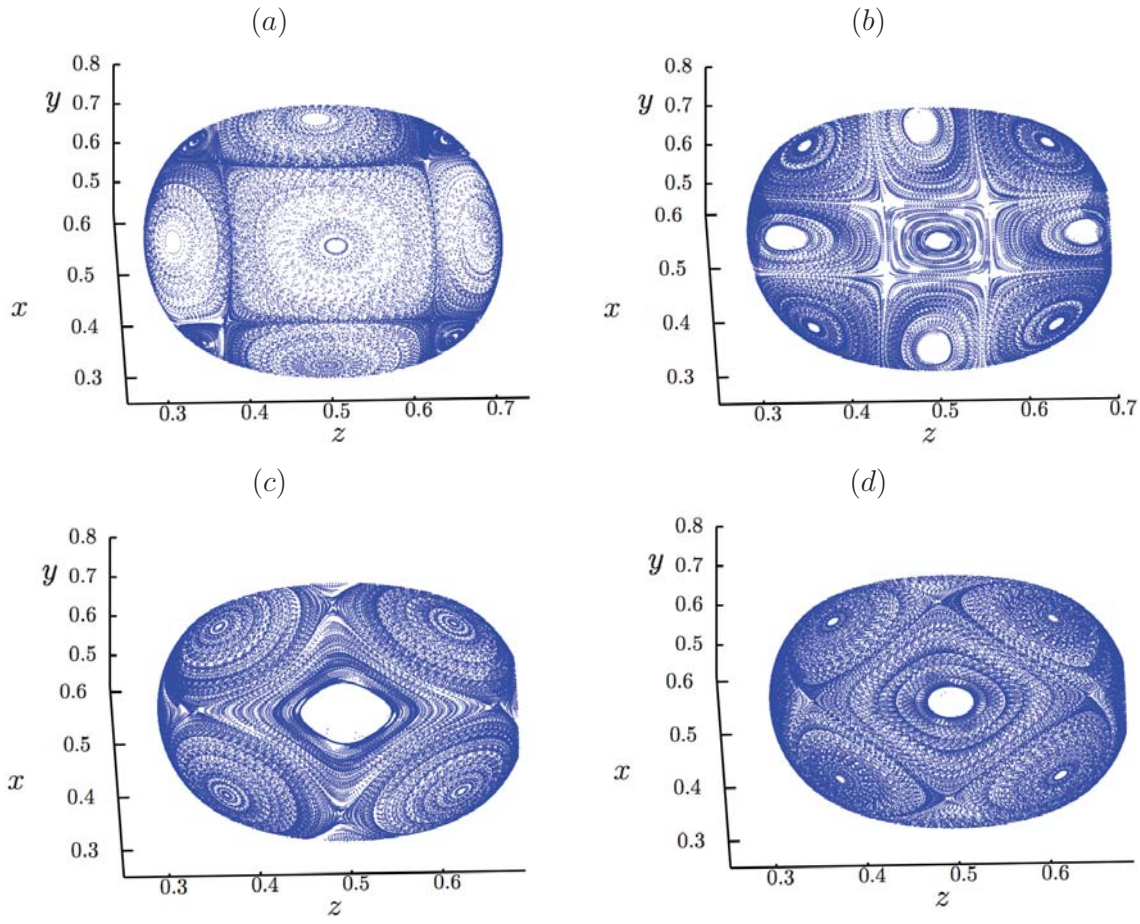

Figure 5.19: Another view of the previous sequence. Ra $= 9 \times 10^4$. In (a)-(d) the radius of the invariant surfaces decreases. From (a) to (b) we have skipped one invariant surface because it shows a similar behavior.

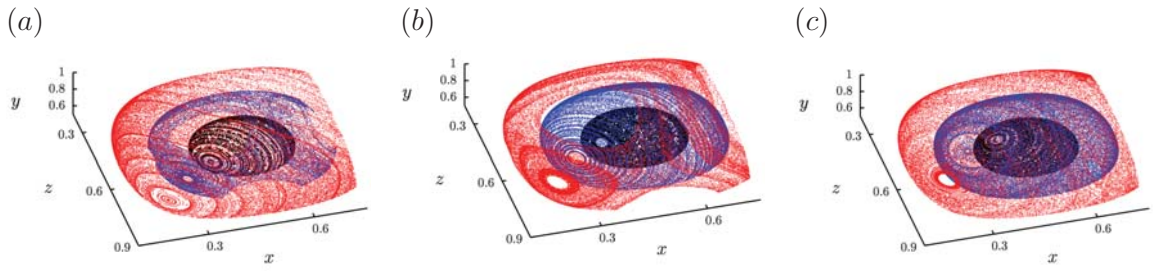

Figure 5.20: Position of elliptic points for different radii of invariant surfaces. (a) Ra $= 5 \times 10^4$, (b) Ra $= 7 \times 10^4$ and (c) Ra $= 9 \times 10^4$.

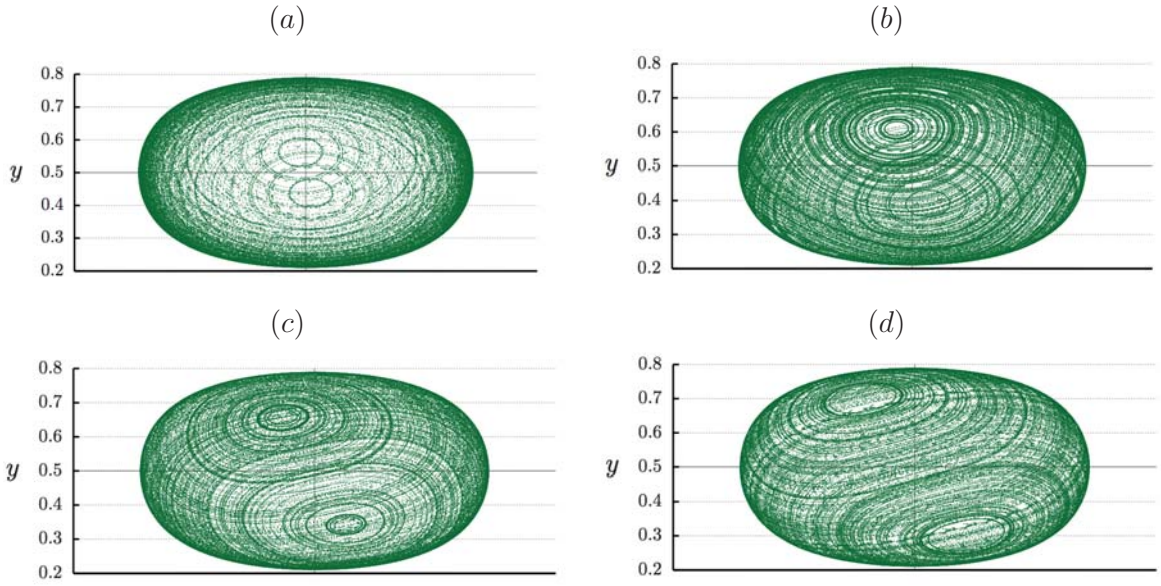

Figure 5.21: Wandering of elliptic points augmenting Ra for fixed radius, from this perspective the plane $x = 1 - z$ is represented by the vertical line. (a) Ra $= 3 \times 10^4$, (b) Ra $= 5 \times 10^4$, (c) Ra $= 7 \times 10^4$, and (d) Ra $= 9 \times 10^4$.

Rayleigh number 1×10^5

In essence we can group the dynamics of Ra $= 1 \times 10^5$ and Ra $= 9 \times 10^4$ as we did for Ra $= 7 \times 10^4$ and Ra $= 5 \times 10^4$. In figs. 5.22-5.23 we show the complete sequence of the 4-bifurcation. It is important to remark the way that hyperbolic points connect at different radii in a similar way as in the 3-bifurcation case. When the two set of points separate a reconnection occurs, see figs. 5.23 $(d) - (e)$.

Fig. 5.24 shows two nested invariant surfaces when the collision of hyperbolic points occurs (figs. 5.22 $(c) - (e)$). Fig. 5.25 shows the elliptic points wandering in this case; we make a comparison between Ra $= 5 \times 10^4$ and Ra $= 1 \times 10^5$ and we can see how the effect is more pronounced for larger Ra.

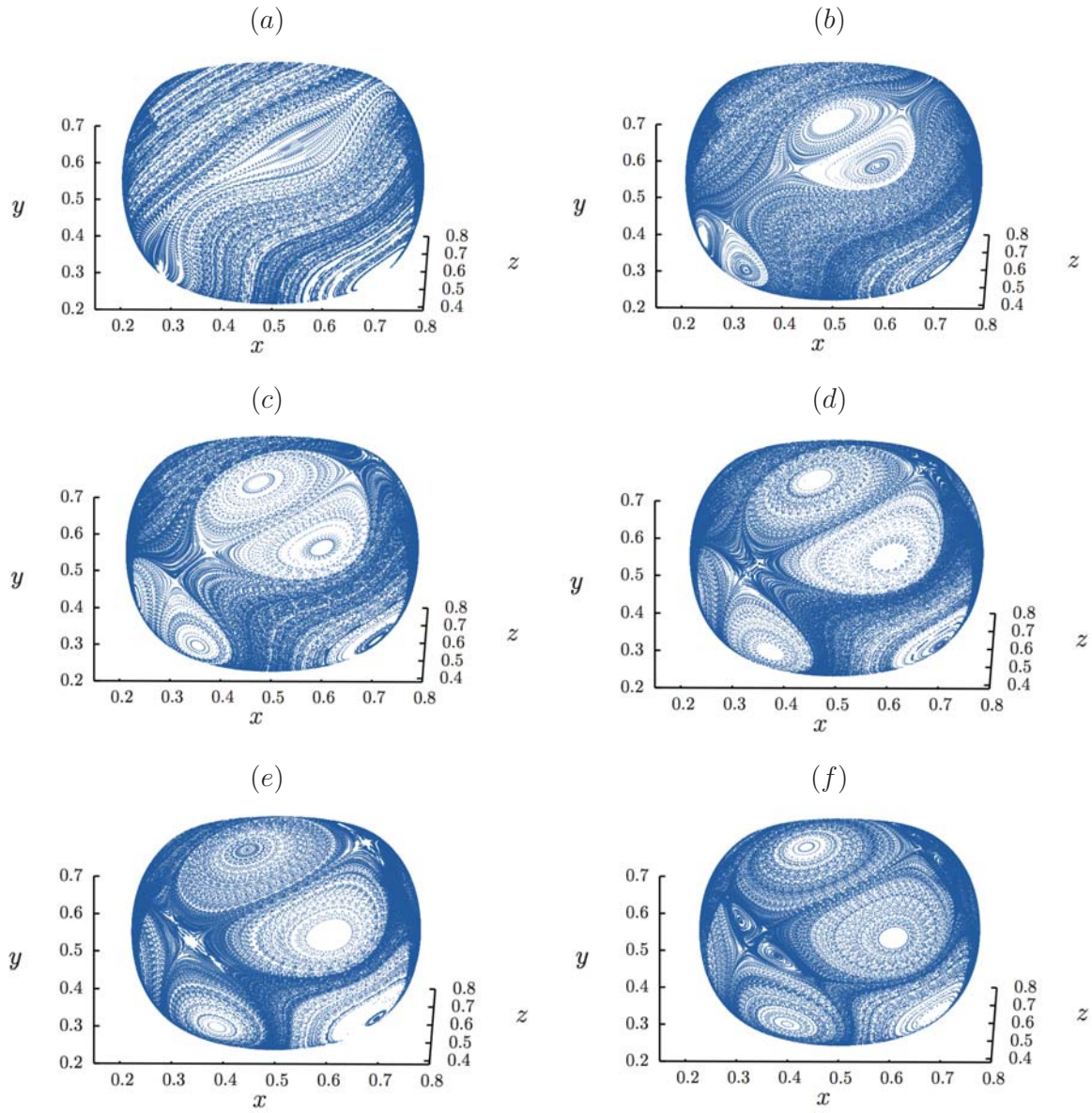

Figure 5.22: Ra $= 1 \times 10^5$. We focus in one of the elliptic points (right bottom). In (a)-(f) we are decreasing the radius of the invariant surfaces.

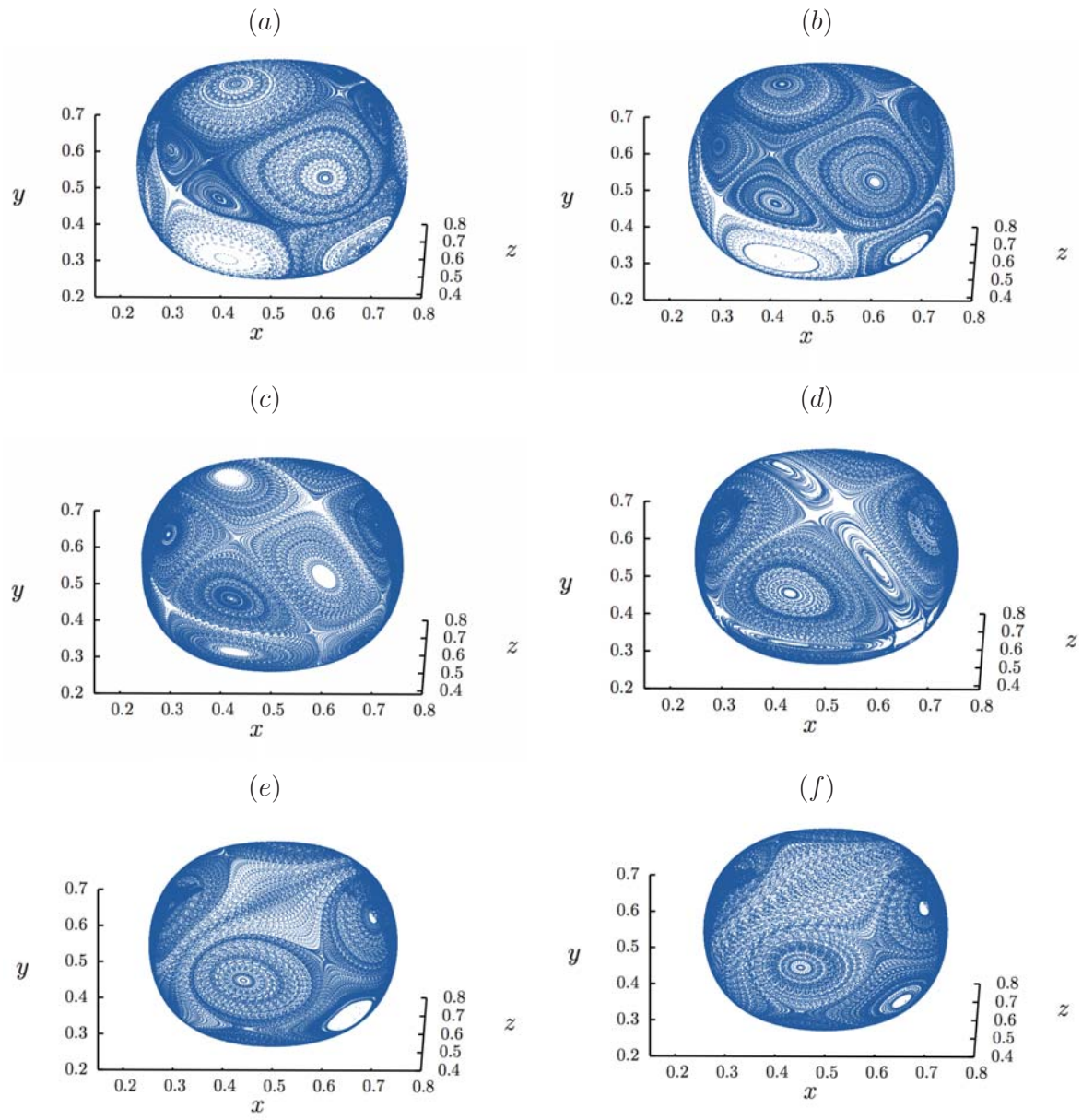

Figure 5.23: Continuation of previous sequence. Ra $= 1\times10^5$. In (a)-(f) we are decreasing the radius of the invariant surfaces.

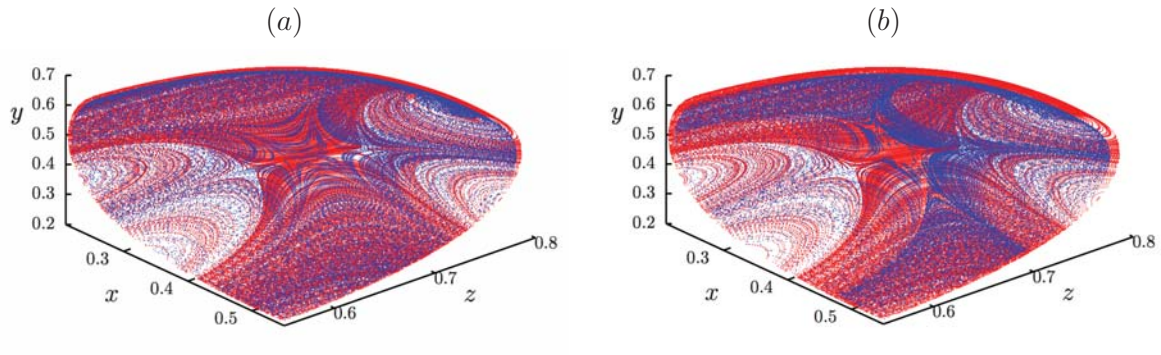

Figure 5.24: Ra $= 1 \times 10^5$. (a) Invariant surfaces of fig. 5.22 (c) and (d). (b) Invariant surfaces of fig. 5.22 (c) and (e).

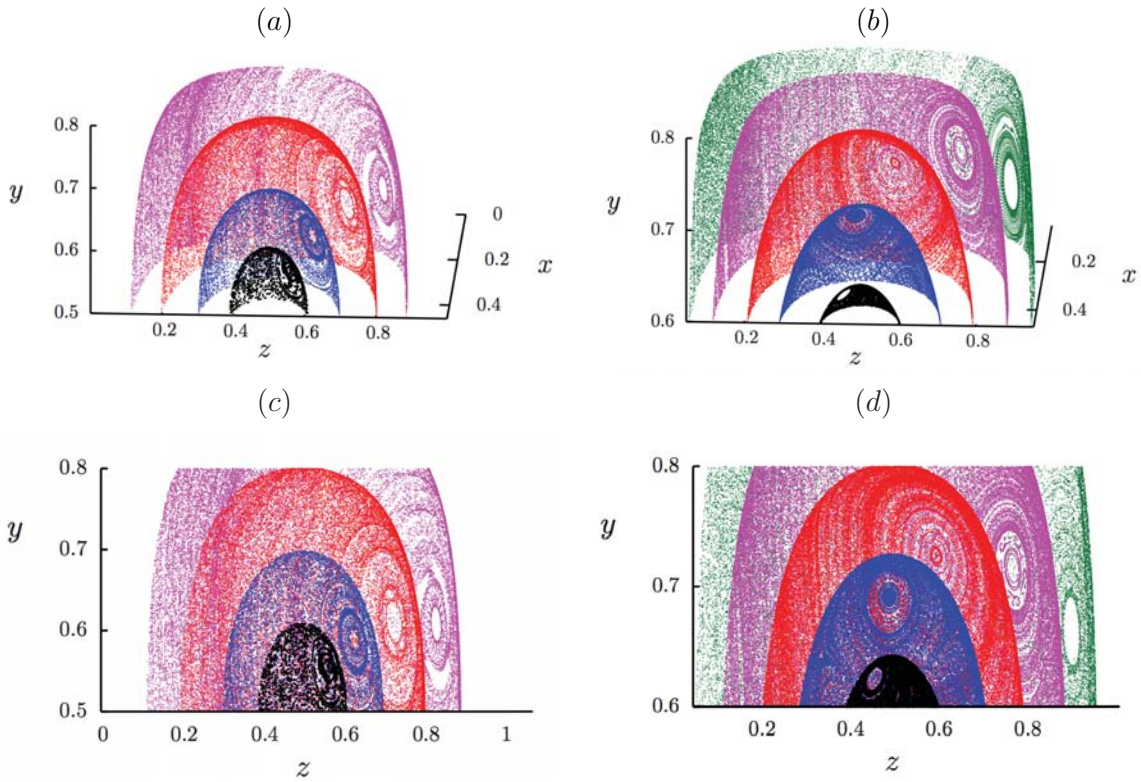

Figure 5.25: (a) Position of elliptic points for different radii of invariant surfaces for Ra $= 5 \times 10^4$. (c) View of (a) in the zy plane. (b) Same as (a) for Ra $= 1 \times 10^5$. (d) View of (b) in the zy plane.

Rayleigh number 5×10^5

From $\mathrm{Ra} = 1 \times 10^5$ to 5×10^5 we see a big change in the dynamics and consequently in the pattern of the Poincaré section. A clear difference is the absence of the two elliptic points present for all the radii at opposite sides of the surfaces. At a specific radius, we find isolated critical points but they are present only for few surfaces, i.e., in a limited range of radii. We find now different behaviors as filled surfaces with no apparent structures. This behavior is called 'fully chaotic intra-surface dynamics' for the lid-driven cylinder flow [6], recall also the description of the standard map with increasing strength in section 2.2.1. It can also be observed 4 critical points symmetrically located with respect to planes $x = z$ and $x = 1 - z$, and two points symmetrically positioned about $x = z$ or $x = 1 - z$ planes. The different structures observed are positioned in pairs symmetrically arranged as we have observed in the previous cases.

For surfaces near the center of the cube we recover the presence of two elliptic points at opposite places on the invariant surface. For this value of the Rayleigh number we will show sequences of invariant surfaces where representative behaviors are displayed. The figures are presented in order of decreasing radii. In Fig. 5.26 we see a five-tupling bifurcation. In this case, the phenomenon is present just for a small number of surfaces, in contrast with the case $\mathrm{Ra} = 3 \times 10^4$.

In fig. 5.27 we see a similar behavior to a 3-bifurcation for two elliptic points. Fig. 5.28 is the continued sequence for the left point of fig. 5.27. The situation represented in this sequence display a similar behavior as the tripling bifurcations for the blinking rolls map [46]. Similar behavior is also found in some bifurcations for the volume preserving maps studied in [66]. In fig. 5.29 we show a sequence where we can observe a great variety of isolated points.

We also find a period doubling bifurcation as the one reported for the blinking rolls map [46]. This is a similar phenomenon to the 'figure eight' bifurcation[5] found for Hamiltonians with $\mathbb{Z}_2$ symmetry, see figs. 5.30-5.32. In the first of the sequences at the left the 'figure eight' bifurcation can be identified, while on the right side we see a double-saddle-node bifurcation. Fig. 5.31 shows a frontal view of the period doubling bifurcation. In the sequence of fig. 5.32 we can see the evolution of the 'figure eight' point, in (b) we observe a connection between the points forming the period doubling bifurcation with points of the double-saddle-node bifurcation. Recall that the structures appear in pairs on the invariant surfaces, we are showing a cut of the surfaces for more clarity. After this connection we observe another 'figure eight' point but located with a rotation with respect to the first one. This behavior after merging of points is similar to reconnections after 3 and 4-bifurcations.

[5] See Appendix A.1.

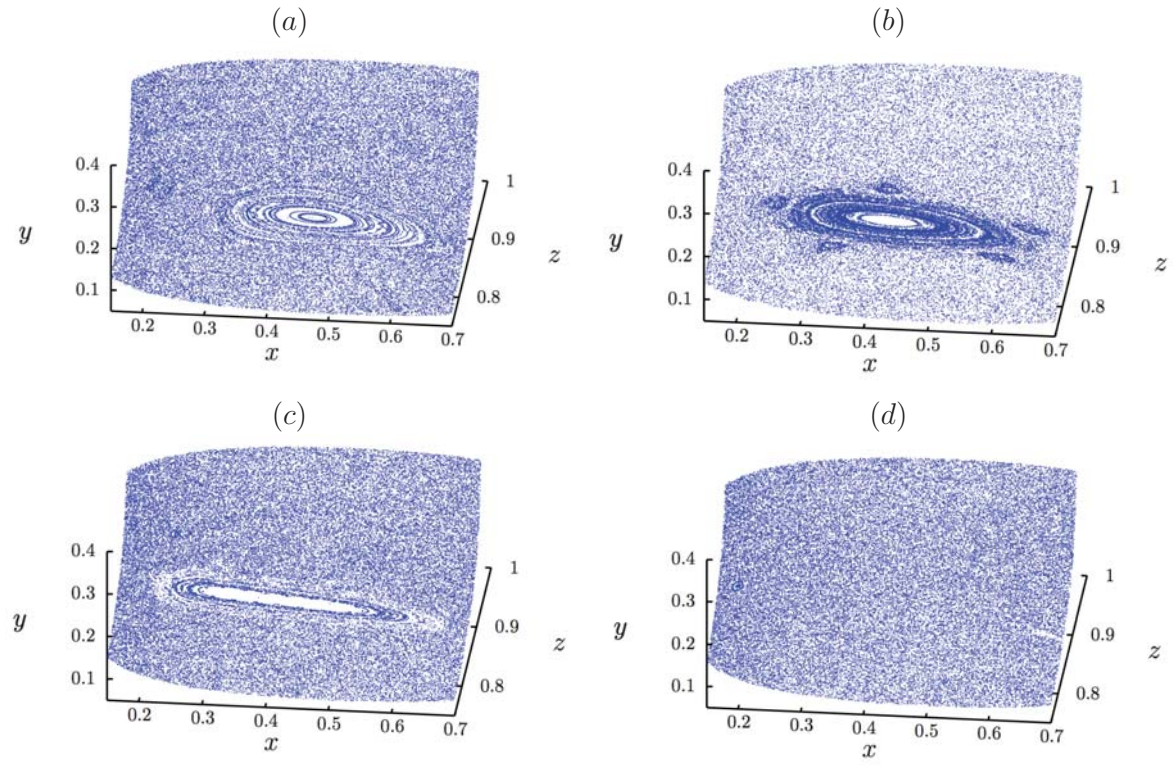

Figure 5.26: Ra $= 5\times10^5$. In (a)-(d) we are decreasing the radius of the invariant surfaces.

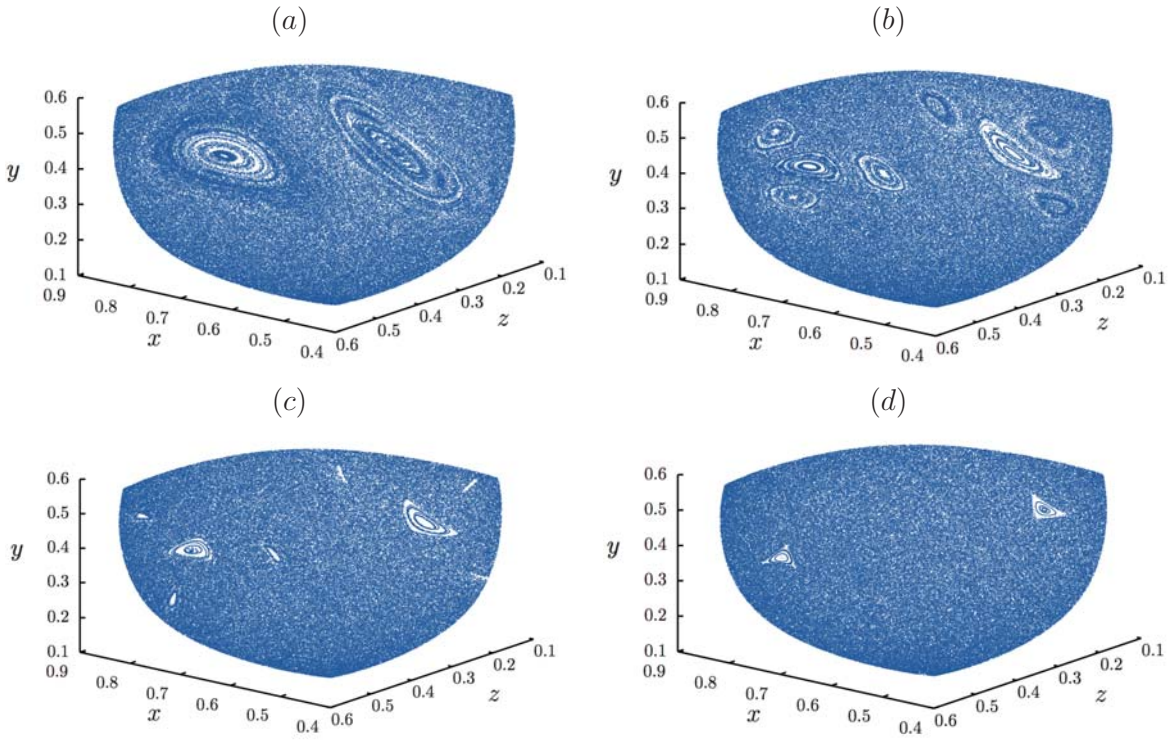

Figure 5.27: Ra $= 5\times10^5$. In (a)-(d) we are decreasing the radius of the invariant surfaces.

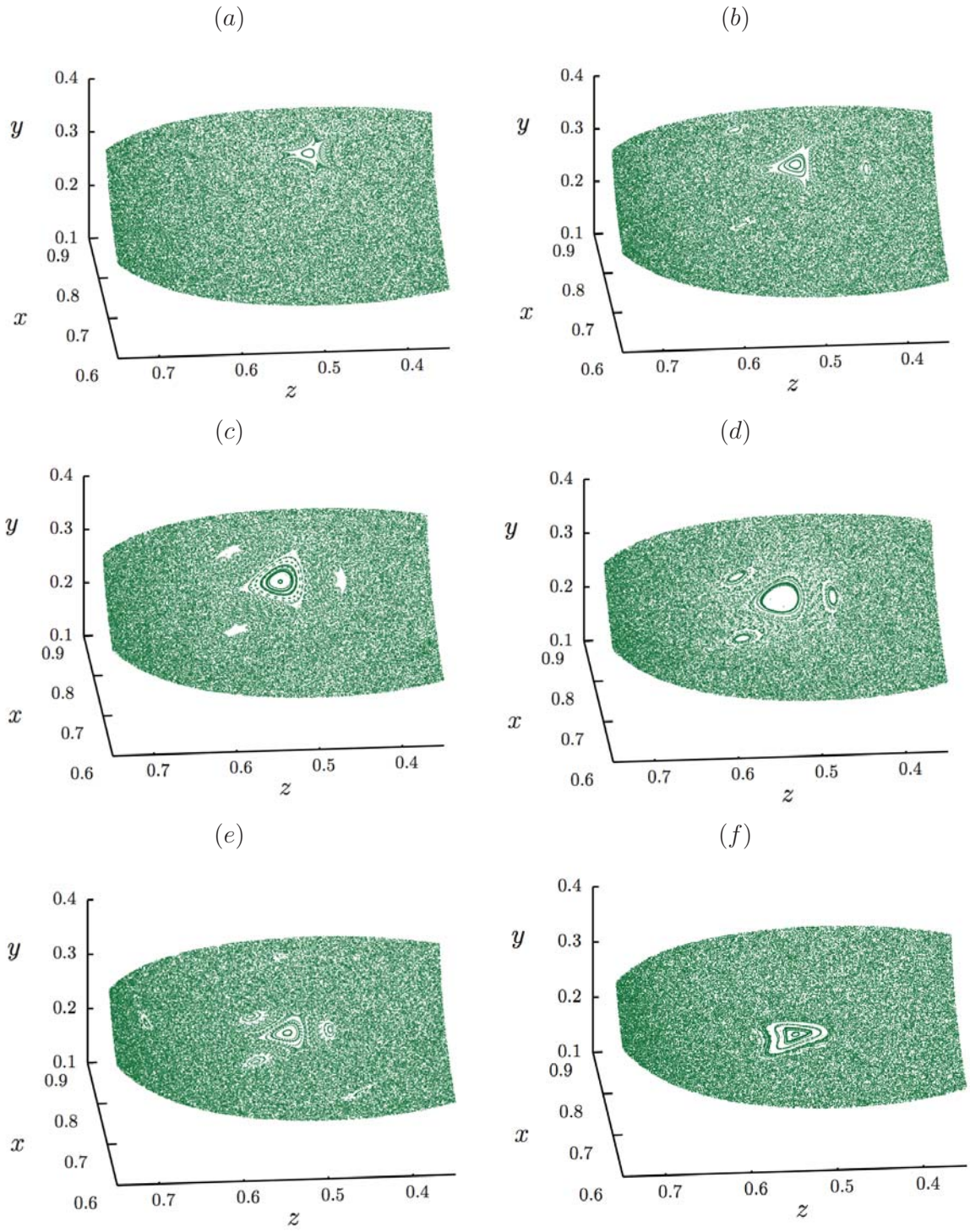

Figure 5.28: Continuation of the previous sequence for the point on the left. $\mathrm{Ra} = 5 \times 10^5$. In (a)-(f) we are decreasing the radius of the invariant surfaces.

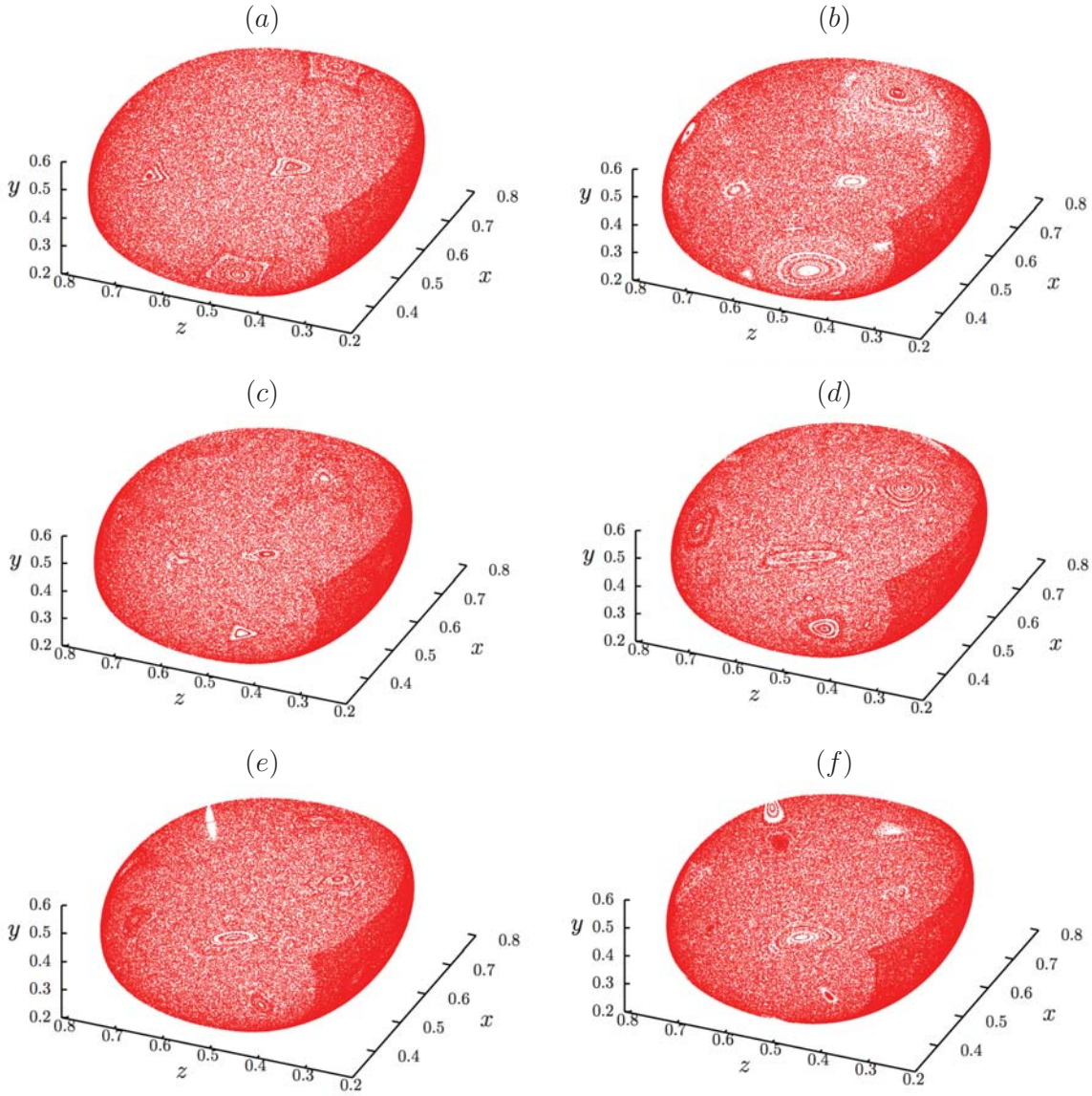

Figure 5.29: Ra $= 5 \times 10^5$. In (a)-(f) we are decreasing the radius of the invariant surfaces.

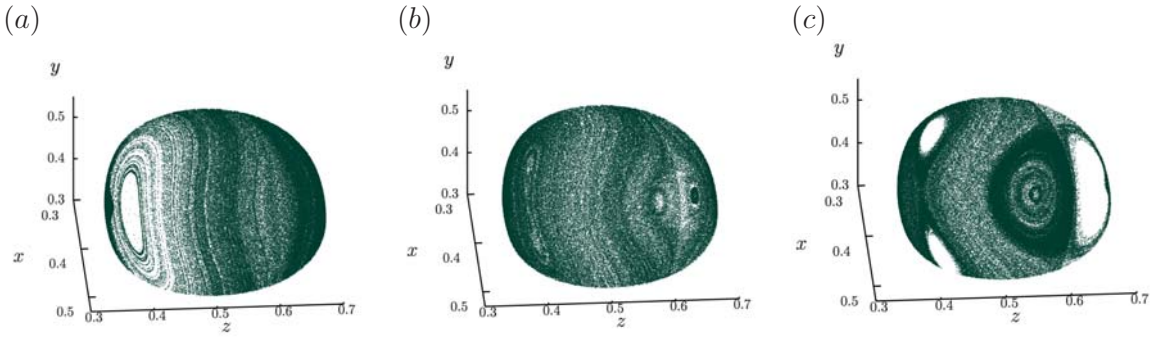

Figure 5.30: Ra $= 5 \times 10^5$. In $(a) - (c)$ we are decreasing the radius of the invariant surface.

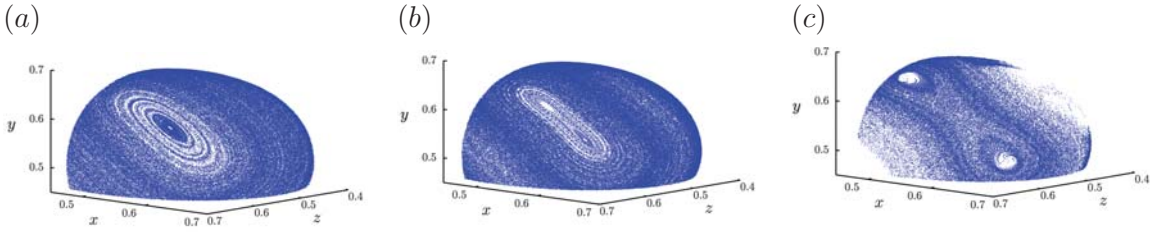

Figure 5.31: Ra $= 5 \times 10^5$. In $(a) - (c)$ we are decreasing the radius of the invariant surface.

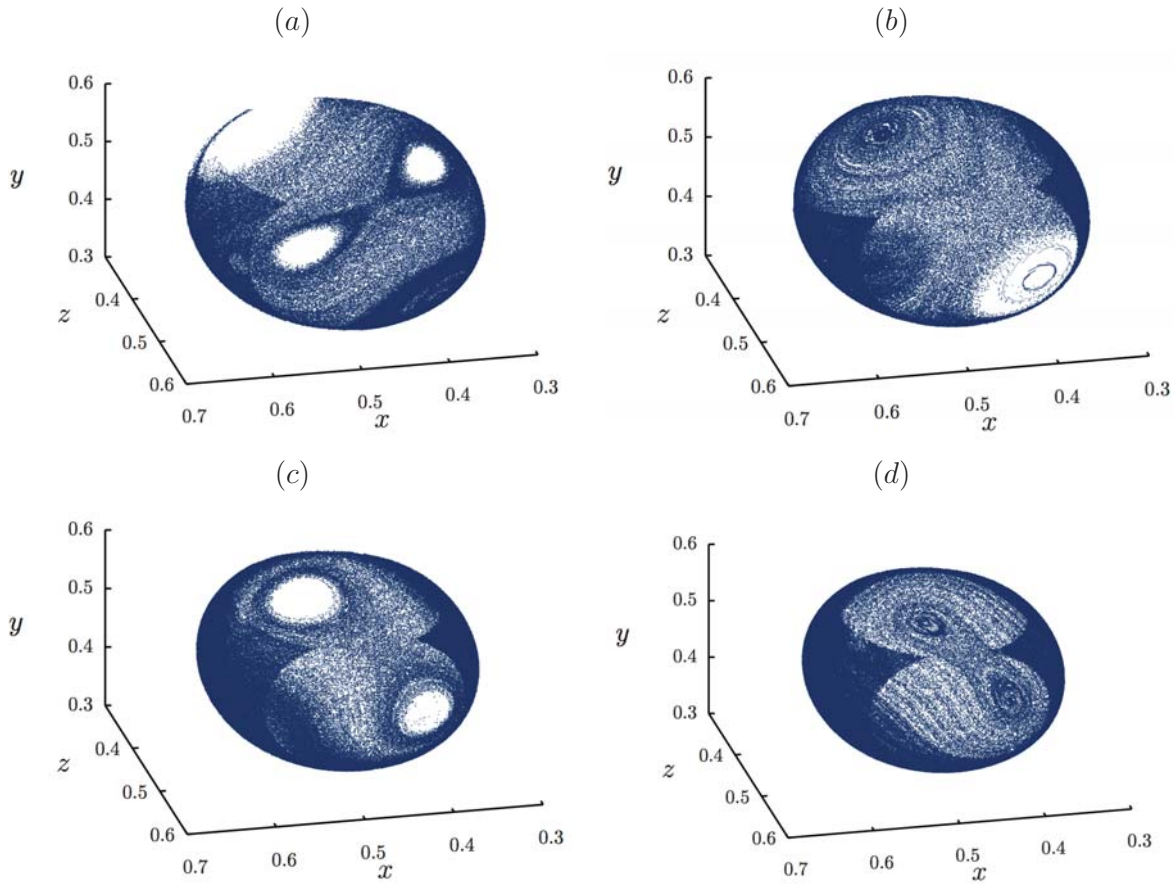

Figure 5.32: Ra $= 5\times10^5$. In (a)-(d) we are decreasing the radius of the invariant surfaces.

Table 5.1 summarizes q-tupling bifurcations found for different Rayleigh numbers and radii. Each column is obtain for a fixed Rayleigh number, Poincaré sections and the variations with the radius is examined downwards. As described in the previous sections, we can group together cases Ra $= 5\times10^4$ and 7×10^4, and cases Ra $= 9\times10^4$ and 1×10^5. In this table we took intervals of radii in order to group the bifurcations observed. We can see how the different structures are observed at different intervals of radii, smaller radii for smaller Ra. The case Ra $= 5\times10^5$ displays different Poincaré section patterns from all others but near to the center of the cube we recover the presence of two elliptic points symmetrically positioned as is found for the other cases examined. Purple and black figures show chains of elliptic and hyperbolic points, eight and seven, respectively and are the cases where we can not track the patterns radius by radius as in the other figures. The behavior of these chains is similar to the resonant bifurcations studied in [67] for the elastic pendulum.

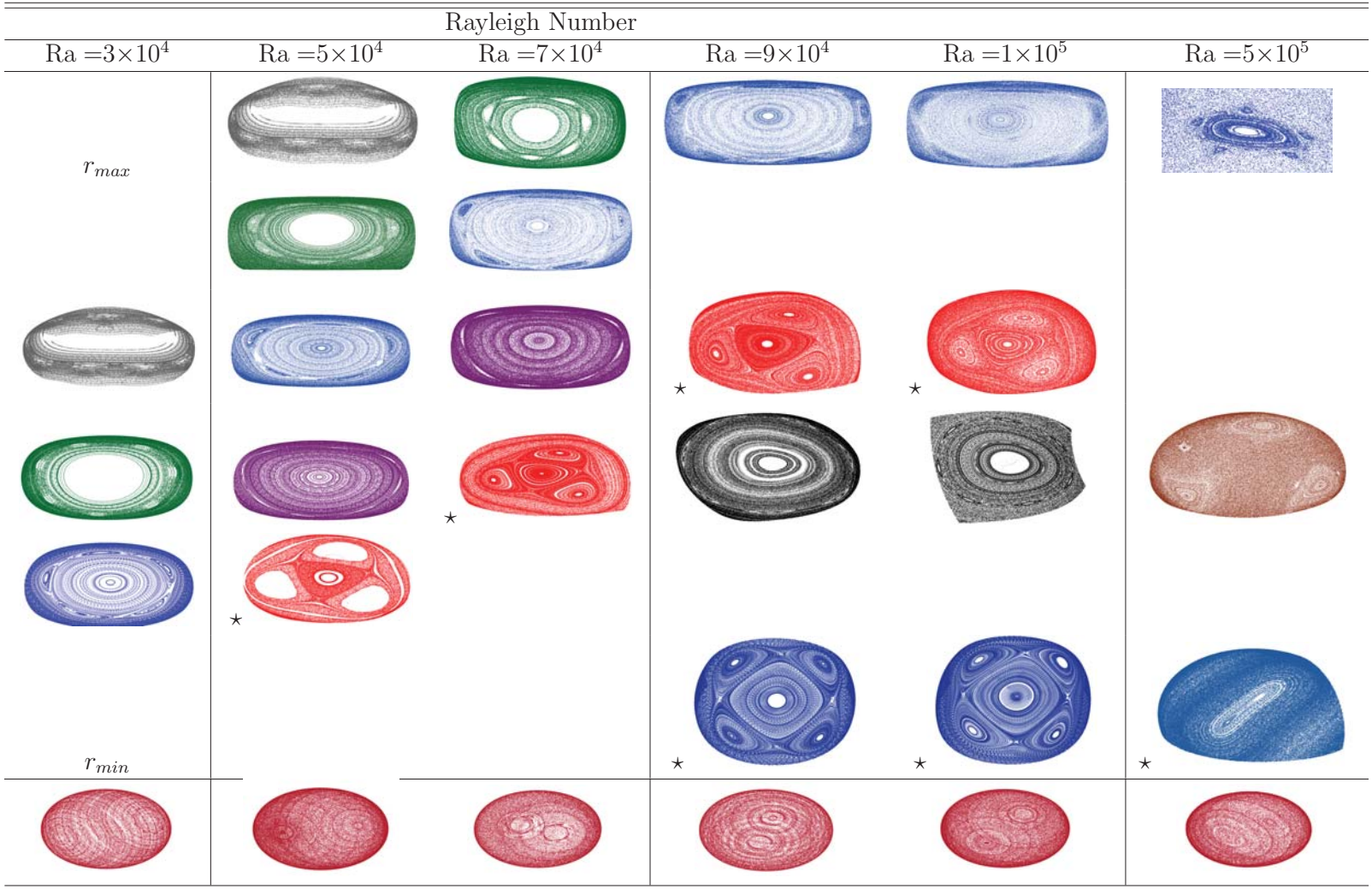

Table 5.1: Main topologies on invariant surfaces. ⋆ Merging of points observed.

5.1.3 Period-1 lines

We have found period-1 lines for all the values of Rayleigh number on the symmetry plane $x = 1 - z$. The shape becomes progressively convoluted with growing Rayleigh number, see figs. 5.33 - 5.35. A similar behavior is found for the lid-driven cylinder flow [18, 6, 40], their displacement parameter is equivalent to Rayleigh number in our system.

In fig. 5.33, the colors represent $\mathrm{Ra} = 1 \times 10^5$, black, $\mathrm{Ra} = 9 \times 10^4$, purple, $\mathrm{Ra} = 7 \times 10^4$, blue, $\mathrm{Ra} = 5 \times 10^4$, red, and $\mathrm{Ra} = 3 \times 10^4$, orange. We use different types of points for more clarity and plot the symmetry plane with a green grid. In fig. 5.34 the colors represent $\mathrm{Ra} = 1 \times 10^5$, black, and $\mathrm{Ra} = 5 \times 10^5$, red; here we plot the symmetry plane with a blue grid. In both figures the dots represent the intersection of an invariant surface and the plane. In fig. 5.35 we show a xy projection of the previously commented figures.

We can group these lines according to the intersections with the lines $y = 0.5$ (horizontal) and the vertical line that passes through the center of the cube. In this way, cases for 3×10^4 and 5×10^5 have no partners but we can relate 5×10^4 with 7×10^4, and 9×10^4 with 1×10^5, this behavior is consistent with the analysis of the dynamics of intra-surface topologies of the previous section.

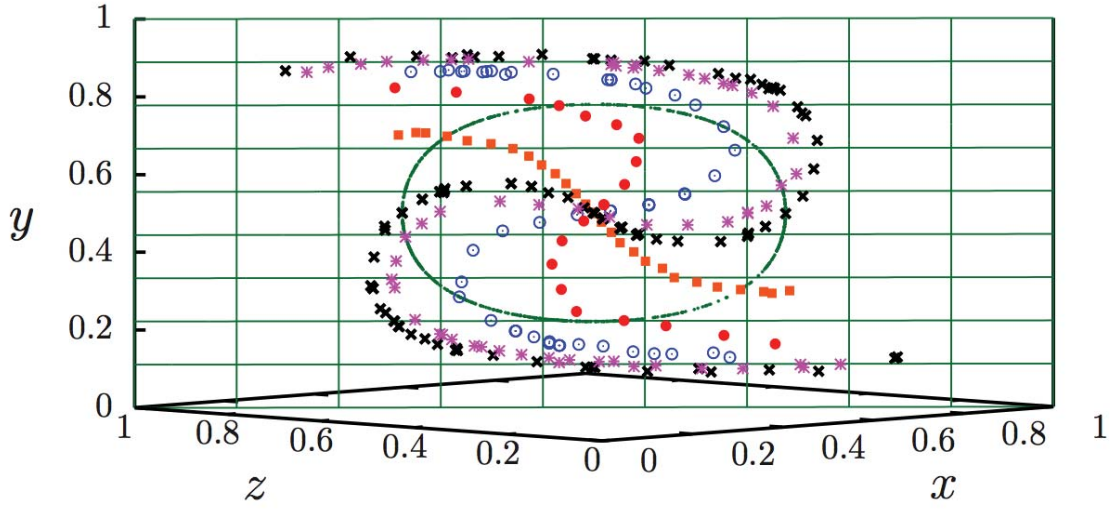

Figure 5.33: Periodic lines found on the plane $x = 1 - z$ (green) for different Ra. Black ($\mathrm{Ra} = 1 \times 10^5$), purple ($\mathrm{Ra} = 9 \times 10^4$), blue ($\mathrm{Ra} = 7 \times 10^4$), red ($\mathrm{Ra} = 5 \times 10^4$) and orange ($\mathrm{Ra} = 3 \times 10^4$). Green dots represent the intersection of an invariant surface and the plane.

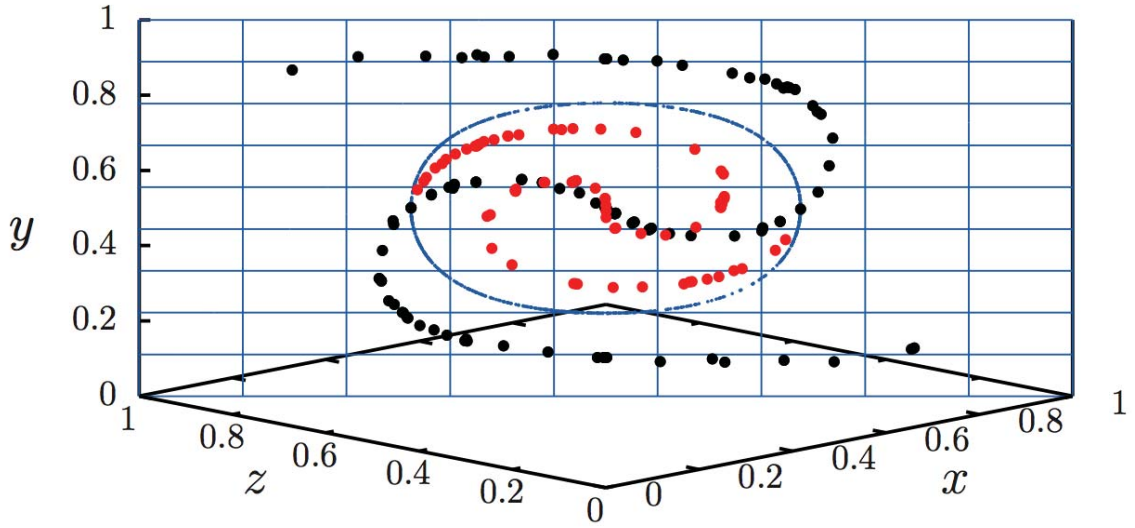

Figure 5.34: Periodic lines found on the plane $x = 1 - z$ (blue) for different Ra. (a) Black ($\mathrm{Ra} = 1 \times 10^5$) and red ($\mathrm{Ra} = 5 \times 10^5$). Blue dots represent the intersection of an invariant surface and the plane.

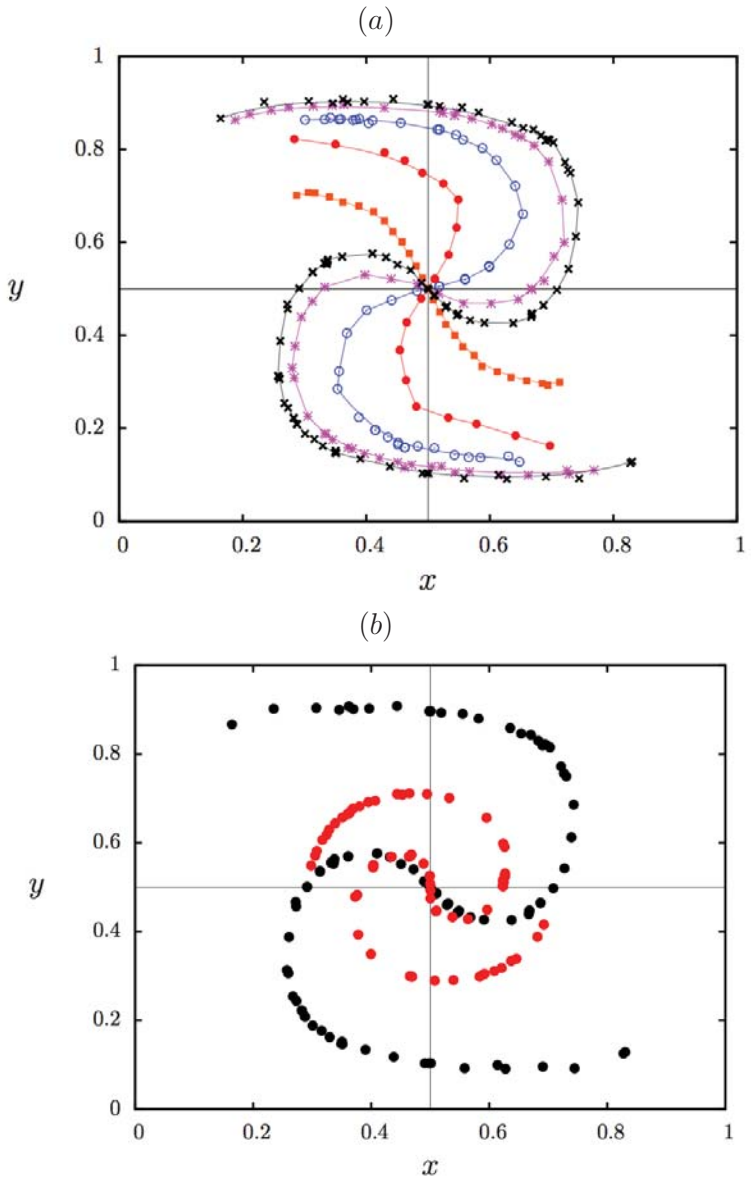

Figure 5.35: Projection of figures 5.33 and 5.34 on the xy plane, colors represent the same Ra numbers as in the previous figures. In (a) lines have been added to highlight the trends.

Closed periodic lines

For Ra $= 9 \times 10^4, 1 \times 10^5, 5 \times 10^5$ we find also closed periodic lines on the symmetry planes, $x = z$ and $x = 1 - z$, at the same interval of radii of invariant surfaces, i.e., the periodic lines are symmetrically situated. Closed periodic lines have been shown for different systems, in the 3D Stokes flows in a cubic container considered by Anderson et al. [20], periodic lines are closed or start and end on the boundary of the flow domain; this is also the case for the lid-driven cylinder flow [18].

The arrangement of closed periodic lines is similar to the periodic lines studied for the blinking tumbler [25, 65, 64]. In fig. 5.36 we plot periodic lines found for Ra $= 5 \times 10^5$, Ra $= 9 \times 10^4$. The case Ra $= 1 \times 10^5$ is topologically equivalent.

For Ra $= 9 \times 10^4, 1 \times 10^5$ we found two closed periodic lines (each one on each of the planes analyzed). In the case Ra $= 5 \times 10^5$ we found more closed lines symmetrically arranged after making a search refinement, see fig. 5.37 for the settlement of points on the $x = 1 - z$ plane. In fig. 5.38 we show periodic lines found on each plane.

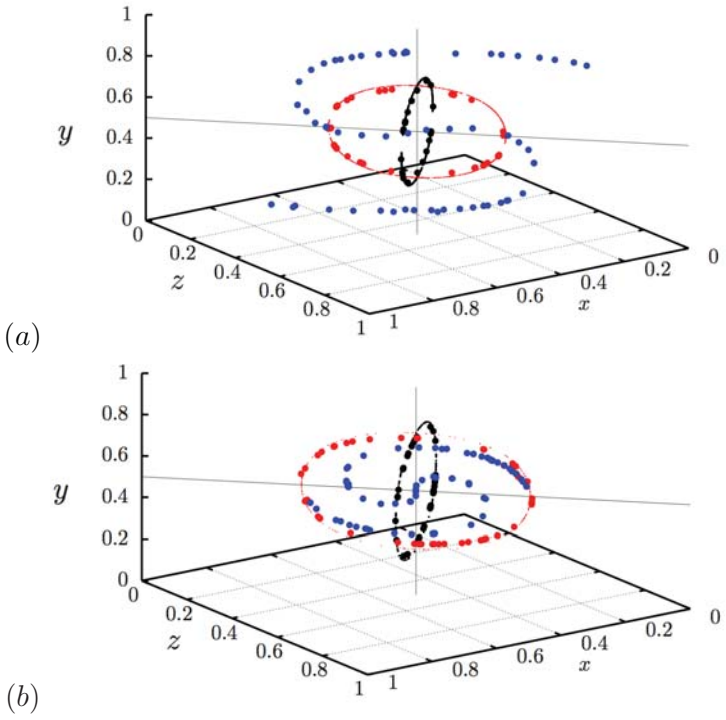

Figure 5.36: Settlement of periodic lines found for (a) Ra $= 9 \times 10^4$, and (b) Ra $= 5 \times 10^5$. Color black represents points on $x = z$ plane and blue and red points on $x = 1 - z$ plane. We added dots as an aid to the eye for the closed lines.

A qualitative phenomenon that is present in cases Ra $= 9 \times 10^4, 1 \times 10^5, 5 \times 10^5$ is that the radii at which merging of points, at 4-bifurcations in the first two cases and for the

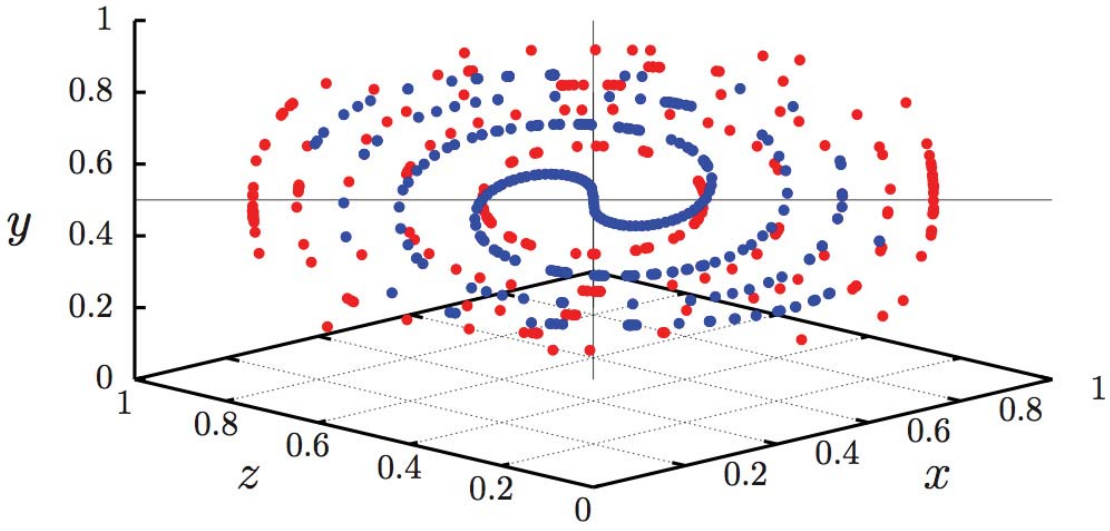

Figure 5.37: Settlement of periodic lines found for $\mathrm{Ra} = 5 \times 10^5$ on $x = 1 - z$ plane.

period doubling and double-saddle-node bifurcations in the last case, coincide with the presence of symmetric closed periodic lines. For $\mathrm{Ra} = 5 \times 10^4, 7 \times 10^4$ where we found also merging of points in 3-bifurcations we didn't find closed periodic lines. In fig. 5.39 we show the closed periodic lines and one invariant surface where we see merging of the sets of points for $\mathrm{Ra} = 1 \times 10^5$.

As we see in subsection 5.1.4, the line on the $x = 1 - z$ plane (black dots in fig. 5.39 (c)) is almost completely elliptic. A similar behavior is found for the blinking tumbler where the authors show a portion of a KAM tube that encircles the elliptic curve [25]. As we will express in the outlook of future studies at the end of this work, it would be very interesting to study in a deeper way the relation of periodic lines and invariant surfaces for this natural convective flow.

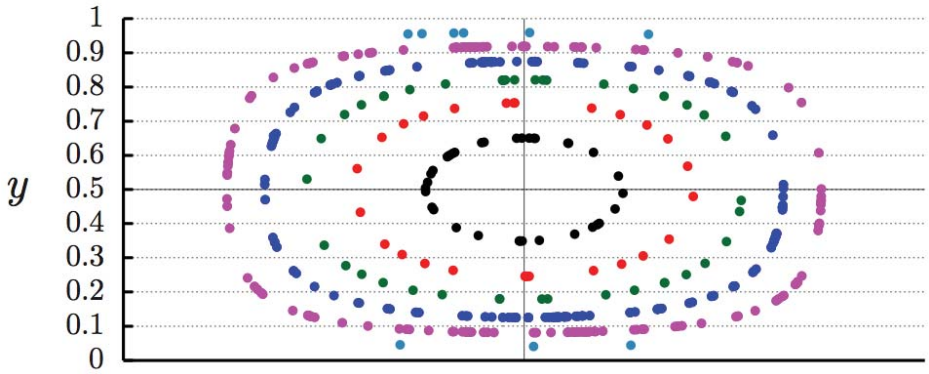

(a)

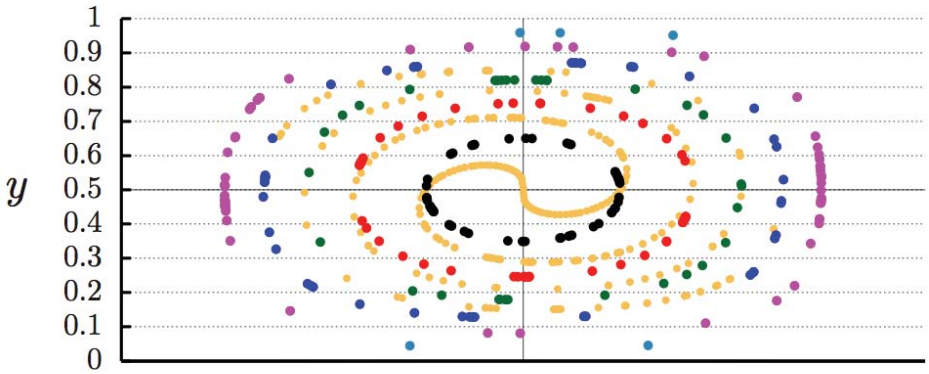

(b)

Figure 5.38: Settlement of periodic points found for Ra $= 5 \times 10^5$ on planes (a) $x = z$, (b), $x = 1 - z$.

(a) (b) (c)

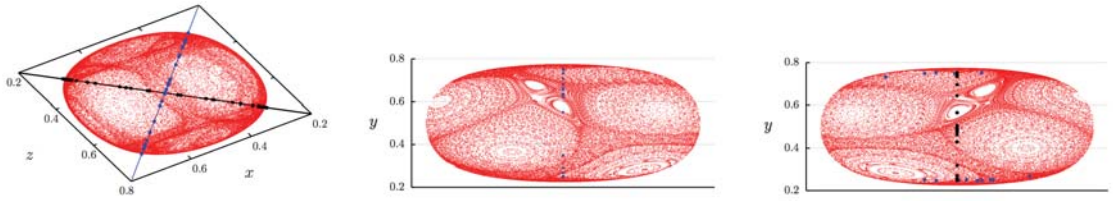

Figure 5.39: Closed periodic lines and one invariant surface where there is merging of points for the 4-bifurcation. Ra $= 1 \times 10^5$. Blue points represent the line on $x = z$ plane and black points the line on $x = 1 - z$ plane. In (a) we show a top view of the intersection. $(b) - (c)$ show a cut of this arrangement.

5.1.4 Classification of periodic points

In the previous subsection we showed the arrangement of periodic lines. As we described in section 4.2, we look for periodic points at the intersections of planes and invariant surfaces. We have constructed a finite number of surfaces and consequently, in some cases, little gaps between points forming the periodic lines exist, e.g., at closed periodic lines. Also we note that structures observed on invariant surfaces (q-tupling bifurcations) also affect the points on the intersection of planes and invariant surfaces. For example, if we have 'empty' regions on the Poincaré maps, those points will not be detected at the intersection with the planes. However, we want to stress that these two limitations can be resolved by building more invariant surfaces at specific regions and by inspecting more cycles on the construction of Poincaré maps, for instance. An alternative solution may be the use of surface tracking[6] of the symmetry planes as is the method actually used for the lid-driven cylinder flow [6, 2] and for the cubical lid-driven cavity flow [20].

In figs. 5.40-5.44 we can see the type of periodic points comprising the period-1 lines for different Rayleigh number. For $\mathrm{Ra} = 3 \times 10^4$ the line is completely elliptic, with increasing Rayleigh number, the line takes a more complicated shape with both elliptic and hyperbolic segments. From these figures we can see that open periodic lines are symmetric when we make a reflection about the $y = 0$ line plus a reflection of the plane $x = z$, this plane is represented as a vertical line in the following figures.

The behavior of the open periodic lines is similar to those found for the lid-driven cylinder flow with the two step forcing protocol that consists of a 'zigzag' movement of the top wall [18]. The segmentation of periodic lines for the lid-driven cylinder flow exhibits a strongly nonlinear dependence upon the displacement parameter [6], here we can see a similar behavior in function of the Rayleigh parameter.

[6]Further, surface tracking can also be used for visualization of natural convective flows as shown by de la Cruz et al. [61].

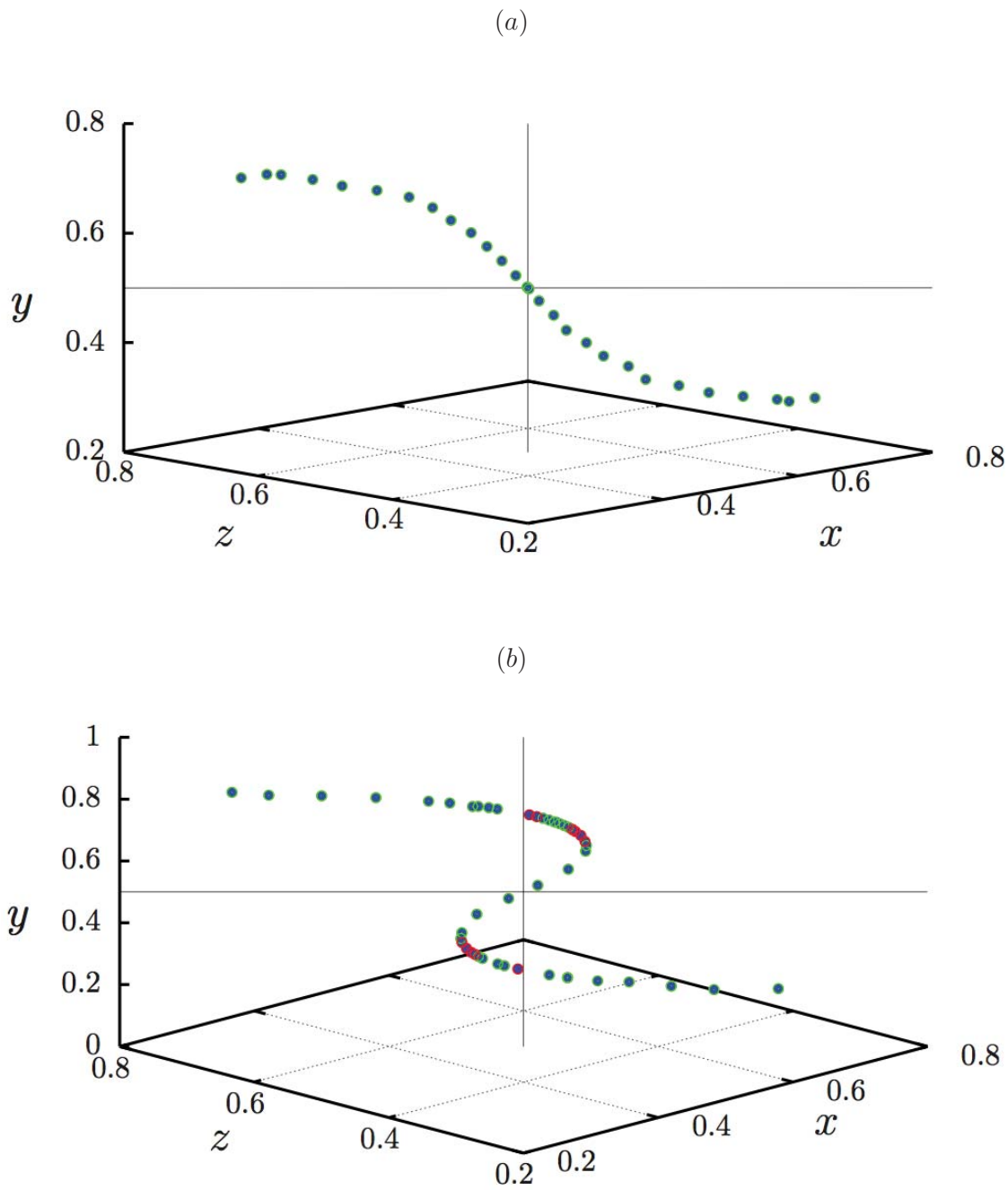

Figure 5.40: Period-1 lines on $x = 1-z$ plane. (a) Ra $= 3\times10^4$ and (b) Ra $= 5\times10^4$. Blue and green points represent elliptic periodic points and blue and red represent hyperbolic periodic points.

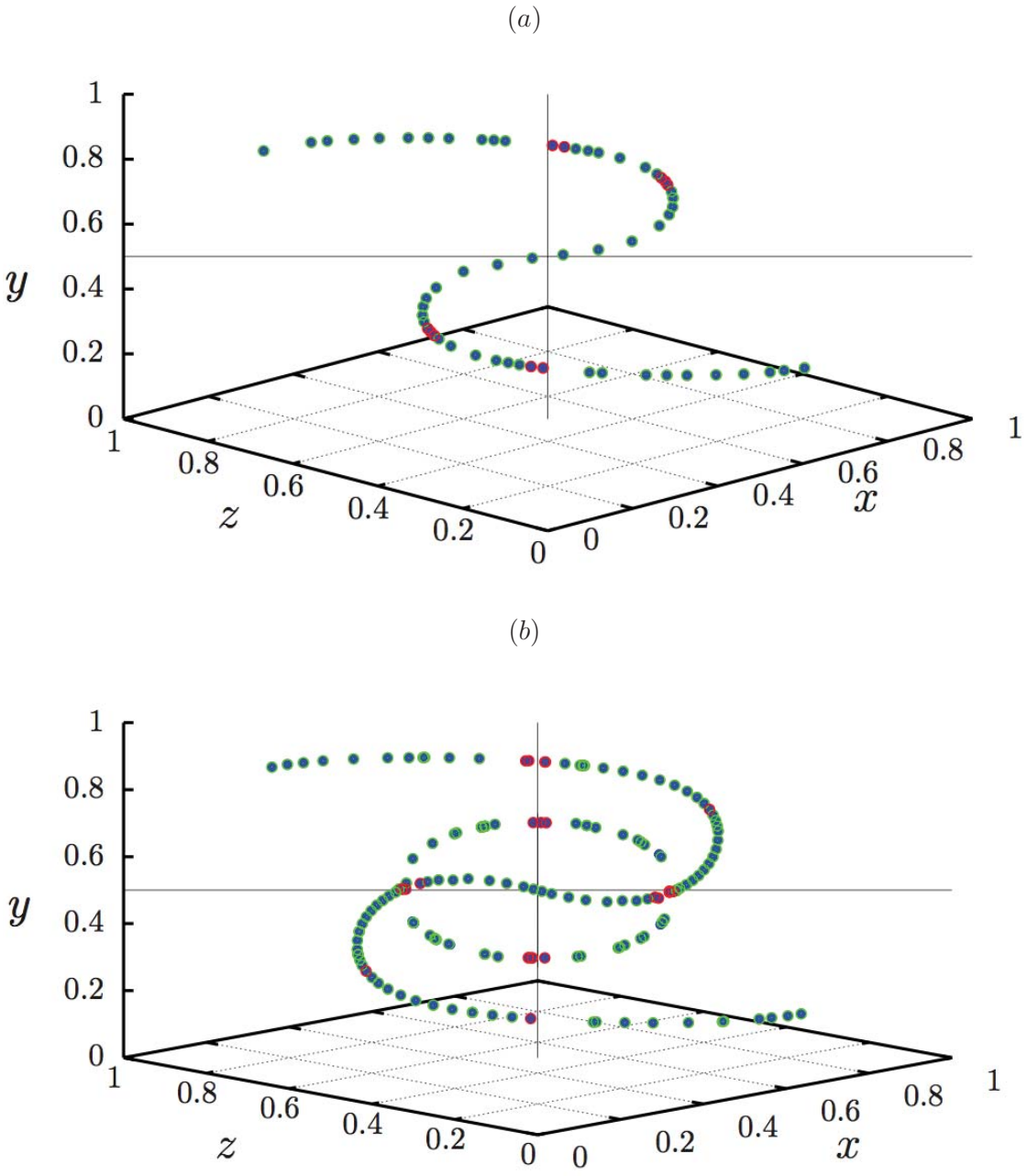

Figure 5.41: Period-1 lines on $x = 1-z$ plane. (a) Ra $= 7\times10^4$ and (b) Ra $= 9\times10^4$. Blue and green points represent elliptic periodic points and blue and red represent hyperbolic periodic points.

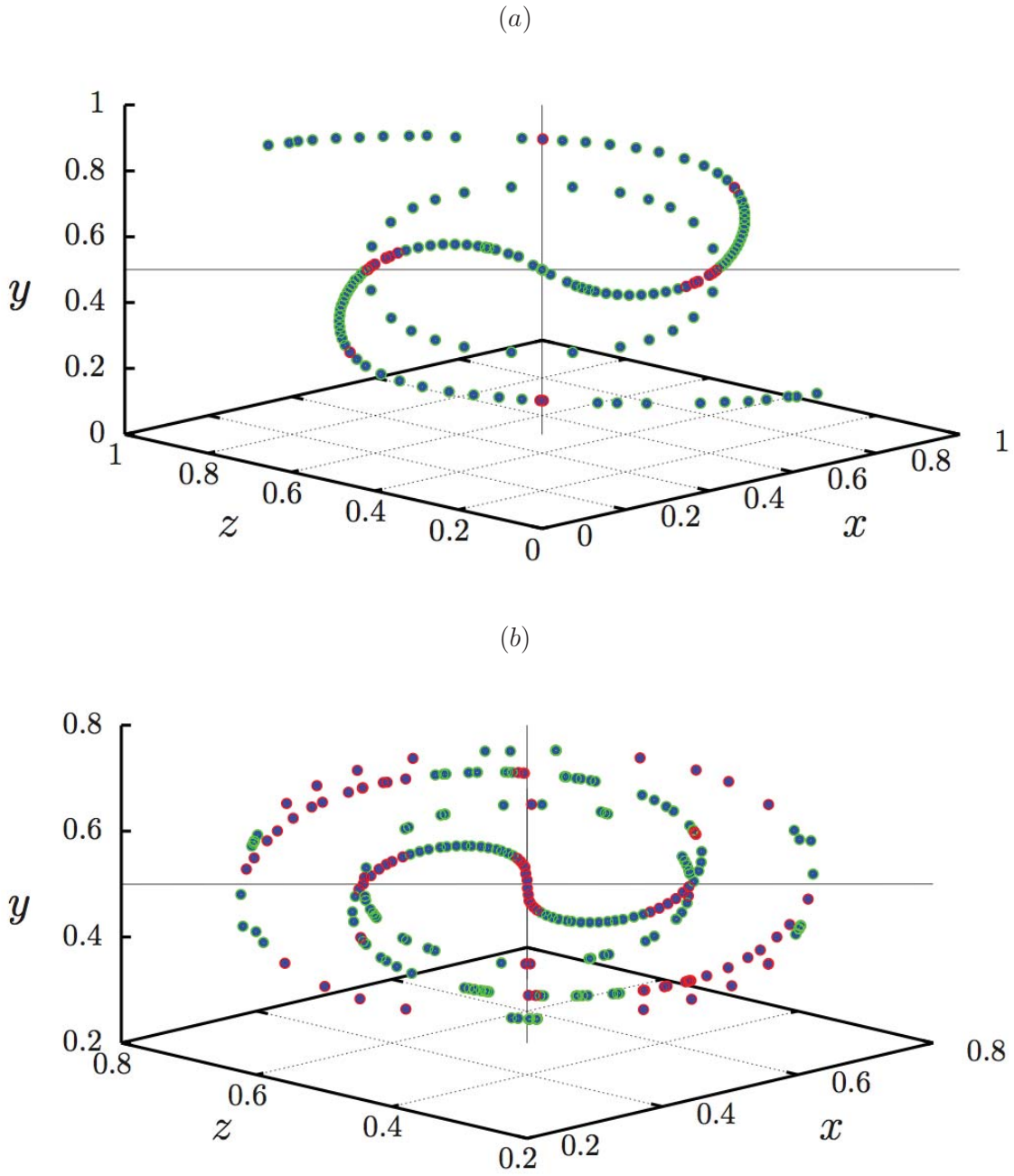

Figure 5.42: Period-1 lines on $x = 1-z$ plane. (a) Ra $= 1\times10^5$ and (b) Ra $= 5\times10^5$. Blue and green points represent elliptic periodic points and blue and red represent hyperbolic periodic points.

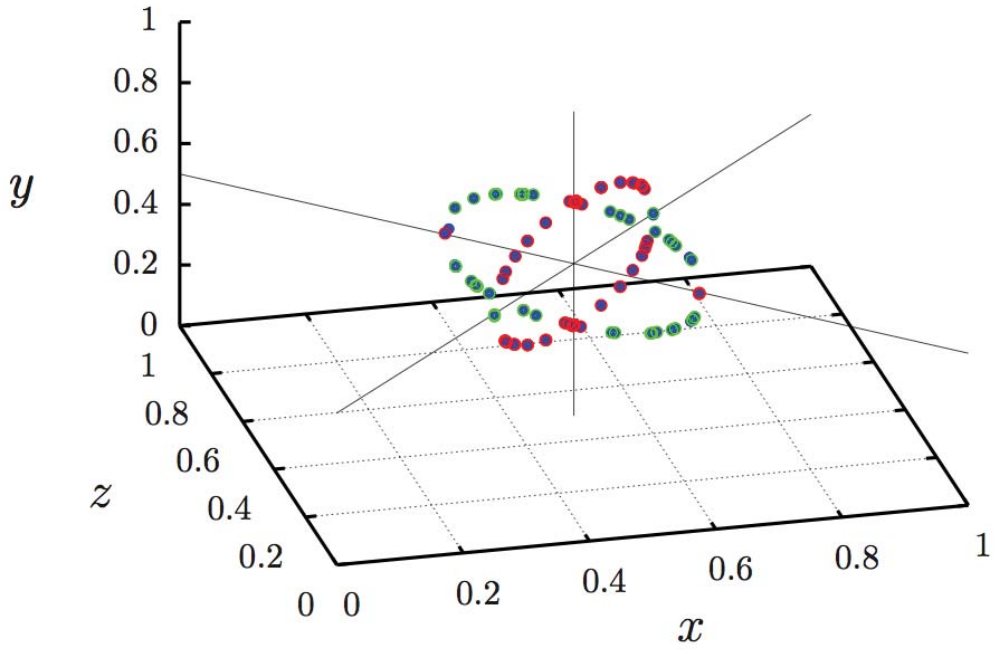

(*a*)

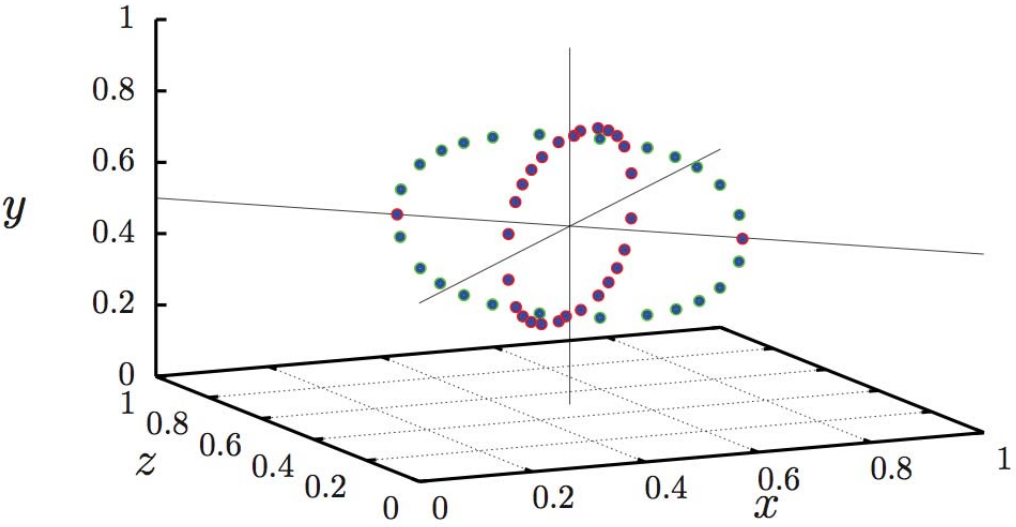

(*b*)

Figure 5.43: Classification of points for the closed period-1 line found on symmetry planes. (*a*) Ra $= 9 \times 10^4$. (*b*) Ra $= 1 \times 10^5$. Blue and green points represent elliptic periodic points and blue and red represent hyperbolic periodic points. We present a slightly different perspective in the two cases seeking the clarity of the figures.

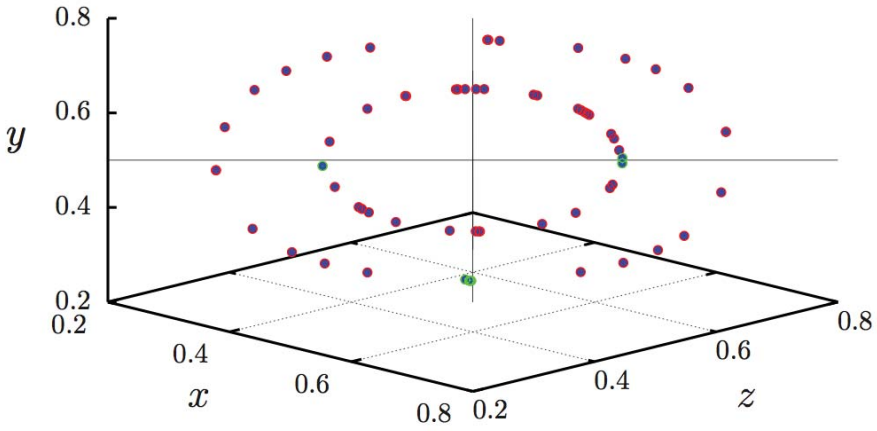

(*a*)

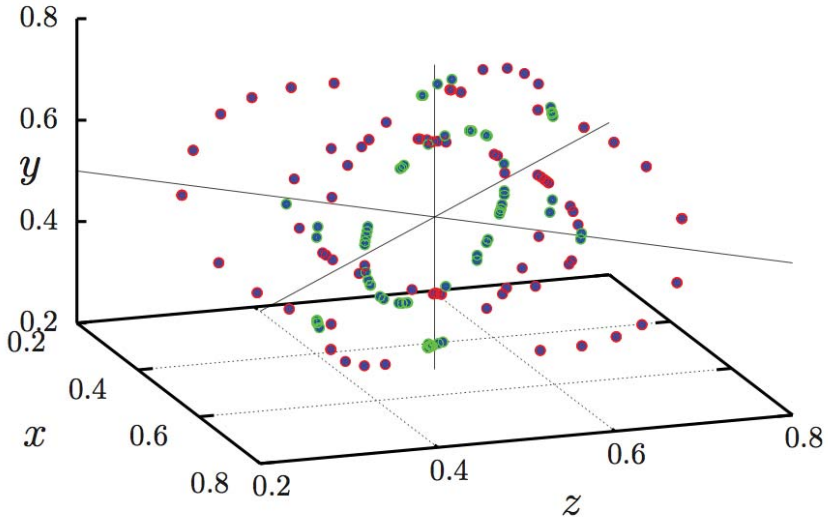

(*b*)

Figure 5.44: Classification of points for the closed period-1 line found on symmetry planes for $\mathrm{Ra} = 5 \times 10^5$. Blue and green points represent elliptic periodic points and blue and red represent hyperbolic periodic points. (*a*) Points on $x = z$ plane. (*b*) Arrangement of periodic points for four closed periodic lines.

For the case $\mathrm{Ra} = 9 \times 10^4$, the closed periodic line located on $x = 1 - z$ plane is almost completely elliptic except in the intersection with the other two lines, see fig. 5.43 (*a*). The closed periodic line located on $x = z$ plane is completely hyperbolic except for the intersection with the $y = 0.5$ line. A similar behavior is present for $\mathrm{Ra} = 1 \times 10^5$, see fig. 5.43 (*b*). In the discussion of the symmetries of this flow we commented the possibility of

having the plane $y = 0.5$ as a symmetry plane also, we have made a quick scan looking for periodic points on this plane and apparently they do exist for the cases where we find closed periodic lines. As we previously mentioned, this arrangement of closed periodic lines and the type of points forming them is similar to those found for the blinking tumbler [25, 65, 64].

We see that a very important requirement for the classification of periodic points is to have the highest possible accuracy in the determination of such points. In general, near the center of the cube we find the greater precision and when we move towards the walls the accuracy decreases. For that reason we choose to classify just a subset of periodic points for the case $\mathrm{Ra} = 5 \times 10^5$, see fig. 5.42 (b) and fig. 5.44. Here we can see that increasing Ra produces a bigger segmentation of the outer closed line on the $x = 1 - z$ plane, the lines on $x = z$ plane are almost fully hyperbolic, see fig. 5.44 (a).

For the full identification of parabolic points, the points where the behavior changes from elliptic to hyperbolic, we need the refinement of the method. To have more invariant surfaces at specific regions or to explore the surface tracking algorithm in order to decrease the space between points in the periodic lines near the position of the change. We have identified points that nearly fulfill the condition $\Lambda = \{1, 1, 1\}$ neighboring the position of fragmentation but as we have commented before for a good characterization of points we need accurate determination of the position of points.

As specific example to illustrate a more detailed analysis procedure, we chose two periodic points, one elliptic and one hyperbolic, of the open periodic line for $\mathrm{Ra} = 5 \times 10^5$ and we track points on a circle of radius 0.005 surrounding them on the symmetry plane $x = 1 - z$ for 1, 2, 3, 4 and 5 cycles in order to see the motion of the fluid in their vicinity. In fig. 5.45 (a) we show the initial circles and a segment of the periodic line. As we can see from fig. 5.45 (b), the circle of the hyperbolic point deforms in a much greater way exploring a larger region of the container than for the elliptic point, this different behavior is crucial in terms of zones of better mixing, see fig. 5.45 (b).

The behavior near the hyperbolic point can be the result of the interaction with the stable and unstable manifolds, a behavior studied for the lid-driven cylinder flow [18, 2]. It would be very interesting to analyze the deformation of material surfaces in order to determine stable and unstable manifolds of hyperbolic segments of periodic lines.

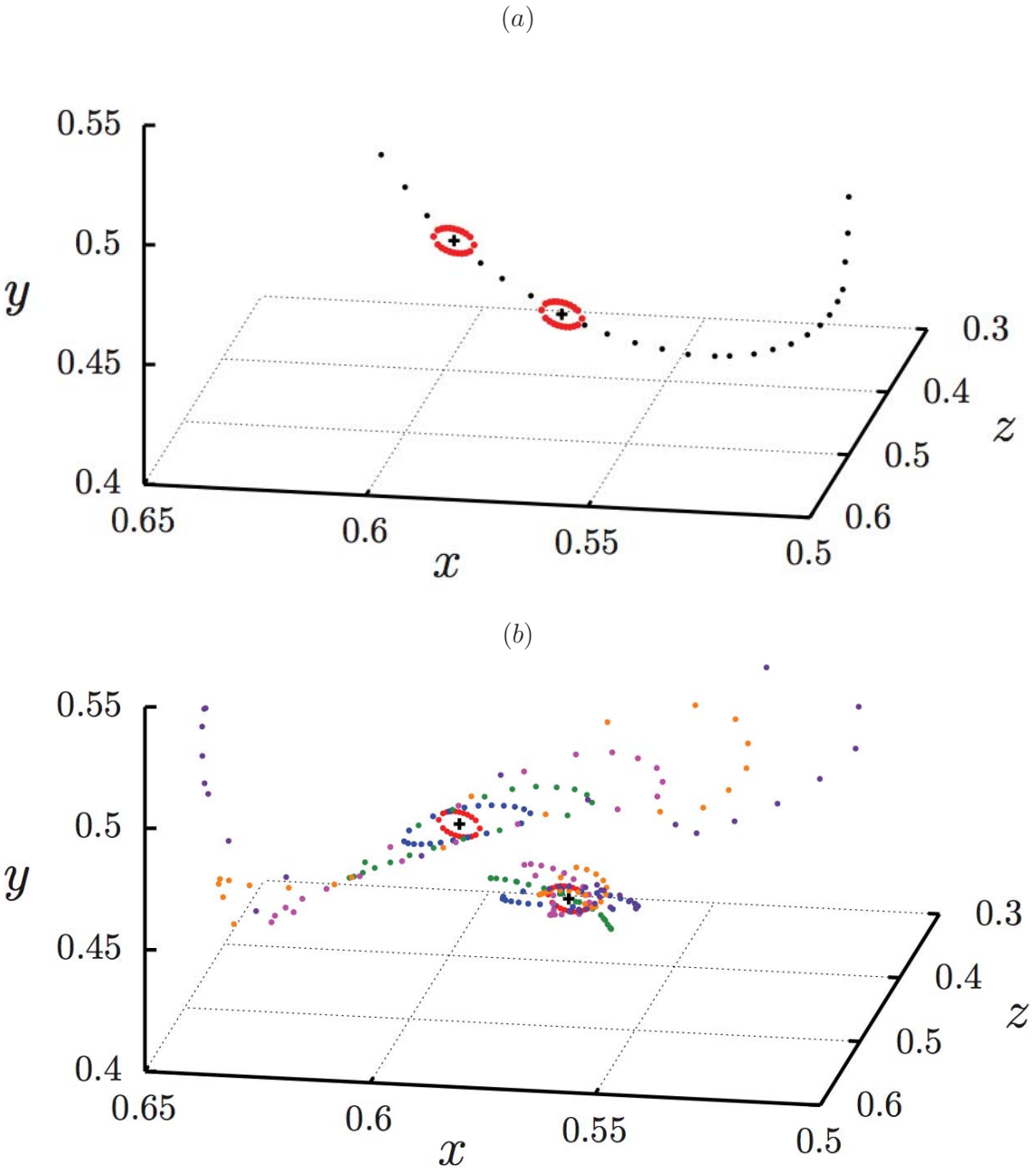

Figure 5.45: Ra $= 5 \times 10^5$. Tracking of initial circles surrounding two periodic points, crosses, on the $x = 1 - z$ plane. (a) The black points represent a segment of the periodic line and the red points are located at circles surrounding the hyperbolic point (top of the image) and the elliptic point. (b) Deformation of circles (red) for 1 (blue), 2 (green), 3 (pink), 4 (yellow) and 5 (purple) cycles.

Chapter 6

Summary

Conclusions

In this work we presented some topological properties for the natural convective flow inside a cubic container following the methodology presented for the lid-driven cylinder flow. In particular, we found invariant spheroids where trajectories of tracers are restricted. Intra-surface dynamics on invariant spheroids show a variety of forms that can be grouped in terms of Rayleigh number and that exhibit the complexity of area-preserving maps. We found period-1 lines for all the studied values of Rayleigh number and we have made a classification of periodic points that form these lines.

The phenomena observed in this work have been observed in a wide range of three-dimensional volume preserving maps with non-toroidal invariant surfaces, starting with the lid-driven cylinder flow [21, 6, 41, 4], the three-dimensional sphere-driven flow [26], the flow generated by the blinking rolls map [46], the three-dimensional lid-driven cube flow [20] and three-dimensional granular flows inside spherical tumbler [25, 65, 64]; specific similarities and differences have been pointed out at the appropriate places. As noted by Aref et al. [4], the emergence of similar dynamics in such a great variety of systems reflects the universality of many of the phenomena.

Future work

Many possible tasks have been identified as possible continuation of the present research, here we list a few.

In chapter 5 we presented some representative intra-surface dynamics found for the natural convective flow and the evolution of the periodic lines as functions of the Rayleigh number. At this point we have presented them as two separate phenomena but as we noted in section 2.2, intrasurface topologies are shaped essentially by the periodic points defined by the intersection of the invariant surfaces with periodic lines [6, 41]. This is beautifully shown for the flow driven by a rotating sphere [26]. We need to make a deeper study in order to relate our observations to this system.

Making an exhaustive study of the symmetries of our heating protocol can be of interest in order to fully understand the presence of periodic lines and also the symmetries shown by them. As shown for the lid-driven cylinder flow, protocols that lack of global symmetries

do not have periodic lines and can display isolated periodic points and three-dimensional chaos [21, 2].

The manifolds of isolated periodic points and hyperbolic segments of periodic lines are essential to the dynamics. As it is shown for the blinking tumbler, the invariant manifold template for chaotic transport can be applied to this kind of flows [25]. Such manifolds have been also presented for the lid-driven cylinder flow and the flow driven by a rotating sphere. An important tool that can be used to measure the degree of chaos are the Lyapunov exponents. For volume preserving maps in three dimensions the sum of the three exponents must be zero and when the orbits are restricted to two-dimensional surfaces, one of these exponents must be exactly equal to zero. A study of the Lyapunov exponents can be found for the blinking rolls map where the authors can see a clear correspondence between the existence of island structures and small Lyapunov exponents [46]. Determining the Lyapunov exponents is yet another task for continuing the study presented in this thesis.

A promising concept with Hamiltonian foundation and devised specifically for mixing application is found in the linked twist map [21], it may be of interest to explore possible connections regarding this convective flow.

Though the existence of invariant surfaces forbids three-dimensional mixing, mixing can occur on the invariant surfaces. This is associated with the elimination of islands. For the lid-driven cylinder flow it is shown that three-dimensional chaotic dynamics covering the entire flow domain can be achieved depending on the forcing protocol, moreover, when tracers are restricted to invariant surfaces, the dynamics can be changed by breaking such structures via perturbations of the linear problem.

As pointed out in the recent review of Frontiers of chaotic advection [4], the challenge ahead is the study of three-dimensional unsteady flows. The natural continuation of the work presented here is the inclusion of the nonlinear terms in the governing equations. The appearance of new structures by the inclusion of inertial effects in the lid-driven cylinder flow is thought to exemplify a universal mechanism and an important part of an essentially route to chaos of three-dimensional time-dependent flows [19, 4]. The dynamics of perturbed invariant spheroids remains largely an open problem. Fully-chaotic spheroids survive weak inertia and constitute transport barriers, non-chaotic regions of invariant spheroids have ramifications by causing the formation of intricate adiabatic structures through 'resonance induced merger' (RIM) [21, 4].

Some of the academic activities listed before are potential research projects that will contribute to the understanding of mixing with natural convection.

Appendix A

Dynamical systems

The motion of fluid particles in an Eulerian velocity field is a dynamical system[1]. In this work we are very interested in the solution,

$$\mathbf{x} = \mathbf{\Phi}_t(\mathbf{X}), \qquad \mathbf{X} = \mathbf{\Phi}_{t=0}(\mathbf{X}) \tag{A.1}$$

which is called *flow*[2] or *motion* (term from continuum mechanics), of

$$\frac{d\mathbf{x}}{dt} = \mathbf{v}(\mathbf{x}, t), \tag{A.2}$$

with $\mathbf{x} = \mathbf{X}$ at time $t = 0$. The flow is represented by a *mapping* or *map* or *point transformation*; $\mathbf{X}$ is mapped to $\mathbf{x}$ after a time t[3]. In the language of dynamical systems a mapping

$$\mathbf{\Phi}_t(\mathbf{X}) \to \mathbf{x} \tag{A.3}$$

is called a C^k diffeomorphism if it is 1-1 and onto, and both $\mathbf{\Phi}_t(\cdot)$ and its inverse are k-times differentiable. The transformation (A.1) is required to satisfy the condition for the Jacobian, $J = \det(\frac{\partial x_i}{\partial X_j}) = \det(D\mathbf{\Phi}_t(\mathbf{X}))$,

$$0 < J < \infty. \tag{A.4}$$

Eq. (A.4) precludes two particles $\mathbf{X}_1$ and $\mathbf{X}_2$, from occupying the same position $\mathbf{x}$ at a given time, or one particle splitting into two (non-topological motions such as breakup or coalescence are not allowed).

In the language of dynamical systems theory, a map, S, is an example of a *measure-preserving transformation*. If R denote the region occupied by the fluid, and A is any subdomain of R, $\mu(A)$ denotes the volume of A. μ is a function that assigns to any subdomain of R its volume; the function μ is known as a *measure*. Incompressibility of the fluid is expressed as $\mu(A) = \mu(S(A))$ [1].

Here we consider that a *continuous dynamical system* is a system of differential equations (A.5) and its associated flow

$$\frac{d\mathbf{x}}{dt} = \mathbf{f}(\mathbf{x}, t), \tag{A.5}$$

[1] We deal exclusively with either autonomous systems or time-periodic systems following [10, Chapter 5].

[2] Here $\mathbf{x} = \mathbf{\Phi}_t(\mathbf{X})$ is usually assumed to be invertible and differentiable.

[3] Here we are identifying a point in a continuum by its initial position vector, i.e., eq. (A.1) means that the initial condition of particle $\mathbf{X}$ occupies the position $\mathbf{x}$ at time t.

$\mathbf{x} \in \mathbf{R}^n$ and the right hand side is arbitrary. An important case occurs when $\mathbf{f}$ is periodic in time ($\mathbf{f}(\mathbf{x}, t) = \mathbf{f}(\mathbf{x}, t + T)$). The space $\mathbf{x}$, with t as a parameter or with $\mathbf{x}$ augmented by t ($\mathbf{R}^n \times \mathbf{R}$ if the time t is added as one of the axes), is called de *phase space* of the flow. Given any point $\mathbf{x}_0$ belonging to the phase space at some time arbitrarily designated as zero, the orbit or trajectory based at $\mathbf{x}_0$ is given by $\mathbf{\Phi}_t(\mathbf{x}_0)$ for all times t.

When we do not follow the trajectory of every initial condition continuously in time through the phase space we can record their positions at specified times[4]. Consider for example that the position of the initial condition $\mathbf{X} = \mathbf{x}_0$ is recorded every $t = T$, in this case

$$\mathbf{x}_n = \mathbf{\Phi}_T^n(\mathbf{x}_0) \tag{A.6}$$

where $\mathbf{\Phi}_T^n(\cdot)$ denotes the composition of n mappings $\mathbf{\Phi}_T$ (alternative ways of expressing the same concept are $\mathbf{x}_n \to \mathbf{\Phi}_T(\mathbf{x}_n)$ and $\mathbf{x}_{n+1} = \mathbf{\Phi}_T(\mathbf{x}_n)$). Mappings as (A.6) are referred as *discrete dynamical systems*.

Given a flow $\mathbf{x} = \mathbf{\Phi}_t(\mathbf{X})$, $\mathbf{P}$ is a *fixed point* of the flow if

$$\mathbf{P} = \mathbf{\Phi}_t(\mathbf{P}) \tag{A.7}$$

for all time t, that is, the particle located at the position $\mathbf{P}$ stays at $\mathbf{P}$. $\mathbf{P}$ is a *periodic point* of period T (belonging to a periodic or closed orbit) if

$$\mathbf{P} = \mathbf{\Phi}_T(\mathbf{P}), \tag{A.8}$$

the particle located at the position $\mathbf{P}$ with orbit $\mathbf{x} = \mathbf{\Phi}_t(\mathbf{P})$ returns to its initial position after a time T ($\mathbf{\Phi}_t(\mathbf{P} \neq \mathbf{P})$ for any $t < T$).

A point $\mathbf{P}$ is a *fixed point of the mapping* $\mathbf{f}(\cdot)$ if[5]

$$\mathbf{P} = \mathbf{f}^n(\mathbf{P}) \tag{A.9}$$

for all n. We say that $\mathbf{P}$ is a *periodic point of order* n of the map $\mathbf{f}(\cdot)$ if

$$\mathbf{P} = \mathbf{f}^n(\mathbf{P}), \tag{A.10}$$

$\mathbf{P}$ returns to its initial location after exactly n iterations ($\mathbf{f}^n(\mathbf{P}) \neq \mathbf{P}$ for any $m < n$). In fluid mixing a very common way of generating mappings from flows is by means of the *Poincaré surface of section*.

A flow $\mathbf{\Phi}_t(\cdot)$ in a region S displays chaos when it satisfies one of the following conditions[6] [10, 15]:

[4] If we think of the number of dimensions, it is clear that there is a visualization problem. For a two-degree-of freedom (Hamiltonian) system, the phase space is four-dimensional and, if conservative, the energy shell is three-dimensional and even following the motion on this $3D$ energy shell is difficult. The surface of section is a most valuable technique to this end [14].

[5] A fixed point of a flow and its corresponding mapping are in general not the same. Generally, a fixed point of a mapping corresponds to a periodic point of the flow.

[6] In a strict sense, the definitions are not equivalent, although for many purposes in fluid mixing they might be regarded to be so [15]. There are also other possible definitions for temporal chaos [10]. For a brief discussion of the term chaos in the context of chaotic advection, see [1].

- There is an invariant set[7] S ($\mathbf{\Phi}_t(S) = S$) and the flow is sensitive to initial conditions[8] on S.
- The flow has transverse homoclinic and/or heteroclinic points.
- The flow produces horseshoe maps.

A.1 Hamiltonian systems

Golubitsky & Stewart [45] study generic bifurcations of Hamiltonian systems with symmetry (see [68] for a definition of this concept, the idea is that the Hamiltonian H is invariant under a compact Lie group Γ which preserves the symplectic structure). The authors seek conditions on the group in order that bifurcations cannot be changed by small Γ-invariant perturbations of H. We are particularly interested in section 4 of this work were they summarize generic bifurcations (when eigenvalues pass through zero) of Hamiltonian systems with one-degree-of-freedom[9] for different symmetry groups, $\mathbf{1}$, $\mathbb{Z}_n$ and SO(2). This material can also be found in references [68, 48, 47], we also recommend [69, Appendix 7].

$\mathbb{Z}_n$ is the cyclic group of order n (the order or a finite group is the number of elements of the group), this is the set of rotational symmetries of a regular n-sided polygon. It consists of rotations of the plane through the angles $0, \theta, ..., (n-1)\theta$, where $\theta = 2pi/n$. The action of this group on $\mathbb{R}^2$ (identifying it with $\mathbb{C}$) is given by $\theta \cdot z = e^{i\theta} z$ [68, 45].

$\Gamma = \mathbf{1}$

The Hamiltonian is generically

$$H(p, q) = \pm p^3 \pm q^2 + ..., \tag{A.11}$$

and the model 1-parameter has the normal form[10]

$$H(p, q, \lambda) = p^3 + q^2 + \lambda p. \tag{A.12}$$

[7] A set S is called an *invariant* set of the flow $\mathbf{x} = \mathbf{\Phi}_t(\mathbf{X})$ on a manifold M ($S \subset M$) if $\mathbf{\Phi}_t(\mathbf{X}) \in S$ for all $\mathbf{X} \in S$, for all time t. If a point belongs to an invariant set, then when acted by the flow, it remains in the set.

[8] The flow $\mathbf{\Phi}_t(\mathbf{X})$ is said to be sensitive to initial conditions on a domain S if for all $\mathbf{X} \neq \mathbf{X}_0$, with $\mathbf{X}$ belonging to an ϵ-ball around $\mathbf{X}_0$, there exists a time, $t < \infty$ such that $\mathbf{\Phi}_t(\mathbf{X})$ lies outside the ϵ-ball for all the $\mathbf{X}_0$ contained in S. A similar definition applies to maps [10].

[9] Bifurcations in Hamiltonian systems with two degrees of freedom can be reduced to an investigation of a one-parameter Hamiltonian systems with one degree of freedom [69].

[10] The method of normal forms provides a way of finding a coordinate system in which a dynamical system takes the 'simplest' form, see [68, 48], though a description of normal forms is beyond the scope of the present study.

Level curves exhibit 'fish' structure bifurcation when the parameter changes from $\lambda > 0$ to $\lambda < 0$. This is the analog to the saddle-node bifurcation for Hamiltonian systems, as a parameter is varied two equilibria, a saddle and a center, collide and disappear, leaving no fixed points.

$\Gamma = \mathbb{Z}_2$

The model normal form in this case is

$$H(p, q, \lambda) = p^4 + q^2 + \lambda p^2. \tag{A.13}$$

The level curves presents the 'figure eight' generic bifurcation when the parameter changes from $\lambda > 0$ to $\lambda < 0$.

$\Gamma = \mathbb{Z}_m \ (m \geq 3)$

Here the authors obtain the normal forms

$$(z\overline{z})^2 + Rez^m - \lambda z\overline{z} \qquad (m \geq 5), \tag{A.14}$$

$$(z\overline{z})^2 + \gamma Rez^4 - \lambda z\overline{z} \qquad (m = 4), \tag{A.15}$$

$$Rez^3 - \lambda z\overline{z} \qquad (m = 3), \tag{A.16}$$

where the parameter $\gamma \neq 0, \pm 1$. The level curves of the normal form for $m = 3$, exhibit a *3-bifurcation* (there exists a hyperbolic periodic orbit of period 3 for positive and negative values of the parameter and it tends to the 3-bifurcation point as the parameter goes to 0).

For $m \geq 5$ the level curves of the normal form are typical of m-bifurcation points (there exist an elliptic and also a hyperbolic periodic orbits of period m for positive value (respectively negative) of the parameter and no periodic orbit of period m for negative value (respectively positive) of the parameter, as the parameter goes to 0 from the appropriate side, both orbits tend to the m-bifurcation point), see [48, Chapter 11].

The authors consider separately the case $m = 4$ since it has special features. As γ is changed to $-\gamma$ the phase portrait is unchanged except for a rotation. And therefore they assume $\gamma \geq 0$. There are two exceptional values of γ, 0 and 1 (or -1) at which the topology of the phase portrait changes. They show the transition of the two portraits for values $\gamma = 0.5$ and 1.5. This bifurcation can behave either like $m = 3$ or like $m > 4$ [66, 48].

Appendix B

Incompressibility constraint

$\mathrm{Ra} = 5 \times 10^5$, mesh: 96^3	
Step of the protocol	$\nabla \cdot \mathbf{u}$
1	$9.14127e-06$
2	$8.62083e-06$
3	$8.72801e-06$
4	$8.65373e-06$

Table B.1: Incompressibility constraint for $\mathrm{Ra} = 5 \times 10^5$, computational mesh: 96^3.

$\mathrm{Ra} = 1 \times 10^5$, mesh: 96^3	
Step of the protocol	$\nabla \cdot \mathbf{u}$
1	$9.55421e-06$
2	$8.65632e-06$
3	$7.61257e-06$
4	$8.67739e-06$

Table B.2: Incompressibility constraint for $\mathrm{Ra} = 1 \times 10^5$, computational mesh: 96^3.

$\mathrm{Ra} = 1 \times 10^5$, mesh: 128^3	
Step of the protocol	$\nabla \cdot \mathbf{u}$
1	$2.88287e-05$
2	$2.59745e-05$
3	$2.87175e-05$
4	$2.63960e-05$

Table B.3: Incompressibility constraint for $\mathrm{Ra} = 1 \times 10^5$, computational mesh: 128^3.

$\mathrm{Ra} = 9 \times 10^4$, mesh: 128^3	
Step of the protocol	$\nabla \cdot \mathbf{u}$
1	$2.81003e-05$
2	$2.61406e-05$
3	$2.84726e-05$
4	$2.66368e-05$

Table B.4: Incompressibility constraint for $\mathrm{Ra} = 9 \times 10^4$, computational mesh: 128^3.

$\mathrm{Ra} = 7 \times 10^4$, mesh: 96^3	
Step of the protocol	$\nabla \cdot \mathbf{u}$
1	$7.84445e-06$
2	$8.90510e-06$
3	$8.90597e-06$
4	$8.92077e-06$

Table B.5: Incompressibility constraint for $\mathrm{Ra} = 7 \times 10^4$, computational mesh: 96^3.

$\mathrm{Ra} = 5 \times 10^4$, mesh: 96^3	
Step of the protocol	$\nabla \cdot \mathbf{u}$
1	$5.88451e-06$
2	$8.90308e-06$
3	$6.94999e-06$
4	$8.91544e-06$

Table B.6: Incompressibility constraint for $\mathrm{Ra} = 5 \times 10^4$, computational mesh: 96^3.

$\mathrm{Ra} = 3 \times 10^4$, mesh: 96^3	
Step of the protocol	$\nabla \cdot \mathbf{u}$
1	$5.74044e-06$
2	$8.46982e-06$
3	$4.33433e-06$
4	$8.48091e-06$

Table B.7: Incompressibility constraint for $\mathrm{Ra} = 3 \times 10^4$, computational mesh: 96^3.

References

[1] S. Wiggins and J. M. Ottino. Foundations of chaotic mixing. *Philosophical Transactions of the Royal Society of London. Series A: Mathematical, Physical and Engineering Sciences* **362** no. 1818 (2004), pp. 937–970. Cited 5 times on pp. 13, 16, 19, 109, 110.

[2] M. Speetjens, H. Clercx and G. van Heijst. A numerical and experimental study on advection in three-dimensional stokes flows. *Journal of Fluid Mechanics* **514** (2004), pp. 77–105. Cited 11 times on pp. 13, 17, 18, 22, 32, 33, 63, 64, 98, 104, 108.

[3] J. M. Ottino. Mixing, chaotic advection, and turbulence. *Annual Review of Fluid Mechanics* **22** no. 1 (1990), pp. 207–254. Cited 3 times on pp. 13, 19, 21.

[4] H. Aref, J. R. Blake, M. Budišić et al. Frontiers of chaotic advection. arXiv:1403.2953 [nlin.CD]. Cited 13 times on pp. 13, 16, 17, 18, 20, 21, 22, 23, 29, 36, 41, 107, 108.

[5] R. Sturman, J. M. Ottino and S. Wiggins. *The mathematical foundations of mixing: the linked twist map as a paradigm in applications: micro to macro, fluids to solids*, vol. 22 (Cambridge University Press, 2006). Cited 2 times on pp. 13, 71.

[6] Z. Pouransari, M. Speetjens and H. Clercx. Formation of coherent structures by fluid inertia in three-dimensional laminar flows. *Journal of Fluid Mechanics* **654** no. 1 (2010), p. 5. Cited 17 times on pp. 13, 18, 21, 29, 31, 32, 34, 35, 37, 38, 64, 65, 71, 85, 92, 98, 107.

[7] A. Figueroa, P. Meunier, S. Cuevas, E. Villermaux and E. Ramos. Chaotic advection at large péclet number: Electromagnetically driven experiments, numerical simulations, and theoretical predictions. *Physics of Fluids* **26** no. 1 (2014), pp. 013 601 1–14. Cited 1 time on p. 13.

[8] H. Aref. Stirring by chaotic advection. *Journal of fluid mechanics* **143** no. 1 (1984), pp. 1–21. Cited 1 time on p. 13.

[9] J. M. Ottino. The mixing of fluids. *Scientific American* **260** no. 1 (1989), pp. 56–57. Cited 1 time on p. 13.

[10] J. M. Ottino. *The kinematics of mixing: stretching, chaos, and transport*, vol. 3 (Cambridge University Press, 1989). Cited 12 times on pp. 13, 19, 20, 21, 30, 39, 40, 41, 71, 109, 110, 111.

[11] P. Galison. *Einstein's Clocks, Poincaré's Maps: Empires of Time* (WW Norton & Company, 2003). Cited 1 time on p. 14.

[12] B. G. June. Poincaré and the three body problem. history of mathematics. *American Mathematical Society* **11**. Cited 2 times on pp. 14, 15.

[13] P. Holmes. Poincaré, celestial mechanics, dynamical-systems theory and "chaos". *Physics Reports* **193** no. 3 (1990), pp. 137–163. Cited 2 times on pp. 15, 17.

[14] M. Tabor. *Chaos and integrability in nonlinear dynamics: an introduction*, vol. 165 (Wiley New York, 1989). Cited 6 times on pp. 15, 39, 40, 41, 42, 110.

[15] J. Ottino, S. Jana and V. Chakravarthy. From reynolds's stretching and folding to mixing studies using horseshoe maps. *Physics of Fluids* **6** no. 2 (1994), pp. 685–699. Cited 4 times on pp. 16, 20, 34, 110.

[16] J. Ottino, F. Muzzio, M. Tjahjadi, J. Franjione, S. C. Jana and H. Kusch. Chaos, symmetry, and self-similarity: exploiting order and disorder in mixing processes. *Science* **257** no. 5071 (1992), pp. 754–760. Cited 2 times on pp. 16, 34.

[17] G. Metcalfe, M. Speetjens, D. Lester and H. Clercx. Beyond passive: Chaotic transport in stirred fluids. In E. van der Giessen and H. Aref (eds.), *Advances in Applied Mechanics*, vol. 45, pp. 109–188 (Elsevier, 2012). Cited 1 time on p. 16.

[18] V. Malyuga, V. Meleshko, M. Speetjens, H. Clercx and G. van Heijst. Mixing in the stokes flow in a cylindrical container. *Proceedings of the Royal Society of London. Series A: Mathematical, Physical and Engineering Sciences* **458** no. 2024 (2002), pp. 1867–1885. Cited 9 times on pp. 17, 29, 30, 31, 32, 92, 95, 98, 104.

[19] S. Wiggins. Coherent structures and chaotic advection in three dimensions. *Journal of Fluid Mechanics* **654** (2010), pp. 1–4. Cited 4 times on pp. 17, 18, 41, 108.

[20] P. Anderson, O. Galaktionov, G. Peters, F. van de Vosse and H. Meijer. Analysis of mixing in three-dimensional time-periodic cavity flows. *Journal of Fluid Mechanics* **386** (1999), pp. 149–166. Cited 6 times on pp. 17, 30, 60, 95, 98, 107.

[21] M. F. Speetjens and H. J. Clercx. Formation of coherent structures in a class of realistic 3D unsteady flows. In J. K. et al. (ed.), *Fluid Dynamics in Physics, Engineering and Environmental Applications*, pp. 139–157 (Springer, 2013). Cited 8 times on pp. 17, 18, 21, 36, 41, 63, 107, 108.

[22] L. M. de la Cruz and E. Ramos. Mixing with time dependent natural convection. *International communications in heat and mass transfer* **33** no. 2 (2006), pp. 191–198. Cited 2 times on pp. 18, 47.

[23] J. H. Cartwright, M. Feingold and O. Piro. Chaotic advection in three-dimensional unsteady incompressible laminar flow. *Journal of Fluid Mechanics* **316** (1996), pp. 259–284. Cited 4 times on pp. 20, 21, 22, 37.

[24] M. Feingold, L. P. Kadanoff and O. Piro. Passive scalars, three-dimensional volume-preserving maps, and chaos. *Journal of statistical physics* **50** no. 3-4 (1988), pp. 529–565. Cited 3 times on pp. 21, 33, 37.

[25] I. C. Christov, R. M. Lueptow, J. M. Ottino and R. Sturman. A study in three-dimensional chaotic dynamics: Granular flow and transport in a bi-axial spherical tumbler. *SIAM Journal on Applied Dynamical Systems* **13** no. 2 (2014), pp. 901–943. Cited 10 times on pp. 21, 33, 36, 66, 78, 95, 96, 104, 107, 108.

[26] N. Moharana, M. Speetjens, R. Trieling and H. Clercx. Three-dimensional lagrangian transport phenomena in unsteady laminar flows driven by a rotating sphere. *Physics of Fluids* **25** no. 9 (2013), p. 093 602. Cited 5 times on pp. 21, 35, 60, 65, 107.

[27] M. Speetjens, H. Clercx and G. van Heijst. Merger of coherent structures in time-periodic viscous flows. *Chaos: An Interdisciplinary Journal of Nonlinear Science* **16** no. 4 (2006), pp. 043 104 1–8. Cited 3 times on pp. 21, 36, 37.

[28] H. Aref. The development of chaotic advection. *Physics of fluids* **14** no. 4 (2002), pp. 1315–1325. Cited 1 time on p. 22.

[29] K. El Omari and Y. Le Guer. Alternate rotating walls for thermal chaotic mixing. *International Journal of Heat and Mass Transfer* **53** no. 1 (2010), pp. 123–134. Cited 1 time on p. 23.

[30] Y. Le Guer and K. El Omari. Chaotic advection for thermal mixing. In E. van der Giessen and H. Aref (eds.), *Advances in applied mechanics*, vol. 45, pp. 189–237 (Elsevier, 2012). Cited 1 time on p. 23.

[31] H. Schlichting and K. Gersten. *Boundary-layer theory* (Springer, 2000). Cited 2 times on pp. 23, 45.

[32] S. Chandrasekhar. *Hydrodynamic and Hydromagnetic Stability* (Oxford, 1961). Cited 2 times on pp. 24, 25.

[33] L. Landau and E. Lifshitz. Fluid mechanics, 1987. *Course of Theoretical Physics* . Cited 1 time on p. 24.

[34] I. G. Currie. *Fundamental mechanics of fluids* (CRC Press, 2003). Cited 1 time on p. 24.

[35] D. Gray and A. Giorgini. The validity of the boussinesq approximation for liquids and gases. *International Journal of Heat and Mass Transfer* **19** no. 5 (1976), pp. 545–551. Cited 1 time on p. 25.

[36] E. Ramos and M. Vargas. The boussinesq approximation in a rotating frame of reference. *Journal of Non-Equilibrium Thermodynamics* **30** no. 1 (2005), pp. 21–37. Cited 1 time on p. 25.

[37] L. M. de la Cruz. *Solución del problema de convección utilizando volumen finito y algoritmos paralelos*. Notas de Modelación y Métodos Numéricos 4 (CIMAT, 2011). Cited 5 times on pp. 26, 53, 54, 56, 57.

[38] H. Versteeg and W. Malalasekera. *An introduction to computational fluid dynamics: The finite volume method* (Pearson Education Limited, 2007). Cited 4 times on pp. 26, 54, 56, 58.

[39] J. M. Ottino. Kinematical views of mixing of fluids and granular materials: a brief review and open questions. *Revista Mexicana de Física* **44** no. 3 (1998), pp. 215–221. Cited 1 time on p. 30.

[40] J. Znaien, M. Speetjens, R. Trieling and H. Clercx. Observability of periodic lines in three-dimensional lid-driven cylindrical cavity flows. *Physical Review E* **85** no. 6 (2012), p. 066 320. Cited 3 times on pp. 30, 35, 92.

[41] M. Speetjens, H. Clercx and G. van Heijst. Inertia-induced coherent structures in a time-periodic viscous flow. *Physics of Fluids* **18** no. 8 (2006), pp. 083 603 1–15. Cited 7 times on pp. 32, 33, 36, 37, 38, 65, 107.

[42] J. G. Franjione, C. W. Leong and J. M. Ottino. Symmetries within chaos: a route to effective mixing. *Physics of Fluids A* **1** no. 11 (1989), pp. 1772–1783. Cited 3 times on pp. 33, 34, 64.

[43] J. Franjione and J. Ottino. Symmetry concepts for the geometric analysis of mixing flows. *Philosophical Transactions of the Royal Society of London. Series A: Physical and Engineering Sciences* **338** no. 1650 (1992), pp. 301–323. Cited 3 times on pp. 33, 34, 66.

[44] A. Gómez and J. Meiss. Volume-preserving maps with an invariant. *Chaos: An Interdisciplinary Journal of Nonlinear Science* **12** no. 2 (2002), pp. 289–299. Cited 1 time on p. 35.

[45] M. Golubitsky, I. Stewart and J. Marsden. Generic bifurcation of Hamiltonian systems with symmetry. *Physica D: Nonlinear Phenomena* **24** no. 1 (1987), pp. 391–405. Cited 3 times on pp. 36, 65, 111.

[46] P. Mullowney, K. Julien and J. Meiss. Blinking rolls: chaotic advection in a three-dimensional flow with an invariant. *SIAM Journal on Applied Dynamical Systems* **4** no. 1 (2005), pp. 159–186. Cited 7 times on pp. 36, 65, 66, 71, 85, 107, 108.

[47] R. S. MacKay. *Renormalisation in area-preserving maps*, vol. 6 (World Scientific, 1993). Cited 3 times on pp. 36, 44, 111.

[48] K. Meyer, G. Hall and D. Offin. *Introduction to Hamiltonian dynamical systems and the N-body problem* (Springer, 2009). Cited 4 times on pp. 36, 66, 111, 112.

[49] K. C. Lee, S. Y. Kim and D. I. Choi. Universality of k 3^n and k 4^n bifurcations in area-preserving maps. *Physics Letters A* **103** no. 5 (1984), pp. 225–228. Cited 2 times on pp. 39, 44.

[50] A. Lichtenberg and M. Lieberman. *Regular and stochastic motion*, vol. 38 (1983). Cited 1 time on p. 39.

[51] J. V. José and E. J. Saletan. *Classical dynamics: a contemporary approach* (Cambridge University Press, 1998). Cited 3 times on pp. 39, 41, 42.

[52] E. Ott. *Chaos in dynamical systems* (Cambridge, New York, 1993). Cited 5 times on pp. 39, 40, 41, 42, 43.

[53] W. E. Boyce and R. C. DiPrima. *Elementary differential equations and boundary value problems* (Wiley, 2008). Cited 1 time on p. 49.

[54] V. Meleshko. Selected topics in the history of the two-dimensional biharmonic problem. *Applied Mechanics Reviews* **56** no. 1 (2003), pp. 33–85. Cited 1 time on p. 51.

[55] M. Bloor and M. Wilson. An approximate analytic solution method for the biharmonic problem. *Proceedings of the Royal Society A: Mathematical, Physical and Engineering Science* **462** no. 2068 (2006), pp. 1107–1121. Cited 1 time on p. 51.

[56] V. Meleshko. Biharmonic problem in a rectangle. In A. Biesheuvel and G. J. F. van Heijst (eds.), *In Fascination of Fluid Dynamics*, pp. 217–249 (Springer, 1998). Cited 1 time on p. 51.

[57] V. Meleshko. Bending of an elastic rectangular clamped plate: Exact versus 'engineering' solutions. *Journal of Elasticity* **48** no. 1 (1997), pp. 1–50. Cited 1 time on p. 51.

[58] L. M. de la Cruz. Cómputo paralelo en la solución numérica de las ecuaciones de balance en flujo turbulento. *PhD thesis* . Cited 2 times on pp. 53, 54.

[59] C. Hirsch. *Numerical computation of internal and external flows: the fundamentals of computational fluid dynamics*, vol. 1 (Butterworth-Heinemann, 2007). Cited 2 times on pp. 53, 54.

[60] S. Patankar. *Numerical heat transfer and fluid flow* (CRC Press, 1980). Cited 1 time on p. 54.

[61] L. M. de la Cruz, I. García, V. Godoy and E. Ramos. Parallel lagrangian visualization applied to natural convective flows. In *Proceedings of the IEEE 2001 symposium on parallel and large-data visualization and graphics*, pp. 41–44 (2001). Cited 2 times on pp. 59, 98.

[62] M. Speetjens. Three-dimensional chaotic advection in a cylindrical domain. *PhD thesis* . Cited 2 times on pp. 59, 61.

[63] T. Krasnopolskaya, V. Meleshko, G. Peters and H. Meijer. Mixing in stokes flow in an annular wedge cavity. *European Journal of Mechanics-B/Fluids* **18** no. 5 (1999), pp. 793–822. Cited 1 time on p. 61.

[64] R. Sturman, S. Meier, J. Ottino and S. Wiggins. Linked twist map formalism in two and three dimensions applied to mixing in tumbled granular flows. *Journal of Fluid Mechanics* **602** (2008), pp. 129–174. Cited 4 times on pp. 78, 95, 104, 107.

[65] S. W. Meier, R. M. Lueptow and J. M. Ottino. A dynamical systems approach to mixing and segregation of granular materials in tumblers. *Advances in Physics* **56** no. 5 (2007), pp. 757–827. Cited 4 times on pp. 78, 95, 104, 107.

[66] H. Dullin and J. Meiss. Quadratic volume-preserving maps: Invariant circles and bifurcations. *SIAM Journal on Applied Dynamical Systems* **8** no. 1 (2009), pp. 76–128. Cited 2 times on pp. 85, 112.

[67] J. Tuwankotta and F. Verhulst. Symmetry and resonance in hamiltonian systems. *SIAM Journal on Applied Mathematics* **61** no. 4 (2000), pp. 1369–1385. Cited 1 time on p. 90.

[68] S. Wiggins. *Introduction to applied nonlinear dynamical systems and chaos* (Springer, 2003). Cited 1 time on p. 111.

[69] V. I. Arnold. *Mathematical methods of classical mechanics*, vol. 60 (Springer, 1989). Cited 1 time on p. 111.